

UNIVERSITÀ DEGLI STUDI DI NAPOLI  
FEDERICO II  
FACOLTÀ DI INGEGNERIA  
Industrial Engineering Dept. - Aerospace Sect.



*A thesis submitted in fulfilment of the requirements  
for the Doctoral degree in Aerospace Engineering*

---

**Design and experimental tests of an  
Unsteady Active Control Device for Drag  
Reduction of Car Shaped Bluff Bodies**

---

*Author:  
Giuseppe Calise*

TUTOR:  
Prof. Domenico Coiro

SUPERVISOR:  
Prof. Luigi De Luca

MARCH, 2016



## Declaration of Authorship

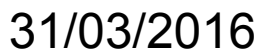
I, Giuseppe Calise, declare that this thesis, titled “Design and experimental tests of an Unsteady Active Control Device for Drag Reduction of Car Shaped Bluff Bodies”, and the work presented in it are my own. I confirm that:

- This work was done wholly or mainly while in candidature for a research degree at this University.
- Where any part of this thesis has previously been submitted for a degree or any other qualification at this University or any other institution, this has been clearly stated.
- Where I have consulted the published work of others, this is always clearly attributed.
- Where I have quoted from the work of others, the source is always given. With the exception of such quotations, this thesis is entirely my own work.
- I have acknowledged all main sources of help.
- Where the thesis is based on work done by myself jointly with others, I have made clear exactly what was done by others and what I have contributed myself.

Signed:



Date:





*Just keep swimming!*

*As long as I just keep trying,  
keep moving, keep hope,  
I can do anything.  
Life is not always a smooth path  
but you have to keep going  
to get to the good stuff.*

---

Brenna Jobe  
*Receptionist at Pointwise*



# Acknowledgments

I'm really thankful to all the people which help me not only for this work but more for the life.

A special notice is for my tutor Prof. D. Coiro who has been a constant reference, with his clear and valuable advices. Also, a special thank goes to Prof. F. Nicolosi and Dr. Eng. A. De Marco which introduce me to the topics of applied aerodynamics and CFD. I thank all the people of the ADAG group and DII for the time spent together as well.

Finally, there are no words to say how grateful I'm to my family and to you, my darling for the life, for being patient, confident and proud of me.





# Abstract

Improving aerodynamic efficiency of bluff bodies is a very interesting solution for reducing fuel consumption of vehicles. Reducing drag, hopefully with no change in lift, is the best way to improve aerodynamic efficiency of such bodies: in fact, if no change in lift is experienced, the vehicle handling does not change as well. Through the years, the drag reduction was obtained mainly modifying the overall body shape with the use of passive devices, as spoilers or flaps, in order to extend laminar flow and reduce separation. Even if this approach is quite easy and fast to implement, its limits result in the poor adaptability to different car shapes or cruise conditions. Therefore, understanding how to design and control an all-purpose active device able to reduce aerodynamic drag represents a very attractive field of investigation.

The work presented here deals with investigations on active control devices for drag reduction purpose: the main goal is to explore different systems and operating conditions in order to identify conditions which realize the higher drag reduction. Generally speaking, active control devices work generating a control jet near or in the separation zone, causing the flow to reattach on the body and to reduce its drag. The use of different prototypes allow to compare device effectiveness for different kind of cars: so, the effectiveness of two different active control devices has been tested on car shaped prototypes, via numerical analyses and experimental tests.

In the first part of this work, a brief overview about the drag reduction problem is presented, along with the introduction of the car shaped prototypes and the active control devices under test. Secondly, numerical simulations and experimental tests are presented and discussed. Lastly, using the electroacoustic analogy, it's presented the development of a simplified model for the design of such blowing devices and for evaluating the ideal power saving achievable with an optimized device.

---

# Table of Contents

---

<b>1</b>	<b>Introduction</b>	<b>1</b>
1.1	Bluff body aerodynamics overview . . . . .	2
1.2	The Ahmed body physics . . . . .	4
1.2.1	Ahmed body slant angle . . . . .	5
1.3	Literature Overview . . . . .	7
1.3.1	Previous works using passive control devices . . . . .	8
1.3.2	Previous works using active control devices . . . . .	9
1.4	On designing of active control devices . . . . .	10
<b>2</b>	<b>Bluff body models and active control devices under test</b>	<b>13</b>
2.1	The Ahmed body model . . . . .	13
	The role of the blowing plate configuration . . . . .	15
2.2	The simplified FIAT Punto car model . . . . .	17
2.3	Active Control Devices . . . . .	20
2.3.1	Unsteady Blowing Device under test . . . . .	21
	The UB 25° blowing plate . . . . .	23
	The UB 35° blowing plate . . . . .	24
2.3.2	Synthetic Jet Devices under test . . . . .	24
	Overview on design of a mechanical SJ . . . . .	26
	The SJ 25° blowing plates . . . . .	29
	The SJ 35° blowing plates . . . . .	29
<b>3</b>	<b>Numerical Simulations</b>	<b>31</b>
3.1	Preliminary thoughts on CFD simulations . . . . .	32
3.2	Two-dimensional simulations on 25° rear end Ahmed body . . . . .	32
3.2.1	Steady jets on Ahmed body . . . . .	35
	Inflow angle ( $\phi$ ) effects . . . . .	36
	Position ( $x_{pos}$ ) effects . . . . .	37
	Minimum effective velocity ( $V_{jet}$ ) . . . . .	39
3.2.2	Unsteady jets on Ahmed body . . . . .	40

	Unsteady blowing jets on Ahmed body . . . . .	41
	Synthetic jets on Ahmed body . . . . .	44
3.3	Three-dimensional simulations on 25° rear end Ahmed body	46
3.4	Three-dimensional simulations on 35° rear end Ahmed body	57
3.5	Three-dimensional simulations on a FIAT Punto Classic . .	60
<b>4</b>	<b>Wind tunnel experimental tests</b>	<b>67</b>
4.1	Experimental tests measurement equipments . . . . .	67
	Wool tufts . . . . .	67
	Oil Film . . . . .	68
	Particle Image Velocimetry (PIV) . . . . .	69
	Load cells . . . . .	69
	Hotwire . . . . .	70
	Pressure probes . . . . .	70
4.2	Experimental tests on 25° rear end Ahmed body . . . . .	71
	Tests with unsteady blowing device . . . . .	71
	Tests with synthetic jet device . . . . .	78
4.3	Experimental tests on 35° rear end Ahmed body . . . . .	89
	Tests with unsteady blowing device . . . . .	89
	Tests with synthetic jet device . . . . .	94
4.4	Experimental tests on FIAT Punto Classic . . . . .	102
	Tests with synthetic jet device . . . . .	102
<b>5</b>	<b>A simplified model for designing unsteady control devices using the electroacoustic analogy</b>	<b>109</b>
5.1	The idea and foundation elements . . . . .	110
5.2	Electrical circuit for device optimization . . . . .	113
5.3	Ideal power consumption and power saving estimation . . . .	116
<b>6</b>	<b>Conclusions and future works</b>	<b>123</b>
	<b>References</b>	<b>127</b>

---

# List of Figures

---

1.1	Car shapes evolution summary . . . . .	2
1.2	Bluff body drag generation mechanisms . . . . .	4
1.3	Ahmed body model . . . . .	5
1.4	Ahmed body's wake structure . . . . .	6
1.5	Ahmed body's drag coefficient breakdown . . . . .	7
2.1	Ahmed body model - CAD representation . . . . .	14
2.2	Ahmed body parts - CAD representation . . . . .	15
2.3	Ahmed body model - Real prototype . . . . .	16
2.4	Ahmed body model - Load cells configuration . . . . .	17
2.5	The 35° Ahmed body wind tunnel installation . . . . .	18
2.6	FIAT Punto Classic - Real and simplified shapes . . . . .	19
2.7	FIAT Punto Classic - Exploded view . . . . .	19
2.8	FIAT Punto Classic - Load cells configuration . . . . .	20
2.9	Unsteady Blowing Device under test . . . . .	22
2.10	Unsteady Blowing Device - Electrically driven rotating valve	23
2.11	UB blowing plates and chambers . . . . .	24
2.12	Synthetic jet device under test . . . . .	26
2.13	SJ blowing plates - #1/#2/#3 . . . . .	30
2.14	SJ blowing plates - #4/#5 . . . . .	30
3.1	2D simulation - Mesh and boundary conditions . . . . .	33
3.2	Separation point identification . . . . .	35
3.3	Influence of $\phi$ angle on $C_D^*$ . . . . .	37
3.4	Influence of $x_{pos}$ on $C_D^*$ . . . . .	38
3.5	Cross-effects of $\phi$ and $x_{pos}$ on $C_D$ . . . . .	39
3.6	Jet velocity ( $V_{jet}$ ) effects on $C_D$ . . . . .	40
3.7	Unsteady blowing - Frequency effects on drag coefficient $C_D^*$	43
3.8	Synthetic jet - Frequency effects on drag coefficient $C_D^*$ . . .	45
3.9	Some details of the three-dimensional computational domain	47

3.10	Flow field comparison between two-dimensional and three-dimensional simulations . . . . .	51
3.11	Velocity streamlines on several planes, during optimal operating conditions . . . . .	53
3.12	Vorticity streamlines on several planes, during optimal operating conditions . . . . .	54
3.13	Comparison of velocity contours on several planes - Unsteady blowing . . . . .	55
3.14	Comparison of velocity contours on several planes - Synthetic jet . . . . .	56
3.15	Time history of a simulation on 35° rear end Ahmed body . . . . .	58
3.16	Wake distributions of a 35° rear end Ahmed body . . . . .	59
3.17	Oswald factor vs. Aspect ratio . . . . .	60
3.18	FIAT Punto model computational grid . . . . .	61
3.19	Some flow visualizations around the FIAT Punto model in clean configuration . . . . .	63
3.20	FIAT Punto Classic - Force coefficients history . . . . .	63
3.21	Streamlines visualizations - FIAT Punto model w/o control device . . . . .	64
3.22	Streamlines visualizations - FIAT Punto model w/ control device . . . . .	65
4.1	Wind tunnel facility of the University of Naples . . . . .	68
4.2	Unsteady Blowing device - Preliminary measurements . . . . .	72
4.3	UB hotwire measurements on 25° rear end Ahmed body . . . . .	73
4.4	Tufts images for the 25° rear end Ahmed body . . . . .	74
4.5	Oil film images for the 25° rear end Ahmed body . . . . .	75
4.6	UB load cells measurements - 25° rear end Ahmed body . . . . .	76
4.7	$u$ velocity fields for the 25° rear end Ahmed body . . . . .	78
4.8	Velocity components for the 25° rear end Ahmed body . . . . .	79
4.9	Hotwire measurements - SJ #1 configuration . . . . .	81
4.10	Load cells measurements - SJ #1 configuration . . . . .	81
4.11	Hotwire measurements - SJ #2 configuration . . . . .	84
4.12	Load cells measurements - SJ #2 configuration . . . . .	84
4.13	Hotwire measurements - SJ #3 configuration . . . . .	87
4.14	Load cells measurements - SJ #3 configuration . . . . .	87
4.15	UB hotwire measurements on 35° rear end Ahmed body . . . . .	90
4.16	Tufts images for the 35° rear end Ahmed body . . . . .	91
4.17	Oil film images for the 25° rear end Ahmed body . . . . .	91
4.18	PIV images for the 35° rear end Ahmed body on symmetry plane . . . . .	92

4.19	$u$ velocity fields for the 35° rear end Ahmed body . . . . .	93
4.20	UB load cells measurements - 35° rear end Ahmed body . . . . .	94
4.21	Velocity components for the 35° rear end Ahmed body . . . . .	96
4.22	Hotwire measurements - SJ #4 configuration . . . . .	97
4.23	Load cells measurements - SJ #4 configuration . . . . .	98
4.24	Load cells measurements - SJ #5 configuration . . . . .	99
4.25	FIAT Punto model overview . . . . .	103
4.26	Tufts images for the FIAT Punto Classic . . . . .	104
4.27	$u$ velocity fields for the FIAT Punto Classic model . . . . .	105
4.28	Hotwire measurements - FIAT Punto model w/ SJ . . . . .	107
4.29	Load cells measurements - FIAT Punto model w/ SJ . . . . .	107
5.1	Lumped Element model for blowing chamber and plate . . . . .	112
5.2	Distributed model for connection tubes . . . . .	113
5.3	Overview of the distributed line block of SimRF Simulink toolbox . . . . .	114
5.4	Schematic view of the optimization cycle . . . . .	116
5.5	SimRF Simulink toolbox - Equivalent circuit of the tested SJ device . . . . .	117
5.6	Optimization cycle results . . . . .	118
5.7	Circuit used for power consumption estimation . . . . .	119



---

# List of Tables

---

1.1	Drag repartition on a realistic car . . . . .	3
2.1	Maximum dimensions of the FIAT Punto model . . . . .	18
2.2	Unsteady Blowing Device - System geometry . . . . .	23
2.3	Synthetic Jet Device - System geometry . . . . .	28
3.1	Influence of $\phi$ angle on $C_D^*$ . . . . .	37
3.2	Influence of $x_{pos}$ on $C_D^*$ . . . . .	38
3.3	Cross-effects of $\phi$ and $x_{pos}$ on $C_D$ . . . . .	39
3.4	Jet velocity ( $V_{jet}$ ) effects on $C_D$ . . . . .	40
3.5	Unsteady blowing - Frequency effects on drag coefficient $C_D^*$	42
3.6	Synthetic jet - Frequency effects on drag coefficient $C_D^*$ . . .	46
3.7	Unsteady blowing - Three-dimensional simulations summary	49
3.8	Synthetic jet - Three-dimensional simulations summary . . .	50
4.1	UB load cells measurements - 25° rear end Ahmed body . .	77
4.2	Load cells measurements - SJ #1 configuration . . . . .	82
4.3	Load cells measurements - SJ #2 configuration . . . . .	85
4.4	Load cells measurements - SJ #3 configuration . . . . .	88
4.5	UB load cells measurements - 35° rear end Ahmed body . .	93
4.6	Load cells measurements - SJ #4 configuration . . . . .	100
4.7	Load cells measurements - SJ #5 configuration . . . . .	101
4.8	Load cells measurements - FIAT Punto model w/ SJ . . . .	106
5.1	Optimization cycle results - System geometry . . . . .	116
5.2	Ideal power consumption . . . . .	120
6.1	Main results summary . . . . .	124





---

## Introduction

---

This work summarizes and extends the research named ‘*Componenti avanzati per la riduzione della resistenza all’avanzamento*’ (*Programma Operativo Nazionale* (PON) 01 – 01750), founded by the *Ministrero Italiano Università e Ricerca* (MIUR) and the European Union. The University of Naples ‘Federico II’ was tasked for studying innovative aerodynamic devices capable of reducing vehicles drag. In the light of this, the use of active flow control devices was the choice.

The automotive industry give greatest attention to discovering new methods for reducing fuel consumption and, thus, for improving overall vehicle efficiency. Depending on vehicle velocity, to improve efficiency and reduce fuel consumption can be followed different strategies: at  $V < 80$  km/h, the forces due to mechanical and tires frictions are greater than aerodynamic drag; conversely, at  $V > 80$  km/h, aerodynamic drag is higher than the others. So, the reasons of fuel consumption depend on the car travelling velocity. Furthermore, considering that higher velocity results in higher energy demand, it’s clear why drag optimization plays a key role.

Initially, vehicle external shapes evolved mainly for safety, comfort or aesthetic reasons. With the 70’s oil crisis, car manufacturers were encouraged in improving energy saving: studies carried out during those years showed that the aerodynamic drag causes 30% fuel consumption in an urban cycle and more than 70% at 120 km/h cruise velocity. This consideration is also stated in [1], where it is explained how fuel consumption, for a middle class car driving at  $V > 100$  km/h, is mainly due to aerodynamic drag. Today, the growing ecological interest has given a new boost to this research field.

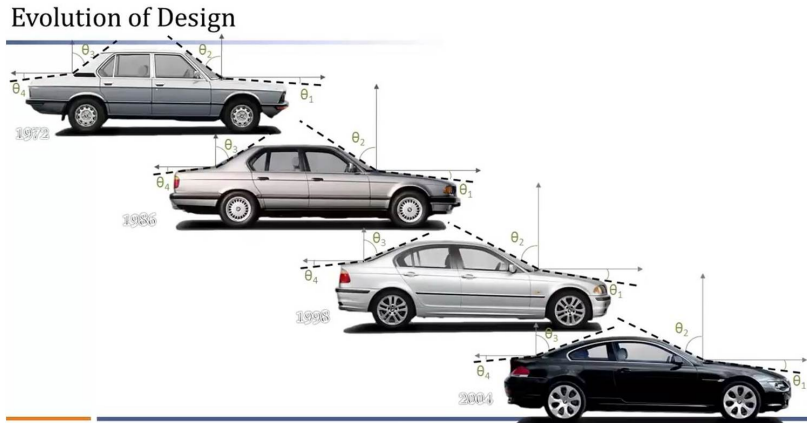


Figure 1.1: Car shapes evolution summary

In Figure 1.1 it's presented an example of the car shapes evolution since 70's until now.

## 1.1 Bluff body aerodynamics overview

Usually, the study on automotive drag reduction is performed using bluff bodies. When a body of whatever geometry is hit by a flow current, its shape causes a pressure distribution over it which result globally in the so-called aerodynamic force: this aerodynamic force can be split into two components known as lift, perpendicular to apparent flow direction, and drag, along the apparent flow direction. So, lift and drag forces represents intrinsic body characteristics because they depends on body shape. Bluff bodies distinguish from the so-called aerodynamic body because they have a relatively low aerodynamic efficiency: in other words, they produce a large amount of drag and a relatively small lift. In [2], it's also stated that about the 70% of the automotive drag depends on its external shape, while only the remaining 30% is due to other automotive parts. This fascinating consideration is summarized in Table 1.1, justifying the great interest on bluff body aerodynamics for drag reduction purposes. Thus, the use of bluff bodies for automotive drag reduction concern.

In aerodynamics, the forces are usually expressed in terms of aerodynamic

Position	% of $C_D$
Upper Surface	40%
Lower Surface	30%
Wheels	15%
Cooling	10%
Others	5%

**Table 1.1:** Drag repartition on a realistic car

coefficients: so, the classic and generic formulation for aerodynamic force is

$$F = \frac{1}{2} C_F \rho V^2 A \quad (1.1)$$

where  $A$  is the body reference area,  $\rho$  is the flow density,  $V$  is the flow velocity and  $C_F$  is the force coefficient. This formulation is almost interesting since it relates flow properties and peculiar body characteristics, expressed by the force coefficient. Similar formulations can be written for drag and lift, as well. The flow field around a bluff body, like a car, allows to identify three main components of drag:

**Surface friction drag:** this drag component has to be account to the boundary layer around the body. Its contribution to bluff body overall drag is relatively small and ,in general, is higher in region of attached flow in turbulent regime.

**Pressure drag:** this drag component is due to the pressure difference between front and aft zones of the bluff body. It is experienced when the flow detach from the body and, thus, the bluff body overall drag is mainly due to it.

**Vortex-induced drag:** the pressure difference between top and bottom surfaces of a finite length body causes this drag component. Pressure difference determines flow motion from the bottom, higher pressure zone, to the top, at lower pressure, which results in a rolling up of flow particles. Thus, this mechanism of drag production is strictly connect to the bluff body capability of producing lift.

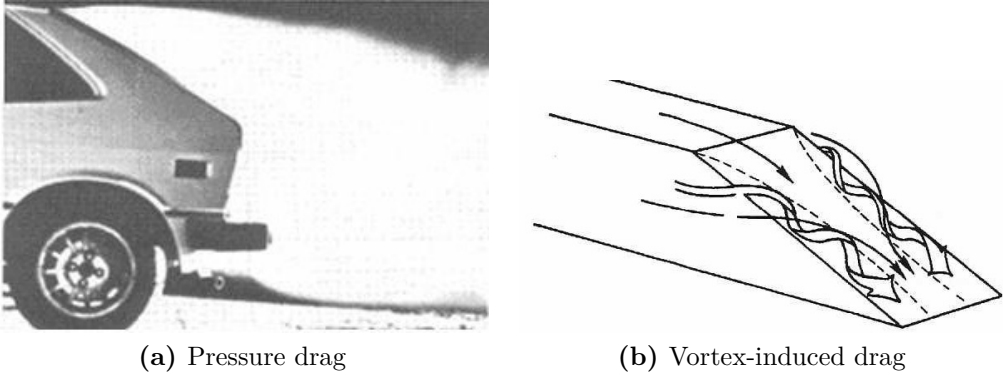


**Figure 1.2:** Bluff body drag generation mechanisms

In Figure 1.2, the pressure drag and the vortex-induced drag mechanisms are depicted. So, reduce bluff body aerodynamic drag is possible limiting the flow separation in its aft zone, without affecting lift characteristics. In fact, lift production changes causes not only higher drag, but also car handling modifications.

## 1.2 The Ahmed body physics

Modern cars can be classified in three different classes: square-back, fast-back and notch-back. Anyway, all of these kind of car behaves like a bluff body. The most famous bluff body used as a simplified car model is the so-called Ahmed body. The studies conducted in [3] discovered the capability of such simplified geometry to reproduce wake structures of several vehicle classes. Its particular shape minimizes aerodynamic influence of the front, while the rear can be easily modified, changing the slant angle  $\Phi$ : different values of  $\Phi$  reproduce wake flow structures of fast-back, hatch-back or square-back cars. Hence, the Ahmed body is considered a reference model for car aerodynamics studies and, due to case complexity, past studies used Ahmed body with  $\Phi = 25^\circ$  as a test case.

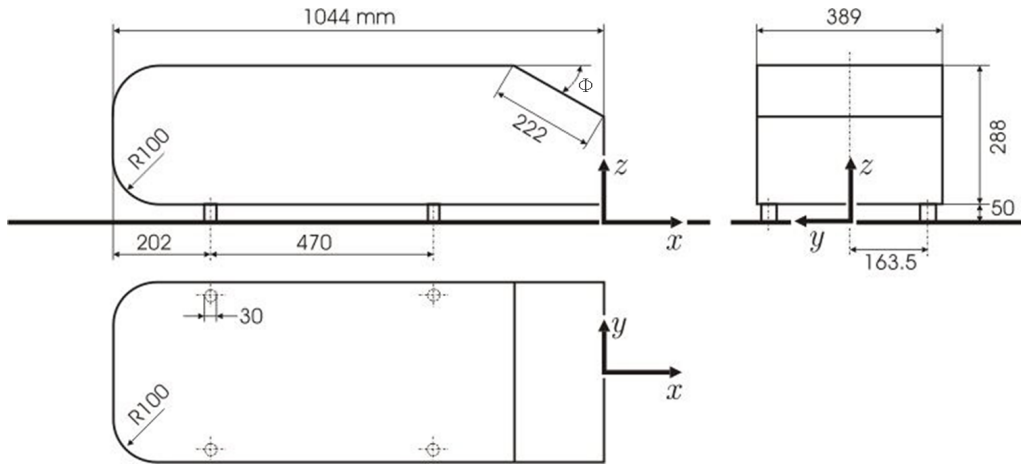


Figure 1.3: Ahmed body model

### 1.2.1 Ahmed body slant angle

In [1] all the relevant works on passenger cars aerodynamics are summarized. Also, a deep description of flow structures and considerations on Ahmed body performance is presented. Summarizing, flow topology around an Ahmed body is strongly dependent on slant angle  $\Phi$ . During the tests of Ahmed (see [3]), he investigated most relevant  $\Phi$  angles in the range  $0^\circ$  to  $40^\circ$ . In fact, he discovered that, in this range, can be identified three sub-range with well defined flow behaviour:

$0^\circ < \Phi < 15^\circ$ :

the flow is quite attached to the body and, like a bluff body, it presents a separation zone in the wake. So, in this configuration, the wake is considered near to two-dimensional one.

$15^\circ < \Phi < 30^\circ$ :

the flow structure is strongly three-dimensional with a small separation bubble on the inclined aft surface of the body; also, vortices detach from the body rear corners, usually called C-pillar, and a larger recirculation area is present behind the body.

$30^\circ < \Phi < 40^\circ$ :

the flow is completely detached from the upper body corner to the

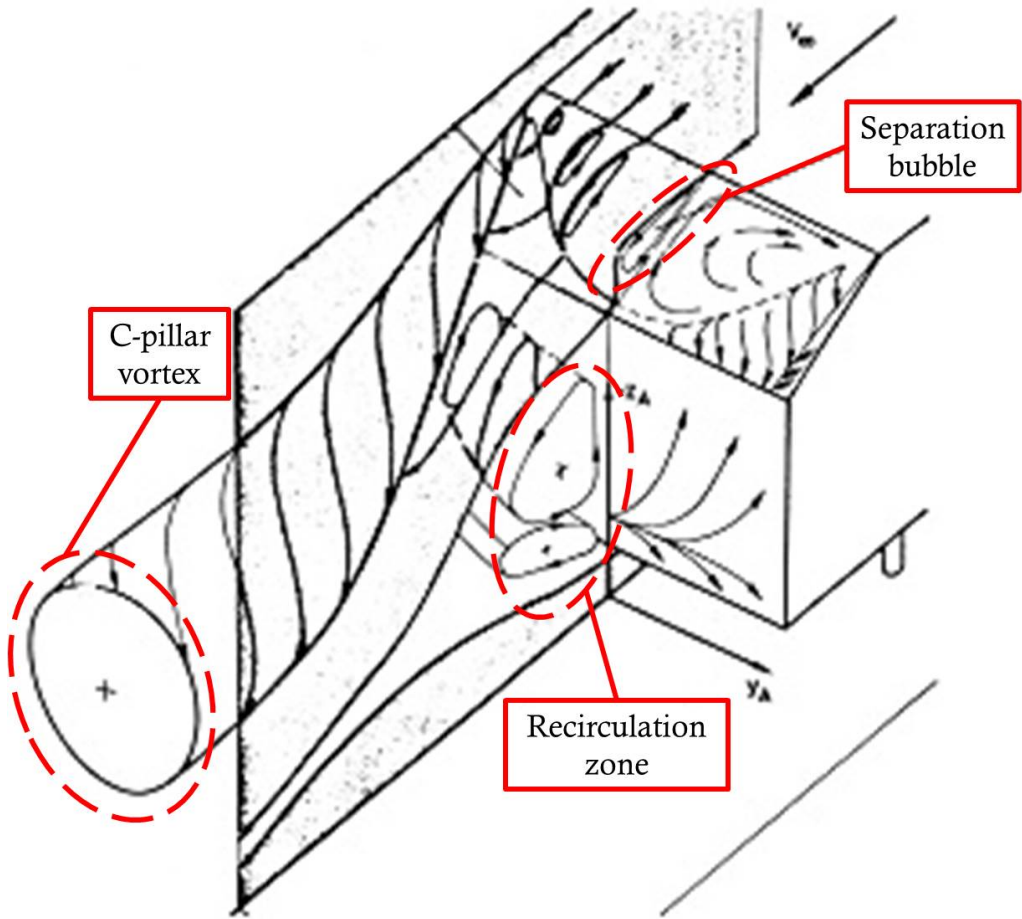


**Figure 1.4:** Ahmed body's wake structure

end of the body and C-pillar vortices disappear; thus, it is considered two-dimensional again with a wide separation and recirculation area.

The particular behaviour of the Ahmed body is also recognizable in Figure 1.5: the  $C_D$  of the Ahmed body has a minimum near  $\Phi = 15^\circ$ ; then, it increases up to  $30^\circ$  of  $\Phi$  angle and, finally, it falls down when  $\Phi > 30^\circ$ . The Figure 1.5 shows each contribution of Ahmed body surface to drag, as well. As noted in [3], the front surface ( $c_K^*$ ) contribution is small and almost independent of  $\Phi$ , like that of the top and bottom side panels ( $c_F^*$ ), while the drag components due to slanted surface ( $c_S^*$ ) and vertical end (also known as base) surface ( $c_B^*$ ) work in an opposite way: increasing the  $\Phi$  angle, the extent of  $c_B^*$  decreases and so the frictional drag related to it; conversely,

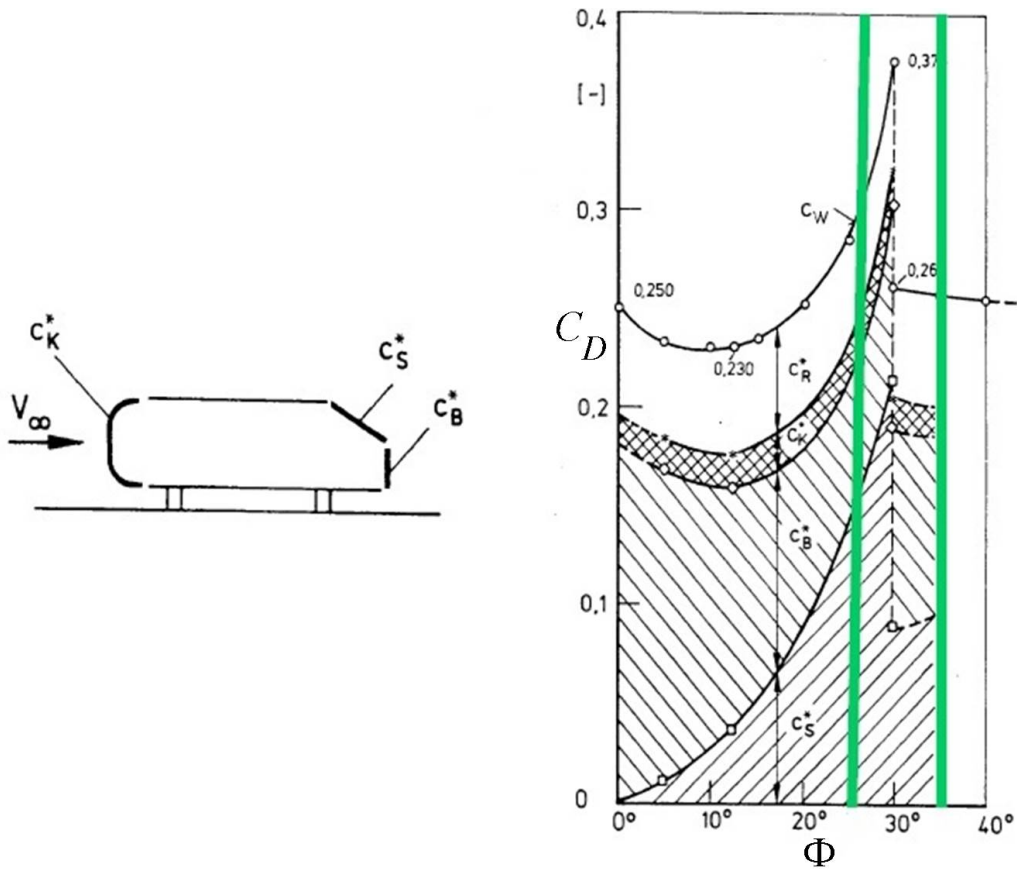


**Figure 1.5:** Ahmed body's drag coefficient breakdown

the strength of C-pillar vortices grows, along with the frictional drag due to a larger  $c_s^*$  surface. When  $\Phi$  approaches  $30^\circ$ , the C-pillar vortices break up and the frictional drag redistribute.

## 1.3 Literature Overview

During the years, a really wide number of studies were completed about bluff body aerodynamics. A milestone for automotive research is [1]: this book collects, in a well organized structure, all the main works regarding road vehicles, along with satisfying insights about the other related topics, such as aerodynamic principles, wind tunnels and so on. For the automotive industry, the innovative shape of bluff body proposed by Ahmed, its characteristics



and results of his investigations, represented a real turning point for research on vehicle optimization. In [3], the Ahmed body and its characteristics are deeply analysed. Similar to [1], the books [4] and [5] provide better understanding on the effects of each car component on performance.

The work in [6] is very similar to the one presented here. It describes experimental tests on a  $25^\circ$  Ahmed body model equipped with a pulsed jet device. It deals with the comparison of different pulsed jet shapes and locations, with the aim of identify the most effective configuration. Tests have been performed in a wind tunnel using a 1 : 1 scaled model, having a substantial compliance with previous studies. The authors of [6] have been focused only on pulsed jet effectiveness over the  $25^\circ$  Ahmed body model, without investigating the pulsed jet behaviour on other shapes.

### **1.3.1 Previous works using passive control devices**

About the drag reduction topic, different ways have been persecuted. As a first way, the idea is to change body shape. Thus, several analysis, both numerical and experimental, have been performed, substantially replicating the experience of Ahmed ([7], [9], [10], [11]), but using the most recent investigation techniques. Similarly, the second way concerns the use of so-called passive systems, like flaps or vortex-generators, to organize the flow field, limiting the turbulent regime and separation zones. In general, using passive devices, it is possible to obtain up to 30% of drag reduction. The authors of [12] have been obtained 9% of drag reduction simply using a classical automotive deflector. Larger drag reduction has been shown in [13], where the authors achieved up to 25% of reduction using flaps at C-pillar locations for  $30^\circ$  Ahmed body. The papers [14] and [15] describes the use of vortex generators in order to modify separation bubble dimension, causing less drag of about 12% and 10%, respectively. Even if passive devices are quite simple to design, their fundamental limit is the inability to follow vehicles cruise speed changes: in other words, a passive device works properly only in the cruise condition at which it has been designed.

### 1.3.2 Previous works using active control devices

Conversely, the latter and most recent way used to reduce drag is using the so-called active devices: in principle, such devices can be adapted to cruise speed variations, modifying their operating parameters, along with a very limit impact on vehicle shape. Thus, these characteristics make active devices really attractive for automotive applications. Active devices differ from passive device for the need of providing power to their operations. Several kind of active control devices can be identified: a first classification can be made distinguishing from suction devices to pulsed jets; also, pulsed jets can be split in other categories, that are steady or unsteady blowing jets and synthetic jets. The value of the mean mass flow distinguishes the former pulsed jet types from the latter: while steady or unsteady blowing jets have a non-zero mean mass flow, synthetic jets have a zero mean mass flow. In other words, blowing jets use pressured air from a tank, while synthetic jets do not need any reservoir, taking supply air from the boundary layer. Therefore, in principle, synthetic jets demand less power for working as compared with blowing jets, even if their production is more complex and costly. The researches on active devices performance to limit vehicle drag have shown the chance to achieve positive results up to 15%. Most of these works deal with 25° Ahmed body. In [16] and [17], the use of steady aspiration on the top of the slant surface allowed 17% of drag reduction and, also, a suppression of the separation area. Experimental tests with synthetic jets on the top of the slant surface (see [18]) have shown positive effects ( $\Delta D = -8\%$ ). Tests with pulsed jets (see [19]) showed to be less efficient than the synthetic jets ( $\Delta D = -5.7\%$ ); numerical analyses, using steady blowing jets in conjunction with suction at the slant top edge, produce a little bit more than 7% of reduction (see [20]), while in [21], using only steady blowing jets, the drag reduction is of 6%. Advanced techniques for controlling pulsed jets, in order to produce feedback controlled periodic signals, display better results with  $\Delta D = -15\%$  (see [22], [23] and [24]).

## 1.4 On designing of active control devices

Active devices performance depends on several parameters, which have to be selected properly. For unsteady pulsed jet devices, the principal parameters are surely: the mass flow injected into the boundary layer, the jet oscillations frequency, the inflow location and the inflow angle. Considering that numerous other parameters (i.e., how the system generate the desired jet, ...) could be taken into account, it seems evident the complexity involved in the designing of active control devices. Therefore, it's necessary to make smaller the field of investigation, focusing only on the most influencing ones.

For the analyses described within this work, two pulsed jet generation systems have been investigated: an unsteady blowing device and a mechanical synthetic jet device. Due to aforementioned system complexity, only a parameter subset has been investigated, keeping constant the remaining ones. The scope has been to identify, if exists, any operating condition of such devices able to reduce drag of bluff bodies under test. The system effectiveness analyses have included both Computational Fluid Dynamics (CFD) simulations and wind tunnel measurements.

In the following sections, all the analyses results will be presented and discussed. In Chapter 2, the bluff bodies used during the experimental tests are presented and a more deep insight on active devices under test is proposed; some outlines on the design of a mechanical synthetic jet device are also provided.

In Chapter 3, are summarized CFD simulations performed using CD-adapco's Star-CCM+ software. These simulations concern Ahmed body, with  $\Phi = 25^\circ$  and  $\Phi = 35^\circ$ , and a simplified shape of a real car, that is a Fiat Punto Classic. Preliminary two-dimensional simulations on  $25^\circ$  Ahmed body have been used to find out conditions which maximize drag reduction, for each parameter under investigation; then, via three-dimensional simulations, the effectiveness of all optimal conditions simultaneously was tested. Simulations have been used for comparison with experimental tests, as well.

In Chapter 4, experimental tests performed in the wind tunnel test facility of the University of Naples 'Federico II' are presented. The used

measurements equipments are described and data from tests are presented and commented.

The Chapter 5 presents a simplified model, based on electro-acoustic analogy, for the analysis and optimization of unsteady pulsed jet devices. The idea has been to create a tool capable to estimate output velocity of a pulsed jet system, in which all available connection lines, from the generation system to the output slit, can be taken into account. In this way, the proper tube length can be properly chosen in order to maximize output velocity with less energy demand.

Finally, the final Chapter 6 recaps the principal results of the whole study and suggests some possible future developments.



---

## Bluff body models and active control devices under test

---

In this Chapter, the bluff bodies and active control devices used during the experimental tests are presented. Also, some outlines on the design of a mechanical synthetic jet device are provided.

### 2.1 The Ahmed body model

The Ahmed body model used for both numerical and experimental analyses is a 1 : 1 scale of the body used in [3], shown in Figure 1.3. This model has been designed and realized with the capability of replacing several parts, in order to investigate slightly different configuration. In particular, the Figure 2.1 shows the modular approach used in designing of such body.

Such model is composed of two parts which do not change during all the analysis, the bottom and the top ones; conversely, the rear end, the blowing chamber and the blowing plate, can be substituted with others of different characteristics. Each part of Ahmed body model is presented in Figure 2.2. The bottom part plays a key role for experimental testing: the primary measurement equipment, that are load cells, has to be firmly fixed to this part of the model, in order to sense relative motions between the wind tunnel frame and the model. Also, this part of the model could be used, if necessary, as a supporting floor on which auxiliary devices can be set. The rear end can be replaced during tests to modify the slant angle  $\Phi$  of the Ahmed body: in this way, it's possible to investigate different

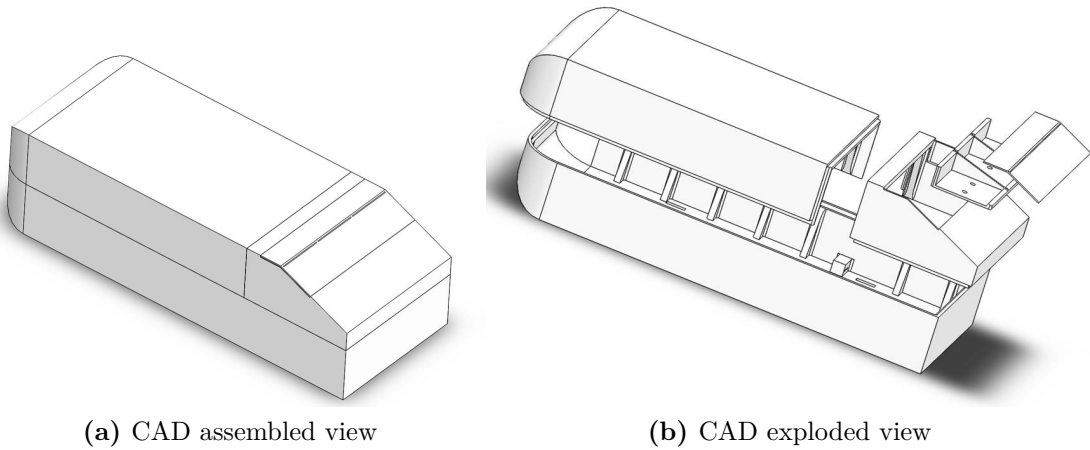


**Figure 2.1:** Ahmed body model - CAD representation

flow field due to different value of  $\Phi$ . Two different rear end parts have been realized, one with  $\Phi = 25^\circ$  and the other with  $\Phi = 35^\circ$ , relating to fast-back and square-back cars respectively. The scope has been to compare the effectiveness of active control devices on these two flow fields. Other replaceable parts are the blowing chamber and the blowing plate: the former can be modified to increase or decreased the volume of fluid inside the chamber, while the latter can be adjusted to modify the angle at which the flow is put into the boundary layer and the delivered mass flow rate. Finally, the top part completes the shape of the Ahmed body model.

The Ahmed body model for testing has been realized in PROLAB 65, a polyurethane machinable slab, with a three-axis CNC milling machine. The model overall weight is about 14.5 kg. Some pictures of the realization phase are in Figure 2.3.

The initial prototype set-up has three anchor points for the load cells (three load cells configuration); however, during the tests, some irregularities has been noted and it has been necessary to modify this layout, passing to a more easy two load cells configuration. In the three load cells configuration, two load cells are in the rear part, one per side, below the blowing chamber, while the remaining one is in the symmetry plane, at the front. Conversely, the two load configuration has both the load cells in the symmetry plane, one

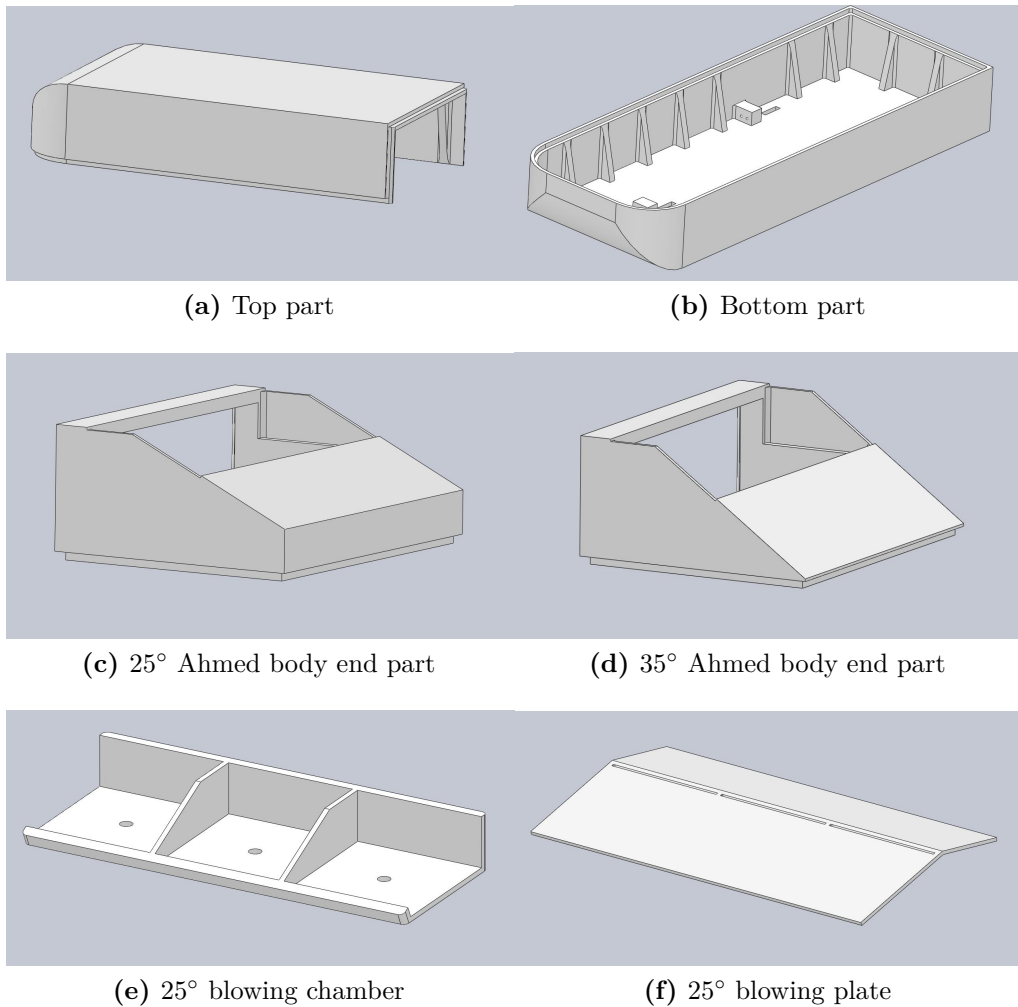


**Figure 2.2:** Ahmed body parts - CAD representation

at the front and the other at the rear. The difference between the two configurations are visible in Figure 2.4. Finally, as an example, the 35° Ahmed body installation inside the wind tunnel facility is shown in Figure 2.5.

### The role of the blowing plate configuration

As it will be explained later, the inflow angle ( $\phi$ ), that is the angle at which the mass flow rate is injected, along with the inflow velocity ( $V_{jet}$ ), namely the velocity which causes the desired mass flow rate, are very important parameters for the proper working of unsteady blowing devices.



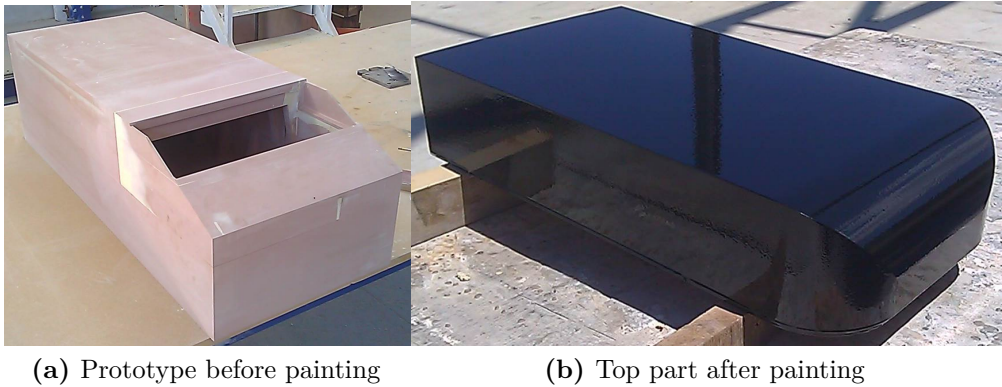


**Figure 2.3:** Ahmed body model - Real prototype

Anyway, while the amount of mass flow rate may be changed in other ways, i.e. increasing initial pressure, the inflow angle is fixed by the blowing plates design. It has to be noticed that, for the scope of this work, inflow angle ( $\phi$ ) is defined as the angle between the pulsed jet direction and the Ahmed body slanted surface ( $c^*_S$ ).

For the scope of this work, the blowing plate configuration depends strictly both on active control device and on bluff body model under test. All of the blowing plates used have a rectangular slit from which the mass flow can exit. In order to reduce the number of parameters involved, the length, the thickness and the depth of the slit are fixed; thus, the shape of the channel, which develops in the blowing plate thickness, may be chosen. Also, the slit location is an important parameter and it has been chosen considering results of several two-dimensional simulations. Mainly, two inflow angle have been tested:  $\phi = 20^\circ$  and  $\phi = 90^\circ$ , where the latter identifies a pulsed jet direction perpendicular to surface. Thus, the former plates have a curved converged channel, into the blowing thickness, in order to increase the output velocity from the slit, while the latter plates have a straight rectangular channel. Major details on the used blowing plates will be provided later.

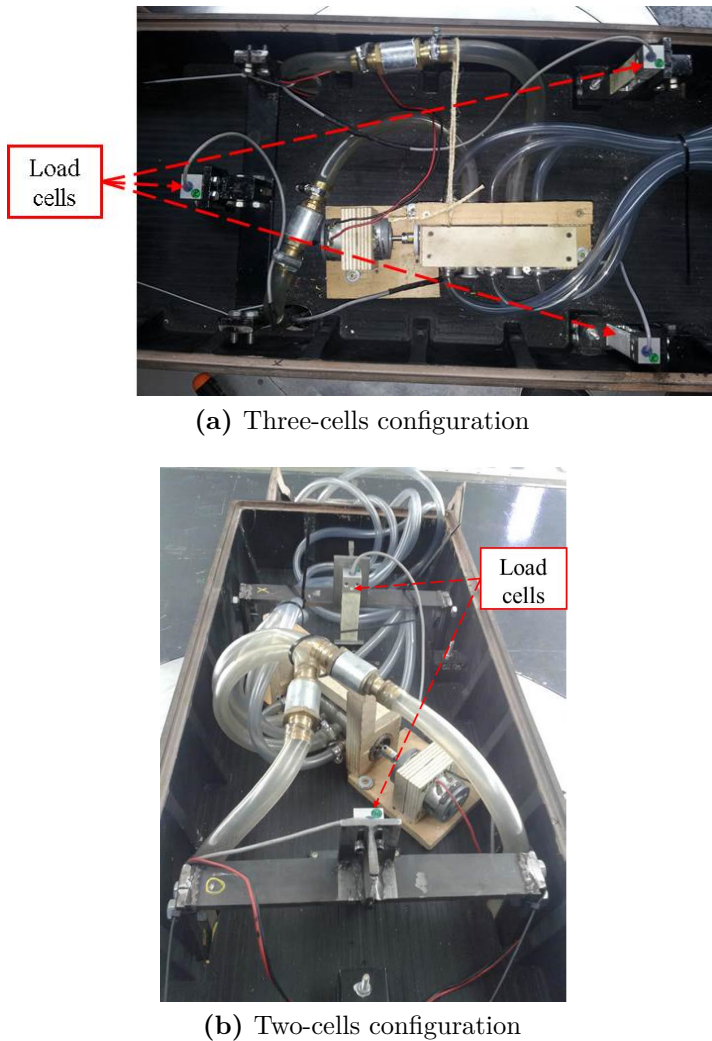


**Figure 2.4:** Ahmed body model - Load cells configuration

## 2.2 The simplified FIAT Punto car model

After a deep analysis of active control devices performance on a simplified car model, such as the Ahmed body, the same devices have been tested on a real car, as well. So, a model of an existing car, the FIAT Punto Classic, has been realized. The model is about 1 : 4 scaled model of the real car: the maximum dimensions of the model are listed in Table 2.1. The model has been designed starting from the real car shape, eliminating non relevant parts, as windshield wipers, outer door handles, rear-view mirror,



**Figure 2.5:** The 35° Ahmed body wind tunnel installation

Dimension (max)	[m]
Length	0.965 m
Width	0.400 m
Height	0.376 m
Ground Height	0.070 m

**Table 2.1:** Maximum dimensions of the FIAT Punto model

etc. Also, the rotating motion of the wheels has not been taken into account. In Figure 2.8 the two shapes are compared.

As the Ahmed body model, the FIAT Punto model has been made using a modular approach. Unlike the Ahmed body, the FIAT Punto model has been realized using Fused Deposition Modelling (FDM). Even if FDM technique allows the creation of complex geometries and entities with very low level of end products, it is yet an expensive production method. In fact, in order to have high level of accuracy in shape definition, suitable component dimensions and time of production, it is necessary to use very costly equipment. Hence, model parts has been defined in order to match limits of the available FDM machine. The FIAT Punto model, as can be seen in Figure 2.7, consists of three main parts:

- the bottom, at which load cells are attached;
- the top, which encloses the internal model volume and define the shape of the car;

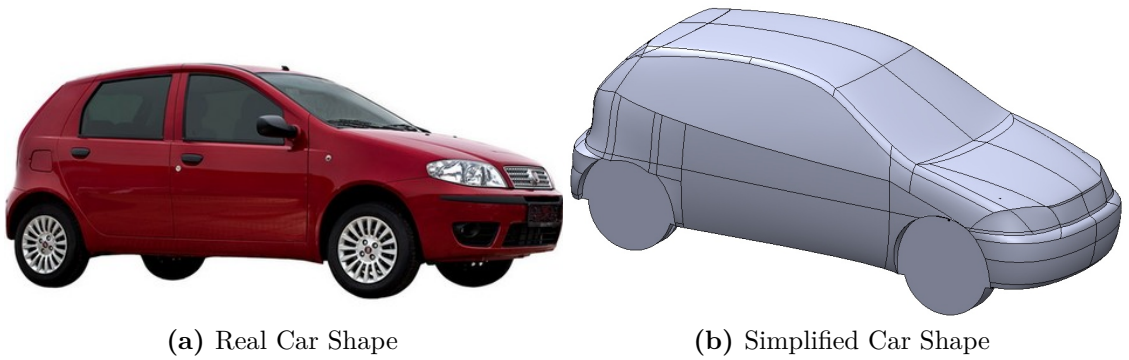


**Figure 2.6:** FIAT Punto Classic - Real and simplified shapes

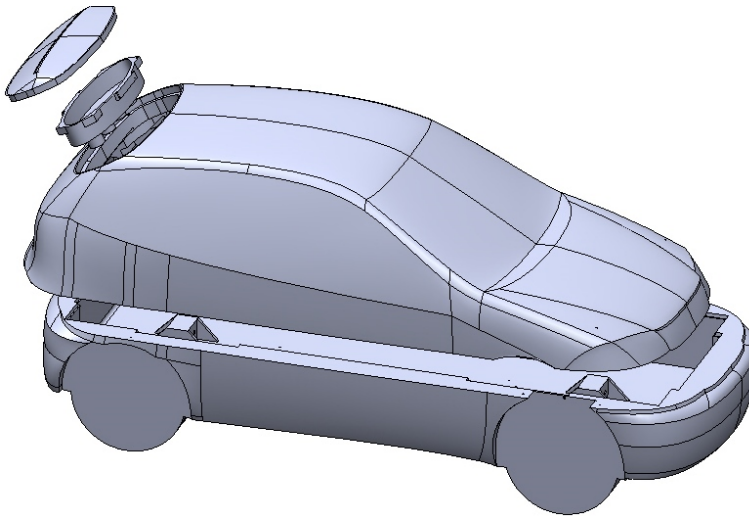
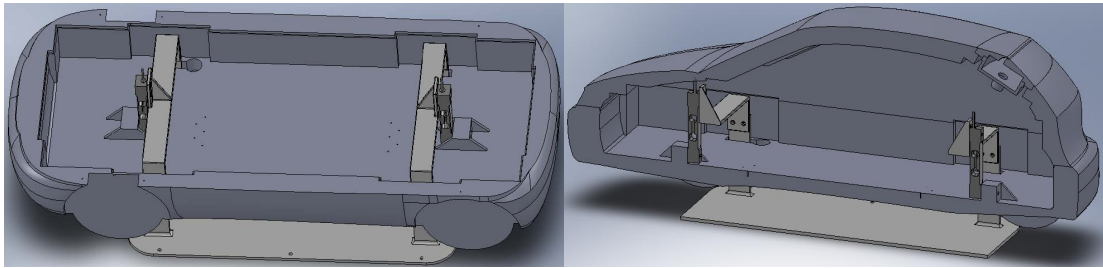


**Figure 2.7:** FIAT Punto Classic - Exploded view

- the blowing chamber, which consists of two different parts, the chamber and the blowing plates, that could be changed for testing different configurations.

The FIAT Punto model has the same connection to wind tunnel of the Ahmed body model: two load cells are located in the model symmetry plane, being the junction between model and wind tunnel frame.



(a) Top view

(b) Section view

**Figure 2.8:** FIAT Punto Classic - Load cells configuration

## 2.3 Active Control Devices

Operations of active control devices involve a large number of parameters, which can be set to match the desired target. During the years, several studies dealt with the problem of controlling boundary layer separation to improve airfoils or wings aerodynamic efficiency. Most of these showed that through the use of a steady blowing or suction within the boundary layer, separation can be delayed or eliminated. Nevertheless, the power needs and the complex controlling technique related to these devices have pushed them out of production. Recently, the idea of using unsteady control device, instead of steady ones, has seemed more promising. Even if control laws continue to be an issue, unsteady device should require less power, as they intend to use frequency to guide boundary layer reattachment.

In [25], the author deals with the problem of improve aircraft endurance by means of turbulent separation control. Initially, he resumes the main results in boundary layer control using unsteady devices, highlighting that the effectiveness of this techniques is mainly dependent on the so-called reduced frequency  $F^+$  and jet momentum coefficient  $C_\mu$ :

$$F^+ = \frac{f * X_{act}}{V_{inf}} \quad (2.1)$$

$$C_\mu = \frac{2h}{X_{act}} \left( \frac{V_{mean}}{V_{inf}} \right)^2 + \frac{2h}{X_{act}} \left( \frac{V'}{V_{inf}} \right)^2 \quad (2.2)$$

in which  $f$  is the jet frequency,  $X_{act}$  is the distance between the injection point and the model trailing edge,  $V_{inf}$  is the free stream velocity,  $h$  is the slot exit extension,  $V_{mean}$  is the average outlet velocity from the device and  $V'$  is the oscillating part of the outlet velocity from the device. Using this non-dimensional quantities, Seifert, Wygnanski and Tinapp ([26], [27], [28], [29]) suggest that the most effective forcing frequency for flow control is  $F^+ \approx 1$ ; about the momentum coefficient, they discovered that, for a steady jet, it has to be in the range 0.002 – 0.010. To achieve this objectives, two different kinds of unsteady jet device have been arranged and tested: the former is an ‘Unsteady Blowing Device’ (UB), while the latter is a mechanical ‘Synthetic Jet Device’ (SJ). The main difference among these device is both the way of producing and also the average value of output velocity. The UB device is a system which uses pressurized air to produce a non-zero mean output velocity; conversely, the SJ device captures flow from the boundary layer, energizes it, and ejects a signal with zero mean output velocity. In other words, the UB device is a non-zero mean mass flow device, while the SJ is a zero-mean mass flow device. Anyway, it has to be noticed that the name ‘Synthetic Jet Device’ is used to highlight the capability of such device of producing, starting from a certain distance from the output section, a almost steady jet; this artificial (synthetic) steady jet is obtained stimulating characteristic boundary layer frequencies, which, in turn, causes flow to reattach. In the light of this, it is clear the great interest towards synthetic jet devices, that promises less power demand respect to other active control techniques.

### 2.3.1 Unsteady Blowing Device under test

The unsteady blowing device used during experimental tests is presented in Figure 2.9. It consists of a main compressor tank, connected by means of tubing, to other device components. Flow from the main tank goes into the so-called compensation tank, that stabilizes the flow from the compressor. Then, the flow passes through a electrically controlled rotating valve, that converts steady flow from the tank to unsteady one (see Figure 2.10): the rotating valve is driven by a stepper motor, whose RPMs can be set changing

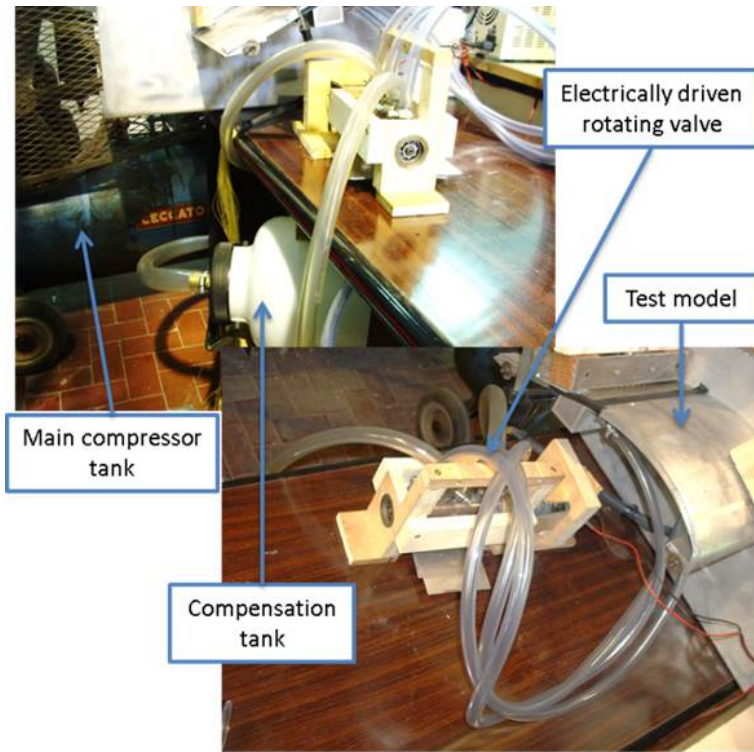
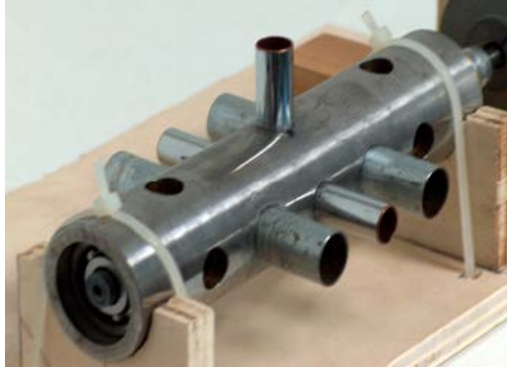


Figure 2.9: Unsteady Blowing Device under test

voltage supply. Finally, unsteady flow from the rotating valve goes into the test model, where a blowing terminal is disposed: the blowing terminal is composed of the blowing chamber and the blowing plates, from which the unsteady jet is deployed. Therefore, overall UB performance depends on several parameters, each one influences unsteady jet production. The tested UB device geometrical arrangement is presented in Table 2.2, where  $L_1$ ,  $d_1$ ,  $L_2$ ,  $d_2$ ,  $L_3$ ,  $d_3$  are lengths and diameters of tubing segments.

During experimental tests, the compressor pressure and voltage supply, of the stepper motor, have been changed in order to investigate the effectiveness of different system operational conditions in controlling and reducing boundary layer separation. Also, depending on the tested model, blowing chamber and blowing plate have been changed and compared.



**Figure 2.10:** Unsteady Blowing Device - Electrically driven rotating valve

Compressor		Tubing segments	
Volume	100 L	$L_1$	1.500 m
Pressure (max)	12 atm	$d_1$	0.0254 m
Compensation Tank		$L_2$	1.800 m
Volume	10 L	$d_2$	0.0127 m
Rotating Valve		$L_3$	1.000 m
Stepper Motor Supply	0 V to 12 V	$d_3$	0.0095 m

**Table 2.2:** Unsteady Blowing Device - System geometry

### The UB 25° blowing plate

The terminal part of the UB device is composed of two sub-components, that are the blowing chamber and the blowing plate. For the 25° rear end Ahmed body, only one configuration of blowing plate and blowing chamber has been tested. The CAD representation of this tested configuration is shown in Figure 2.11a, in which it is also compared with the similar configuration for the 35° rear end Ahmed body. In this configuration, the overall blowing chamber volume is about 0.001 18 m<sup>3</sup>; furthermore, inside the blowing chamber, there are 4 walls which divide the chamber and the blowing plate into smaller ones. As it will more clear later, the blowing plate has a rectangular slit, which dimensions are 0.379 m of length and 0.002 m of width; the slit is located with its middle point at 0.005 m from the starting point (corner) of the slanted surface  $c^*_s$ . Along the thickness of



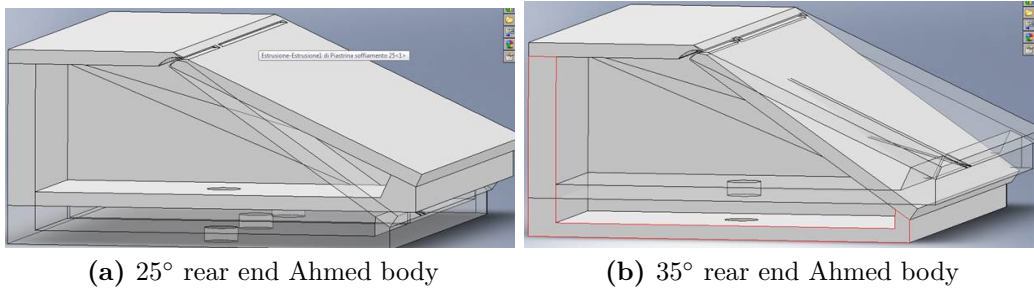


**Figure 2.11:** UB blowing plates and chambers

the blowing plate, the blowing channel is slightly convergent, in order to increase the magnitude of the outlet velocity; also, the channel shape has been designed to obtain velocity vector with inflow angle  $\phi = 20^\circ$  referred to the slanted surface, that correspond to  $5^\circ$  of inclination to the horizontal plane.

### The UB $35^\circ$ blowing plate

As the  $25^\circ$  rear end Ahmed body, for the  $35^\circ$  rear end Ahmed body only one configuration of blowing plate and blowing chamber has been tested. The CAD representation of the tested configuration is shown in Figure 2.11b. The overall blowing chamber volume is about  $0.00139 \text{ m}^3$  and it is also divided into 4 smaller chamber by means of wall. These walls extends up to the blowing plate, which has the same rectangular slit of the blowing plate for the  $25^\circ$  rear end Ahmed body (length of  $0.379 \text{ m}$  and width of  $0.002 \text{ m}$ ). Slit positioning, blowing channel shape and inflow angle ( $\phi$ ), relative to the slanted surface, are the same as the blowing plate of the  $25^\circ$  rear end Ahmed body; but, the inflow angle referred to the horizontal plane is larger ( $15^\circ$ ).

## 2.3.2 Synthetic Jet Devices under test

Generally speaking, the synthetic jet (SJ) is an actuator commonly adopted to control the boundary layer separation. It consists in a closed cavity with an opening on its top surface. The studies of [30] and [31] highlight the attractive advantage of using synthetic jets, compared with the

traditional continuous and pulsed jets: they apply momentum transfer from the outer to the inner part of the boundary layer to be controlled, without the introduction of mass flow rate.

About the operation of a synthetic jet, it is characterized by two phases: in the first one, the flow leaves the cavity, whereas in the other one, the flow is sucked within the cavity. Through the jet blowing phase, high momentum flux is ejected in the boundary layer inner region, where it could be requested to prevent separation: during this phase, the formation of two counter-rotating vortices may be observed. This vortex propagation is interrupted during the ingestion phase, as the flow moves towards the cavity: during the suction phase, the flow coming from the boundary layer outer region is forced to move towards the wall. Thus, also during this phase, high momentum fluid is transferred from the exterior to the near wall region. Furthermore, two counter-rotating vortices generated during the blowing phase allow to increase the mixing process in the inner part of the boundary layer, and give a further contribution to the boundary layer laminar separation delay.

In order to produce this kind of unsteady jet, a mechanical device has been designed and produced for test purposes. Starting from the work [32], a mechanical synthetic jet device has been designed and further details on SJ dimensioning are presented in §2.3.2. The system depicted in Figure 2.12b is made up of mechanical engines, driven by an electrical motor. Engines are common internal combustion ones, properly adapted to have only one duct: thus, the engine head, where usually there are intake and exhaust valves, has been modified fusing valve ducts into only one. In this way, cylinder inlet and outlet coincide and it can work like the closed cavity (chamber) of a synthetic jet. Excitation of the air inside the chamber is provided by the piston: during its run toward the bottom dead centre, it create a depression inside the cylinder which sucks air from the duct; conversely, when it run towards the top dead centre, it pushes air outside from the cylinder (blowing). Thus, the operation of such device is very similar to a typical synthetic jet actuator.

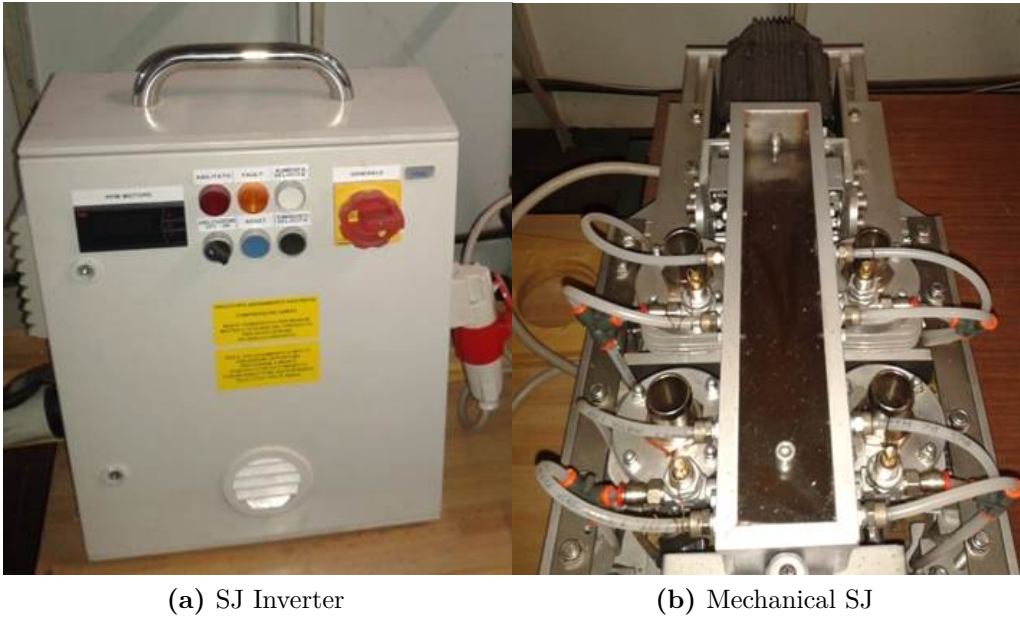


Figure 2.12: Synthetic jet device under test

### Overview on design of a mechanical SJ

The work [32] explains how to design a mechanical SJ device and shows some bench tests on such device, too. Basically, the idea followed by the author is to realize a simple and compact mechanical device able to behave like a synthetic jet. Thus, the role of a typical SJ chamber is played by the cylinder, while the piston movements have to produce the same behaviour as the SJ membrane. In the light of this, fluid conservation laws along with SJ non-dimensional parameters, such as  $C_\mu$  and  $F^+$ , have to be the same for both devices.

$$\dot{m} = \rho V_{jet} A_{jet} \tag{2.3}$$

$$F^+ = \frac{f X_{act}}{V_{inf}} \tag{2.4}$$

$$C_\mu = \frac{h (\rho V^2)_{jet}}{c (\rho V^2)_{inf}} \tag{2.5}$$

where  $V_{jet}$  is the outlet velocity from the slot,  $A_{jet}$  is the slot area,  $X_{act}$  is the slot location from the body trailing edge,  $f$  is the jet frequency,  $V_{inf}$  is

the free-stream velocity,  $h$  is the slot width and  $c$  is the body longitudinal dimension.

As reported before, to be effective, an unsteady jet device has to have  $F^+ \approx 1$  and  $C_\mu$  in the range 0.002 – 0.010. Thus, fixing  $F^+ = 1$  and  $C_\mu = 0.002$ , it is possible to identify the corresponding value of the cylinder volume, which can be obtained multiplying the piston maximum stroke times the cylinder bore. From the reduced frequency  $F^+$  equation, it is possible to verify that the jet location, which causes  $x_{te} = 0.215$  m, is effective if the unsteady jet frequency is about  $f = 100$ /s. Similarly, the equation (2.5) allows to verify that the slot width ( $h$ ) of 0.002 m is suitable to obtain a sufficient amount of  $C_\mu$ .

Considering that  $\dot{m}$  has to be the same both at the internal combustion outlet and at the blowing plate outlet, is it possible to determine the maximum piston stroke. From Computational Fluid Dynamic (CFD) simulations, that will be dealt with in the § 3, it resulted that the minimum effective steady jet velocity is  $V_{jet} = 40$  m/s: using this value as a target for the mechanical SJ device and assuming, not far from reality, that cylinder stroke can be described by sine wave ( $x(t) = X \sin(2\pi f t)$ ), it is possible to determine the cylinder maximum stroke. Due to mass conservation law, the stroke is related to the cylinder outlet section  $A_{cyl}$ , so that it has been fixed to 0.000 49 m<sup>2</sup>, which correspond to a cylinder diameter ( $d_{cyl}$ ) of 0.025 m. From equation (2.6), using  $A_{jet} = 0.379$  m x 0.002 m = 0.000 758 m<sup>2</sup>,  $V_{jet} = 40$  m/s and  $f = 100$ /s, it results that  $X = 0.106$  m. Thus, multiplying  $A_{cyl}$  times  $X$ , it results the required cylinder volume, that is 51.90 cm<sup>3</sup>.

$$\dot{m} = (\rho V A)_{jet} = \rho \frac{dx}{dt} A_{cyl} \Rightarrow X = \frac{(V A)_{jet}}{(2\pi f) \cos(2\pi f t) A_{cyl}} \quad (2.6)$$

Due to the strong connection between frequency and outlet velocity, such devices don't allow to uncouple  $C_\mu$  and  $F^+$ : thus, the mechanical SJ device produced for testing has more than one cylinder, with the scope of having much higher  $C_\mu$  at the same  $F^+$  using several in-phase cylinders. Anyway, all the data presented in this work are relative to the operations of only one

Internal Combustion Engine		Tubing segments	
Volume	35.8 cm <sup>3</sup>	$L_1$	0.700 m
Stroke	30 mm	$d_1$	0.0318 m
Bore	39 mm	$L_2$	1.800 m
Electrical motor (Driver)		$d_2$	0.0254 m
Speed	0 RPM to 3500 RPM	$L_3$	0.500 m
Torque (max)	0 N m	$d_3$	0.0254 m
Power (max)	0 kW		
Gear ratio	1 : 2		

**Table 2.3:** Synthetic Jet Device - System geometry

cylinder of the mechanical SJ device. Finally, it has to be noticed that, in order to use commercially available products, the mechanical SJ cylinders chosen are a bit smaller than required, as it is shown in Table 2.3.

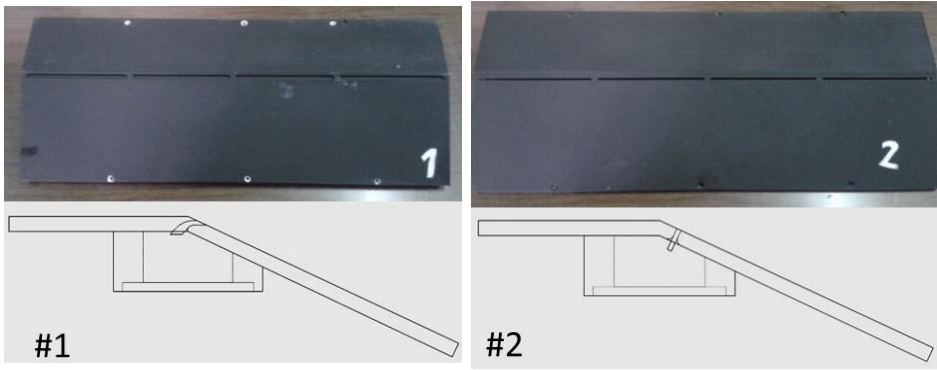
The SJ device under test includes some other components in addition to cylinders: an essential role is played by connection tubes and blowing chamber: in fact, in order to use the SJ, it is essential to connect the engine duct to the blowing plates, devoted to distribute air into the boundary layer. As for the UB device and with more relevance for the SJ device, tubing lengths and diameters affect operating resonance of the SJ device. Ideally, if the device works in resonance condition, the output velocity could be higher with less power demand. Usually, SJ device works in resonance conditions to improve performance. The SJ under test, as the UB device, is composed by three sections of tubing, the dimensions of which are listed in Table 2.3. The tubing arrangement is a sort of tree branches: the section #1 ( $L_1, d_1$ ) splits into two sections #2 ( $L_2, d_2$ ) and, then, into four sections #3 ( $L_3, d_3$ ), which are connected to the blowing chamber. Due to the different slant angle, blowing chamber of the 35° rear end Ahmed body (0.000 178 m<sup>3</sup>) is slightly larger than the one of the 25° rear end Ahmed body (0.000 166 m<sup>3</sup>). Both blowing chamber are very smaller compared to those of the UB device, as the effective volume of the SJ device is that of the mechanical cylinder.

### The SJ 25° blowing plates

For the 25° rear end Ahmed body, the performance of three different blowing plates for the SJ device have been compared. All the three blowing plates are shown in Figure 2.13. These blowing plates have the same slit positioning and dimensions (0.379 m × 0.002 m), but they differ for the inflow angle. While the #1 blowing plate has the inflow angle  $\phi = 20^\circ$ , from the slanted surface ( $c_s^*$ ), both the #2 and #3 have inflow angle  $\phi = 90^\circ$ , so as the flow from the slit is perpendicular to the surface. Also, while the #1 and #2 blowing plates have some interruptions along the slit, the #3 has no interruptions: a similar comparison between the #2 and #3 blowing plates is reported in [33] and, here, it has been replicated. Nevertheless, it has to be noticed that, as for the UB plates, the #1 blowing plate presents a convergent duct shape in the plate thickness, while the #2 and #3 are straight. All of these blowing plates have been realized by means of FDM technique.

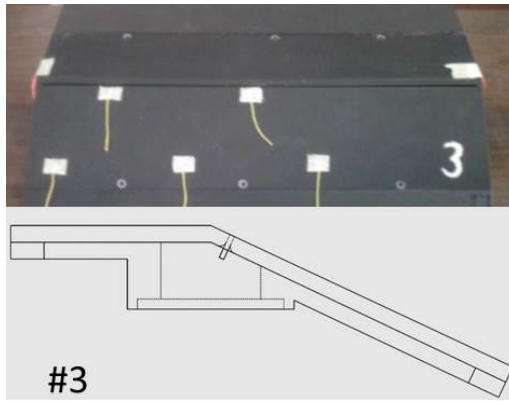
### The SJ 35° blowing plates

The blowing plates used for the 35° rear end Ahmed body with SJ device are two: they are similar (Figure 2.14) except for the inflow angle. As the #1 blowing plate, the #4 blowing plate has an inflow angle  $\phi = 20^\circ$  from the slanted surface ( $c_s^*$ ), which it results in a rotation of about 15° clockwise to the horizontal plane. In order to have the same flow rotation as the #1, the blowing plate #5 has been designed and realized: it has an inflow angle  $\phi = 30^\circ$  relative to the slanted surface and exactly the same configuration of the #4 plate. In this way, inflow angle sensitivity of the 35° rear end Ahmed body has been investigated. All of these blowing plates have been realized by means of FDM technique.



(a) #1

(b) #2



(c) #3

Figure 2.13: SJ blowing plates - #1/#2/#3

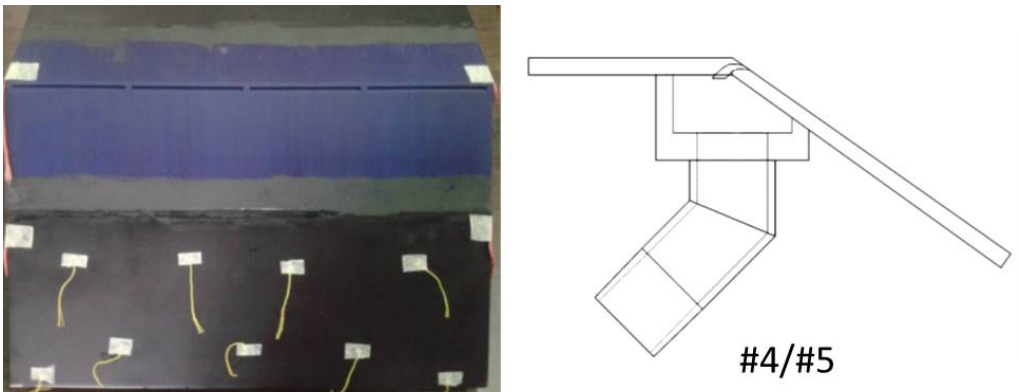


Figure 2.14: SJ blowing plates - #4/#5

# Chapter **3**

---

## Numerical Simulations

---

Today, Computational Fluid Dynamics (CFD) simulations are one of the key analysis methods used for engineering applications. Their role is to help to better understand the physics phenomena which involve natural elements like wind, storms, floods, or sea waves. In the aerodynamic field, the role of CFD simulations is both to reduce expensiveness of experimental tests and to compare different configurations much quicker. This is the motivation of the great increasing interest on CFD, especially for the automotive industry. Furthermore, differently from aerospace, where semi-empirical models allow to preliminary design and performance estimation of an aircraft, automotive design do not have similar models to estimate interactions between several components. Thus, the need to use extensively experimental tests and, nowadays, CFD simulations.

Among the different models to numerically solve Navier-Stokes equations, CFD simulations in this work has been done using Reynolds averaged Navier–Stokes (RANS) equations. RANS equations are the lowest model generally available within a CFD solver. Even if it is not the more accurate, it allows to obtain flow field solution quicker as compared with Detached Eddy Simulations (DES), Large Eddy Simulations (LES) or Direct Numerical Simulations (DNS). To be solved, RANS equations need to be specified the so-called boundary conditions, which are physical conditions on numerical domain boundaries, along with turbulence model. Usually, a number of turbulence models are available in the CFD solver and solution accuracy could be influenced by the choice of the proper one. Thus, the importance of the expertise of the CFD operator, as well as for the grid generation.



## 3.1 Preliminary thoughts on CFD simulations

In this work, CFD simulations have been used as preliminary tool in order to analyse active control device sensitivity to its parameters changes, before the design and production of such devices for wind tunnel testing. For this reason, the aim of these simulations is to compare bluff bodies drag performance in response to several different operational conditions of the active control device. So, due to the comparison purpose, numerical simulations are not aimed to estimate the exact value of body drag, but, instead, to know how this drag amount can be influenced. All CFD simulations have been executed with the CD-adapco's Star-CCM+ software.

Firstly, CFD simulations have been intended to discover an effective design condition for an active control device able to reduce drag of a bluff body, such as the Ahmed body. By means of two-dimensional simulations, a number of parameters have been investigated, like active control device location ( $x_{pos}$ ), inflow angle ( $\phi$ ), average jet velocity ( $V_{jet}$ ) and frequency ( $f$ ). When the most effective jet configuration has been identified, it has been verified with three-dimensional simulations. Lastly, the three-dimensional simulations have been used to phenomenologically compare what has been observed during wind tunnel tests. It has to be noticed that, due to the computational expensiveness of such simulations, their number has been limited as lower as possible.

## 3.2 Two-dimensional simulations on 25° rear end Ahmed body

The computational domain used for two-dimensional simulation is shown in Figure 3.1, along with the description of physical conditions applied on the domain boundaries. As can be seen, the velocity condition at the inlet boundary is replicated on the floor boundary, with the aim to simulate the presence of a rolling belt: in fact, in automotive industry, it is usual to use such kind of belt to reproduce the boundary layer effects experienced by the

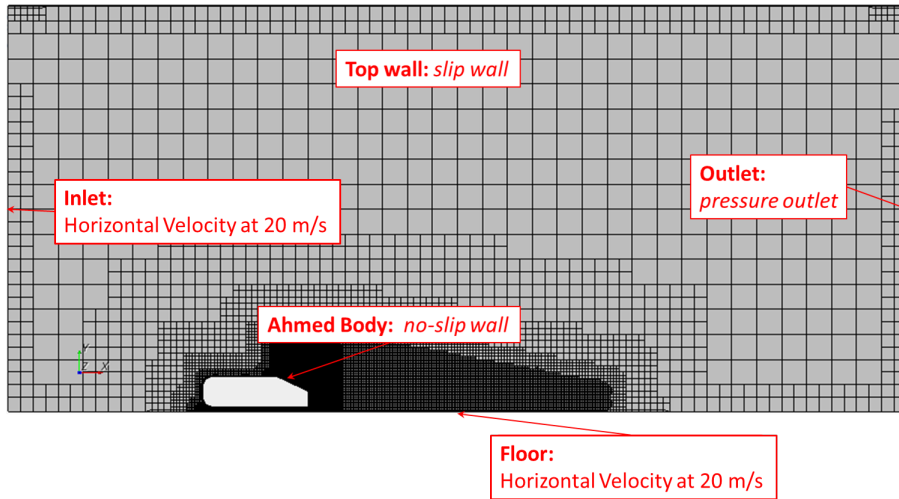


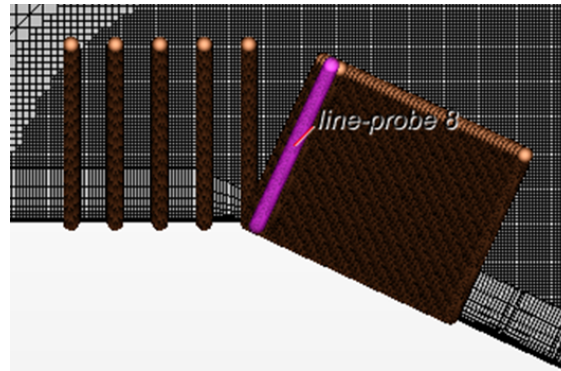
**Figure 3.1:** 2D simulation - Mesh and boundary conditions

car during travelling. So, at the inlet and at the floor boundaries, it has been imposed a 20 m/s velocity inlet condition, with velocity vector parallel to horizontal plane. At the outlet, pressure outlet boundary condition has been imposed, while, at the top boundary, slip wall boundary condition has been used. This set of boundary condition has seemed to be the more appropriate for simulating the wind tunnel environment. On the Ahmed body with 25° rear end, a non-slip wall boundary condition has been imposed, in order to simulate the development and growth of boundary layer around the body.

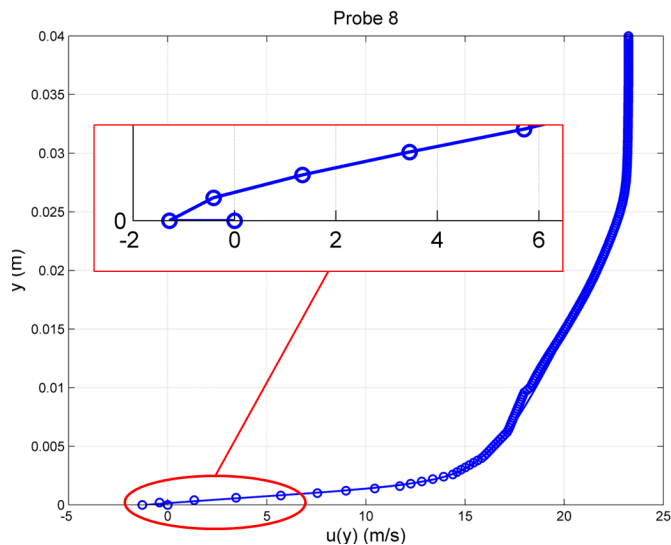
Overall computational domain dimensions are 10 m of length and 5 m of height; the Ahmed body is placed inside the domain at 2.5 m from the inlet boundary, with a clearance of 0.005 m from the floor. For grid generation, it has been chosen the trimmed model, which generate a quite structured computational grid. The computational grid complies some refinements: around the body, to catch the boundary layer development; in the zone of the slanted surface, where strong flow separation should occur, and in the body wake. So, the two-dimensional computational domain counts almost 300000 cells. As extensively explained in [34], after a comparison among the different turbulence models available in the Star-CCM+ software, the SST  $k-\omega$  has been selected, which is well documented to be more appropriate where large flow separations are expected.

Before introducing active control device effects on Ahmed body, some simulations have been performed on so-called clean configuration with the aim of analysing pressure distribution and discovering the location at which separation starts. To do this, some line probes has been created over the Ahmed body surface, by the slanted surface. Using line probes is possible to extract flow quantities, such as pressure, velocity and so on, along the line: in this way, it has been possible to reconstruct velocity into the boundary layer. Having the velocity boundary profile, it is possible to identify separation point: in fact, when velocity near the boundary is reversed, this location can be assumed as separation point. In Figure 3.2, it is shown the first velocity profile in which the velocity is reversed near the wall: it is relative to the line probe 8, located at 0.002 m from the corner. Knowing this, the idea is to introduce active control jet rather close this location, in order to influence separation and to cause flow reattachment.

In all two-dimensional simulations, results are presented as mean values, where the average is computed over the last 1000 iterations, and the average value of drag coefficient is indicated as  $C_D^*$ .



(a) Line probes distribution



(b) Boundary layer velocity profile

**Figure 3.2:** Separation point identification

### 3.2.1 Steady jets on Ahmed body

Introducing active control device to reduce drag, it is necessary to investigate effectiveness of each parameter in doing the desired task. So, first of all, the control jet has been investigated as steady jet: in this way, steady jet parameters have been supposed as starting point for unsteady jet ones. In fact, it has been assumed that the velocity ( $V_{jet}$ ), inflow angle ( $\phi$ ) and position ( $x_{pos}$ ), of an effective steady jet are the same for an unsteady jet.

To introduce the active control jet in the simulations, a new boundary

has been created. For this boundary, which width and position could be modified parametrically, velocity inlet boundary condition has been used. It has to be noticed that, using two-dimensional simulations, jet outlet section is defined only by its width and, so, no information can be gathered regarding its length: in other words, in two-dimensional simulations, the jet outlet section is modelled as an infinite length channel, which width has been assumed, initially, as 0.005 m. Assuming a value for jet outlet section width allows to reduce the number of parameters to investigate; conversely, it limits the analyses to a small set of the all effective and suitable system configurations.

In [34], it is also shown how the introduction of a steady jet influences the boundary layers, before and after the identified separation point.

### Inflow angle ( $\phi$ ) effects

The first parameter analysed is the inflow angle ( $\phi$ ) in Figure 3.3a . It is useful to remember that, in the context of this work, inflow angle is defined as the angle between the jet velocity direction and the slanted surface: positive values of inflow angle denote counter-clockwise rotations starting from slanted surface.

As for each parameter, investigations are carried out keeping fixed all the remaining parameter. In other words, inflow angle effectiveness has been evaluated ranging  $\phi$  from  $0^\circ$  to  $25^\circ$ , while the jet location and velocity have been kept constant, respectively to  $x_{pos} = +0.005$  m, from the corner, and  $V_{jet} = 50$  m/s. The limiting values of  $\phi$  have been fixed considering that  $\phi = 0^\circ$  corresponds to a really tangential flow on the surface, while  $\phi = 25^\circ$  corresponds to a inflow velocity parallel to the horizontal plane, for the  $25^\circ$  rear end Ahmed body.

In Figure 3.3b it is shown the  $C_D^*$  for different values of  $\phi$ , while numerical data are presented in Table 3.1. From results seems that exists a range of angles ( $5^\circ < \phi < 20^\circ$ ) in which the  $C_D^*$  does not change. This result is interesting because suggests that, when  $x_{pos} = +0.005$  m and  $V_{jet} = 50$  m/s, small variations of  $\phi$  does not influence the  $C_D$  reduction, preventing for any eventual production or mounting error.

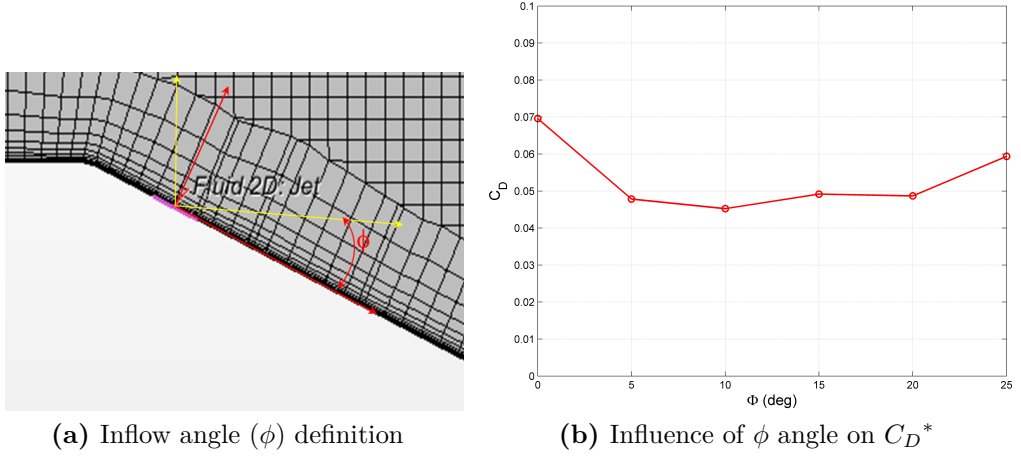


**Figure 3.3:** Influence of  $\phi$  angle on  $C_D^*$

$\phi$	$C_D^*$
0°	0.070
5°	0.048
10°	0.045
15°	0.049
20°	0.049
25°	0.059

**Table 3.1:** Influence of  $\phi$  angle on  $C_D^*$

### Position ( $x_{pos}$ ) effects

Secondly, the jet positioning effect has been investigated. As before, some other parameters like inflow angle and velocity have been kept fixed to  $\phi = 15^\circ$  and  $V_{jet} = 50$  m/s. The range of position evaluated starts from 0.01 m before the corner, indicated with  $-$  sign, to 0.015 m after the corner, with  $+$  sign, and jet positioning is referred to the middle point of the velocity inlet boundary, as it is shown in Figure 3.4a.

The Figure 3.4b shows the results of these simulations and numerical values are reported in Table 3.2: from these result that the best position, using  $V_{jet} = 50$  m/s and  $\phi = 15^\circ$ , is  $x_{pos} = +0.010$  m.

To take in account cross-influence of  $x_{pos}$  and  $\phi$ , some other simulations

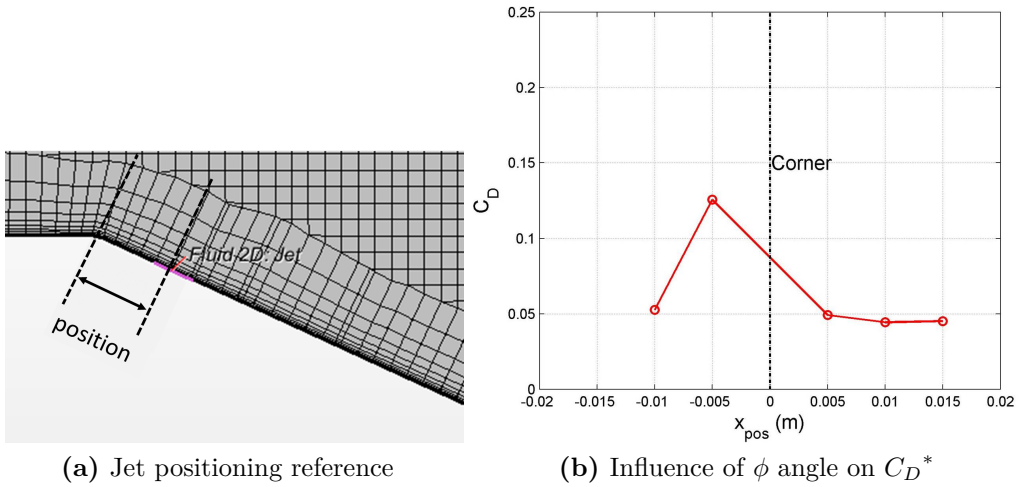


**Figure 3.4:** Influence of  $x_{pos}$  on  $C_D^*$

Posizione [m]	$C_D^*$ $\phi = 15^\circ$
-0.010	0.053
-0.005	0.126
+0.005	0.049
+0.010	0.044
+0.015	0.045

**Table 3.2:** Influence of  $x_{pos}$  on  $C_D^*$

have been run. They consider the same range of position,  $-0.01 \text{ m} \leq x_{pos} \leq 0.015 \text{ m}$ , and other two inflow angles,  $\phi = 5^\circ$  and  $\phi = 15^\circ$  respectively. Data, in terms of  $C_D^*$  variations, are displayed in Figure 3.5 and in Table 3.3. Even if the minimum of  $C_D^*$  occurs for  $x_{pos} = +0.015 \text{ m}$  with  $\phi = 5^\circ$ , there are some practical issues to realize such jet. By the way, another important result is clear: the position at  $+0.005 \text{ m}$  from the corner is the less sensitive to  $\phi$  variations. This consideration is of great interest because, as stated before, it ensure to have beneficial effects on  $C_D$  also in presence of misalignment of  $\phi$ , due to production or mounting issues.

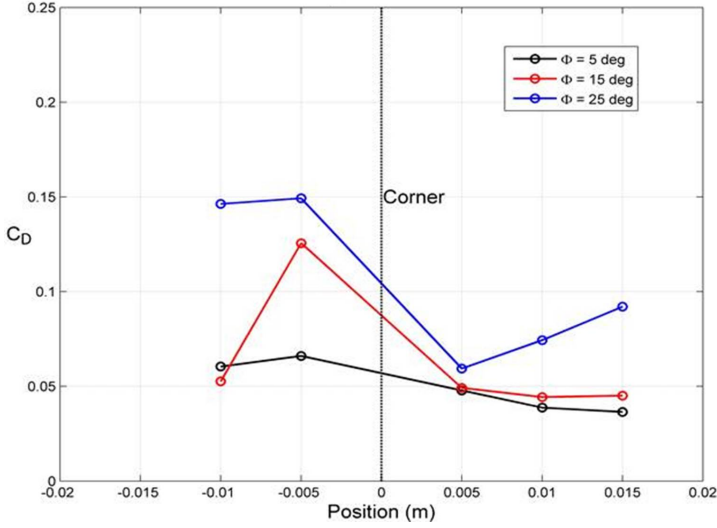


**Figure 3.5:** Cross-effects of  $\phi$  and  $x_{pos}$  on  $C_D$

$x_{pos}$ [m]	$C_D^*$ $\phi = 5^\circ$	$C_D^*$ $\phi = 15^\circ$	$C_D^*$ $\phi = 25^\circ$
-0.010	0.061	0.053	0.146
-0.005	0.066	0.126	0.149
+0.005	0.048	0.049	0.059
+0.010	0.039	0.044	0.074
+0.015	0.037	0.045	0.092

**Table 3.3:** Cross-effects of  $\phi$  and  $x_{pos}$  on  $C_D$

### Minimum effective velocity ( $V_{jet}$ )

Lastly, by means of steady two-dimensional simulations, it has been evaluated the minimum value of jet velocity ( $V_{jet}$ ) which cause the maximum drag reduction. The  $V_{jet}$  value is one of the most important parameter for designing an active control device because it defines the amount of mass flow that the device must provide. Once again, simulations about jet velocity effect have been made keeping constant jet position ( $x_{pos} = +0.005$  m) and inflow angle ( $\phi = 15^\circ$ ). The value of  $\phi$  has been also established considering practical problems in producing smaller  $\phi$  angles. The  $V_{jet}$  velocities have been investigated up to 50 m/s.

Data from simulations suggest that: until  $V_{jet}$  is less than 20 m/s, jet is al-



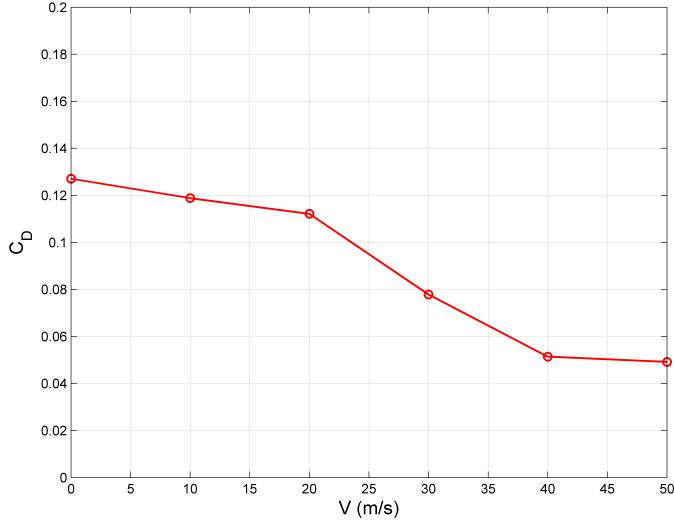


**Figure 3.6:** Jet velocity ( $V_{jet}$ ) effects on  $C_D$

$V_{jet}$ [m/s]	$C_D^*$ $\phi = 15^\circ$
0	0.127
10	0.119
20	0.112
30	0.078
40	0.051
50	0.049

**Table 3.4:** Jet velocity ( $V_{jet}$ ) effects on  $C_D$

most ineffective on reducing  $C_D$ ; jet starts to be effective when  $V_{jet} > 30$  m/s. Furthermore, if the  $V_{jet}$  is higher than 40 m/s, no more drag reduction has been experienced. The  $C_D^*$  curve for various value of  $V_{jet}$  is presented in Figure 3.6, while numerically is listed in Table 3.4.

### 3.2.2 Unsteady jets on Ahmed body

By means of steady two-dimensional simulations, some main characteristics of the active control device have been identified. Steady simulations have proven the capability of a steady jet, with specific parameters, to reduce the wake behind a bluff body, as the Ahmed body, and, consequently,

its pressure drag. Important results of these simulations are:

- the inflow angle has to be smaller as possible, considering production and mounting issues;
- $V_{jet}$  has to be 40 m/s as minimum;
- $x_{pos} = 0.005$  m seems to be the best jet position.

In the light of these, it is possible to introduce another parameter, the frequency  $f$ , which allows to convert a steady jet to unsteady one. The motivation of passing from steady jet to unsteady one is quite simple: generally speaking, a steady jet requires more energy than an equivalent unsteady jet, even if the latter is more complex to realize. Also, unsteadiness generated by such active control device could be beneficial in reducing drag, as documented in [27]. By two-dimensional unsteady simulations, both types of unsteady jet, unsteady blowing jet and synthetic jet, have been compared. Hence, the main scope of these unsteady simulations on 25° rear end Ahmed body is to discover, if it exists, which jet frequency  $f$  could increase drag reduction.

### Unsteady blowing jets on Ahmed body

To simulate an unsteady blowing jet the velocity inlet boundary condition has been slightly modified. Instead of a constant value for velocity magnitude, it has been used a sinusoidal expression to evaluate velocity at each simulation time step. Furthermore, because an unsteady blowing jet is a non-zero mean mass flow device, it has been introduced a mean shift of velocity, namely  $V_m$ . Using results from steady blowing simulations, inflow angle  $\phi$  has been fixed at 10°, while two positions  $x_{pos}$ , at 0.005 m before and after the corner, and several values of frequency  $f$  were investigated. The average value of velocity  $V_m$  has been fixed at 25 m/s, so as the unsteady blowing jet reaches the same maximum value of velocity used for the steady blowing ( $V_{jet} = 50$  m/s). Keeping constant  $V_m$ , the frequency  $f$  has assumed values ranging from 100 Hz up to 500 Hz and, at each simulation time step, velocity  $V(t)$  has been evaluated by the equation (3.1).

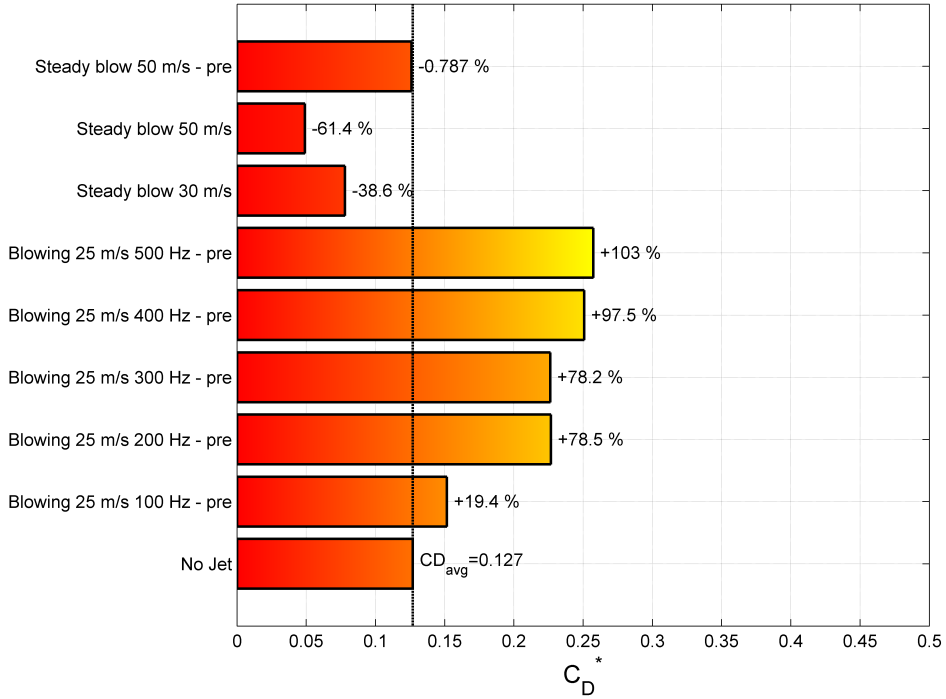
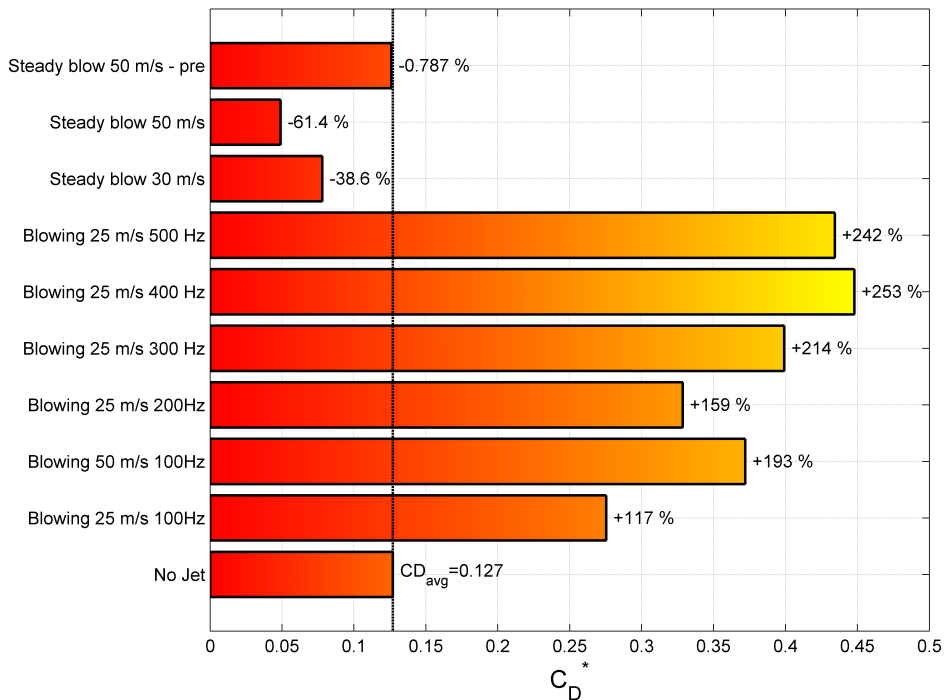
$f$ [Hz]	$ V_m $ [m/s]	$C_D^*$	$\Delta C_D$	$C_D^*$	$\Delta C_D$
		$x_{pos} = -0.005$ m	[%]	$x_{pos} = +0.005$ m	[%]
w/o jet		0.127	-	0.127	-
100	25	0.152	+19.4	0.275	+117
200	25	0.227	+78.5	0.329	+159
300	25	0.226	+78.2	0.399	+214
400	25	0.251	+97.5	0.448	+253
500	25	0.257	+103	0.434	+242

**Table 3.5:** Unsteady blowing - Frequency effects on drag coefficient  $C_D^*$

$$V(t) = V_m (1 + \sin(2 \pi f t)) \tag{3.1}$$

$$\Delta C_D = \frac{C_D^* - C_{Dbase}}{C_{Dbase}} \tag{3.2}$$

Unsteady blowing simulations results are listed in Table 3.5, where  $C_D^*$  variations are also presented as percentage, using the formula (3.2). Comparing results relative to the two jet locations, as depicted in Figure 3.7: data shows that the unsteady blowing jet seems to work better at  $x_{pos} = -0.005$  m than at  $x_{pos} = +0.005$  m, even if it results always detrimental.

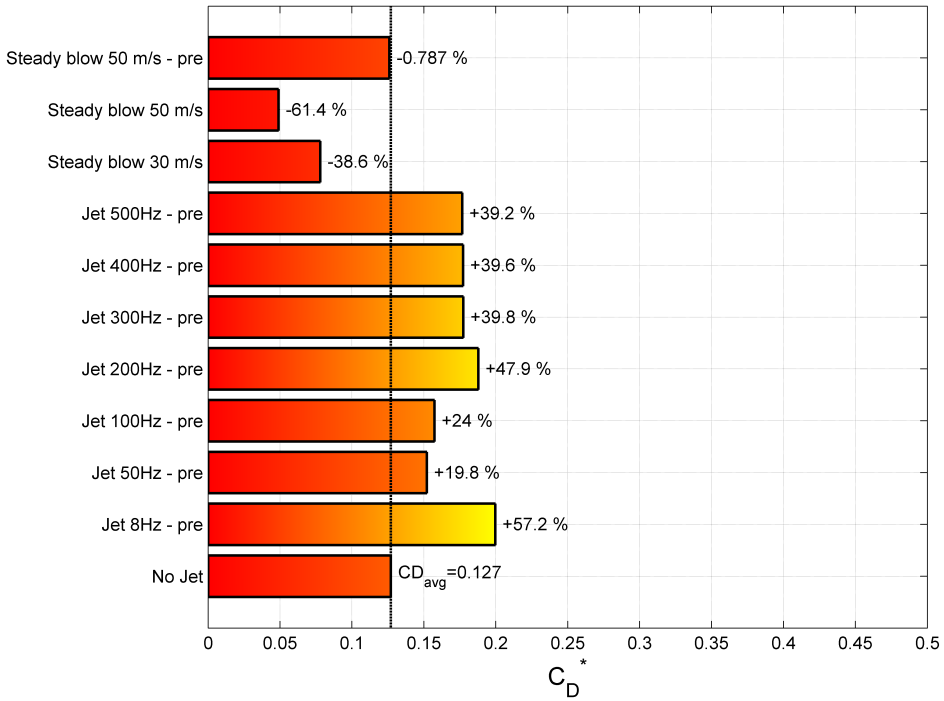
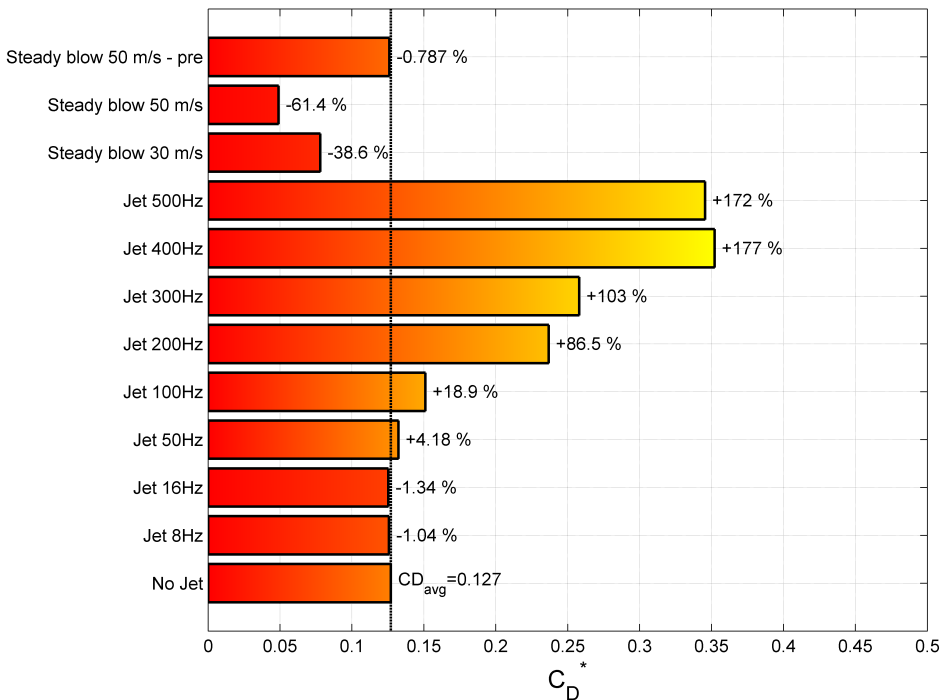
(a) Unsteady blowing at  $x_{pos} = -0.005$  m -  $C_D^*$ (b) Unsteady blowing at  $x_{pos} = +0.005$  m -  $C_D^*$ **Figure 3.7:** Unsteady blowing - Frequency effects on drag coefficient  $C_D^*$

### Synthetic jets on Ahmed body

Similarly to unsteady blowing jet, a sinusoidal wave form has been used for velocity inlet boundary condition to simulate a synthetic jet device. Differently from the unsteady blowing device, a synthetic jet is a system with a zero mass flow rate: thus, the formula (3.1) has been modified into (3.3), considering that  $V_m = 0$  m/s for such device. Also, in order to have, at least, the maximum value of velocity similar to the steady blowing, the  $V(t)$  amplitude has been set as  $V = 50$  m/s.

$$V(t) = V \sin(2 \pi f t) \quad (3.3)$$

This kind of synthetic jet device has been tested in the same locations of the unsteady blowing jet ( $x_{pos} = -0.005$  m,  $x_{pos} = +0.005$  m) and within a range of frequency  $f$  from 8 Hz up to 500 Hz. Data from simulations are listed in Table 3.6, also in percentage terms, and shown in Figure 3.8, for both jet locations. As the unsteady blowing device, the unsteadiness generated by these kinds of jets have detrimental effects on drag reduction and drag increment is larger for higher value of jet frequency. Also, the position before the corner ( $x_{pos} = -0.005$  m) seemed to cause a lower drag increment.

(a) Synthetic jet at  $x_{pos} = -0.005$  m -  $C_D^*$ (b) Synthetic jet at  $x_{pos} = -0.005$  m -  $C_D^*$ **Figure 3.8:** Synthetic jet - Frequency effects on drag coefficient  $C_D^*$

$f$ [Hz]	$C_D^*$	$\Delta C_D$ [%]	$C_D^*$	$\Delta C_D$ [%]
	$x = -0.005 \text{ m}$		$x = +0.005 \text{ m}$	
w/o jet	0.127	-	0.127	-
8	0.200	+57.2	0.126	-1.04
16	-	-	0.125	-1.34
50	0.152	+19.8	0.132	+4.18
100	0.151	+18.9	0.158	+24
200	0.188	+47.9	0.237	+86.5
300	0.178	+39.8	0.258	+103
400	0.177	+39.6	0.352	+177
500	0.177	+39.2	0.346	+172

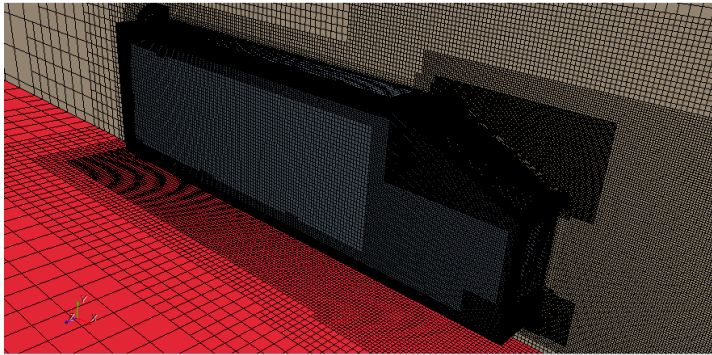
**Table 3.6:** Synthetic jet - Frequency effects on drag coefficient  $C_D^*$

Anyway, although two-dimensional simulations could be useful in the identification of more effective jet parameters for drag reduction, it has to be remembered that the bluff body flow field is strongly three-dimensional. In fact, as expected, two-dimensional simulations were capable to account effects related to skin friction drag and pressure drag, but they provide no information about other drag mechanism, as lift induced drag, which is a typical three-dimensional effect. In the light of this, the damaging effect of unsteady device, recognized by means of two-dimensional simulations, could be positive on controlling lift induced drag and, so, reducing overall body drag. Hence, final sentences about device effectiveness in reducing drag cannot be made without several, more expensive, three-dimensional simulations.

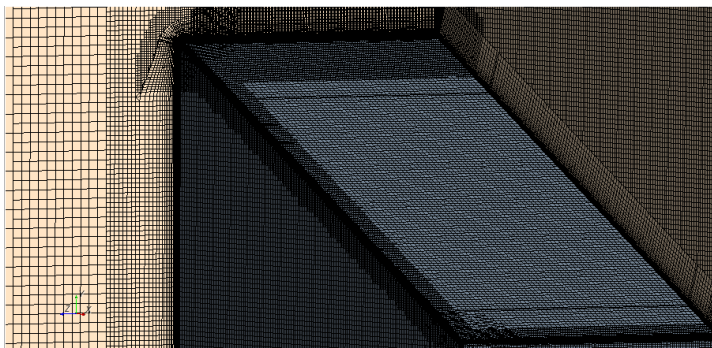
### 3.3 Three-dimensional simulations on $25^\circ$ rear end Ahmed body

Three-dimensional simulations on  $25^\circ$  rear end Ahmed body have been performed to discover, if it exists, an operating condition for unsteady jets to reduce body drag.

Due to symmetry proprieties of both Ahmed body and computational



(a) Three-dimensional mesh overview



(b) Mesh details around the Ahmed body

**Figure 3.9:** Some details of the three-dimensional computational domain

domain, it is possible to simulate only one half of the overall domain, reducing the time and computational expensiveness of such simulations. Boundary conditions used are the same reported in Figure 3.1, except that for the symmetry plane, where symmetry plane boundary condition has been disposed. This boundary condition, available in Star-CCM+, is almost similar to a slip wall condition, not allowing for velocity components through the plane. Despite this, computational domain counts about 14 millions of cells in order to be sure to catch complex three-dimensional phenomena. Some pictures of the computational domain are shown in Figure 3.9: in these images, refinements around the Ahmed body and for the boundary layer are clearly visible.

Comparing two-dimensional flow field (Figure 3.10a) with three-dimensional one on the symmetry plane (Figure 3.10b), it can be observed, both on the front and on the rear of the Ahmed body, how the flow distribution



change: it is almost clear that a new flow expansion appears in the front of the Ahmed body, in its lower part, and that the wake extension is shorter. Probably, both effects have to be accounted to the cross-flow in the body width, which causes also the development of tip vortices. In fact, the Ahmed body can be also referred as a finite wing, with a very low aspect-ratio, for which tip vortices are very strong (as it is probably known, lower is the aspect-ratio, stronger are tip vortices and higher the amount of lift induced drag). Ultimately, the reduction of wake length, due to tip vortices, suggests the beneficial effect of such vortices for decreasing pressure drag; however, their presence is a clear indication of another drag contribution, well known as lift induced drag. Each one of these contributions should be controlled to reduce the overall body drag.

For reducing the number of three-dimensional simulations to be performed, some indications about unsteady jet have been extracted by two-dimensional simulations. Nevertheless, the needs of producing a suitable system, for subsequent wind tunnel testing, have pointed out issues related to mass flow rate and energy: so, the outlet shape of the system has been modified to be as simple as possible, for producing purpose; also, its width has been reduce to decrease mass flow and energy supply demand. The chosen outlet shape has been rectangular and its dimensions are:  $0.379\text{ m} \times 0.002\text{ m}$ . The chosen width of  $0.002\text{ m}$  is more likely the typical dimension of a synthetic jet, instead of  $0.005\text{ m}$  used for the two-dimensional simulations. About the device length of  $0.379\text{ m}$ , it determines an outlet section for the unsteady device which extends for about 90% of the Ahmed body width. Finally, to further reduce the energy and mass flow device, it has been used a  $V = 40\text{ m/s}$ , as maximum value, instead of  $V = 50\text{ m/s}$ .

In Table 3.7 are listed three-dimensional simulations results relative to the unsteady blowing jet, while the data relative to the simulations with synthetic jet are summarized in Table 3.8. While simulations with synthetic jet consider only variations of frequency  $f$ , simulations with unsteady blowing investigate both different values of frequency  $f$  and inflow angle  $\phi$ . For both jet type, two jet positions,  $x_{pos} = -0.005\text{ m}$  and  $x_{pos} = 0.005\text{ m}$ , have been compared.

Unsteady blowing $V =  V_{sin(2\pi ft)}  +  V_m $	$ V_m $ [m/s]	$\phi$ [°]	$f$ [Hz]	$x_{pos}$ [m]	Slot width [m]	$C_D^*$
..UB20_a10_f100.sim	20	10	100	+0.005	0.002	0.242
-	20	10	100	-0.005	0.002	-
..UB20_a10_f200.sim	20	10	200	+0.005	0.002	0.244
-	20	10	200	-0.005	0.002	-
..UB20_a20_f100.sim	20	20	100	+0.005	0.002	0.246
..UB20_a20_f100_pre.sim	20	20	100	-0.005	0.002	0.256
..UB20_a20_f200.sim	20	20	200	+0.005	0.002	0.244
..UB20_a20_f200_pre.sim	20	20	200	-0.005	0.002	0.240
(Maximum) Mass flow rate: $\dot{m} = \rho VA = 0.0371$ kg/s				$C_D^*_{base}$	0.280 (0.3 s)	
(Average) Mass flow rate: $\dot{m} = \rho V_{m,A} = 0.0186$ kg/s				$C_D^*_{base}$	0.272 (0.4 s)	
Device outlet section: rectangular slot - 0.379 m × 0.002 m						

**Table 3.7:** Unsteady blowing - Three-dimensional simulations summary

Synthetic jet $V =  V  \sin(2\pi ft)$	$ V $ [m/s]	$f$ [Hz]	$x_{pos}$ [m]	Slot width [m]	$C_D^*$
..SJ_40_250.sim	40	250	+0.005	0.002	0.236
–	40	250	–0.005	0.002	–
..SJ_40_350.sim	40	350	+0.005	0.002	0.242
..SJ_40_350_pre.sim	40	350	–0.005	0.002	0.332
..SJ_40_450.sim	40	450	+0.005	0.002	0.250
–	40	450	–0.005	0.002	–
..SJ_40_550.sim	40	350	+0.005	0.002	0.296
–	40	350	–0.005	0.002	–

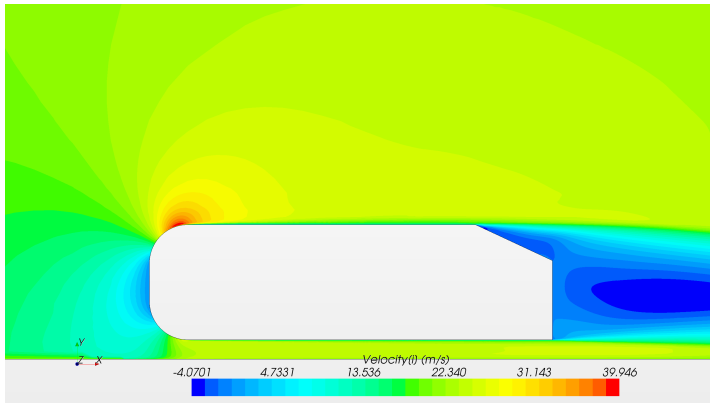
(Average) Mass flow rate:  $\dot{m} = \rho VA = 0.0371 \text{ kg/s}$

Device outlet section: rectangular slot – 0.379 m × 0.002 m

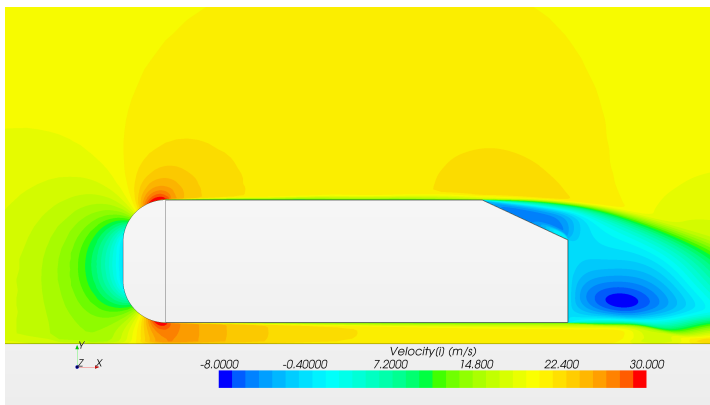
$C_{D^*}^{base}$  0.280 (0.3 s)

$C_{D^*}^{base}$  0.272 (0.4 s)

**Table 3.8:** Synthetic jet - Three-dimensional simulations summary



(a) Horizontal velocity component - 2D simulation



(b) Horizontal velocity component, on symmetry plane - 3D simulation

**Figure 3.10:** Flow field comparison between two-dimensional and three-dimensional simulations

The  $x_{pos} = +0.005$  m has shown that:

- the most effective condition for a synthetic jet has been obtained when  $f = 250$  Hz;
- an unsteady blowing jet with  $f = 100$  Hz is almost insensitive to  $\phi$  variations;
- an unsteady blowing jet with  $f = 200$  Hz is totally insensitive to  $\phi$  variations.

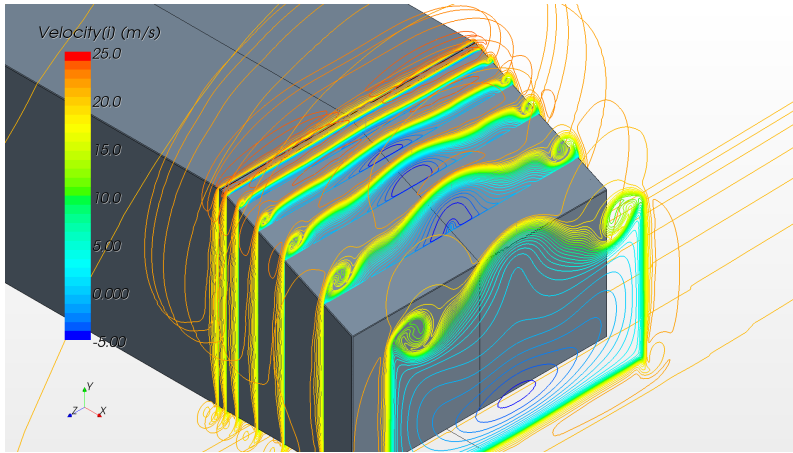
In Figure 3.11 and in Figure 3.12 velocity and vorticity streamlines, on several planes located near the Ahmed body rear end, are shown: they are

compared with the same streamlines in the clean configuration, with the aim to identify some flow features interested by the unsteady control jets. As can be seen from these pictures, it seems that, while unsteady blowing reduces visibly the separation on the slanted surface, the synthetic jet creates unsteadiness which effects more tip vortices than separation. More clearly these considerations can be inferred from Figure 3.13 and Figure 3.14, for the unsteady blowing and for the synthetic jet respectively. These maps show a comparison of velocity contours on several planes, located near the Ahmed body rear end. These planes are:

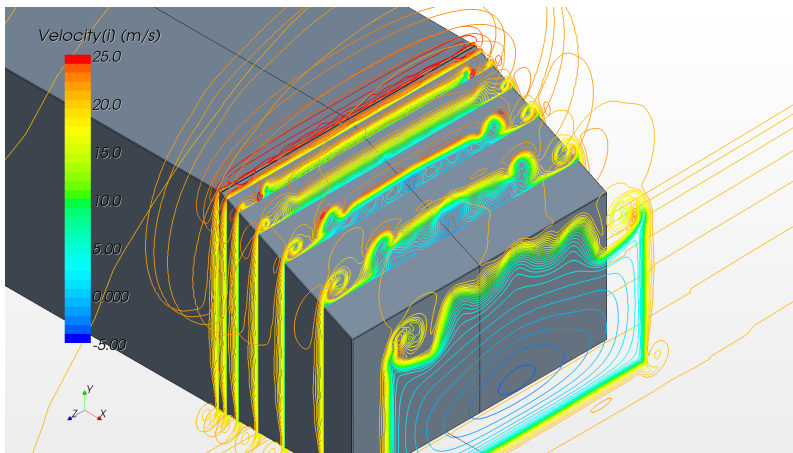
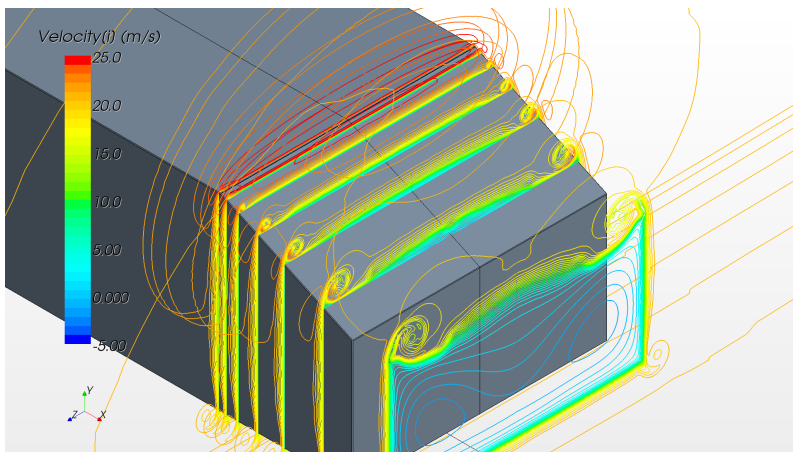
- Plane 1:  $\bar{x} = 0.860$  m;
- Plane 2:  $\bar{x} = 0.893$  m;
- Plane 3:  $\bar{x} = 0.943$  m;

where  $\bar{x}$  is used to denote the distance of the plane from the Ahmed front. The Figure 3.13 and the Figure 3.14 have, on the right, velocity contours relative to the unsteady device in operation, while, on the left, they present the same contours relative to the condition without control device. From these, it is evident that the unsteady blowing reduce both separation and tip vortices, while the synthetic jet creates less coherent structures, which effects are drag reduction. Using a formula similar to (3.2), it is possible to estimate that, in optimal unsteady jet operating condition, the synthetic jet is capable to produce a drag reduction of about 13%, while the unsteady blowing is capable of about 11% of drag reduction.

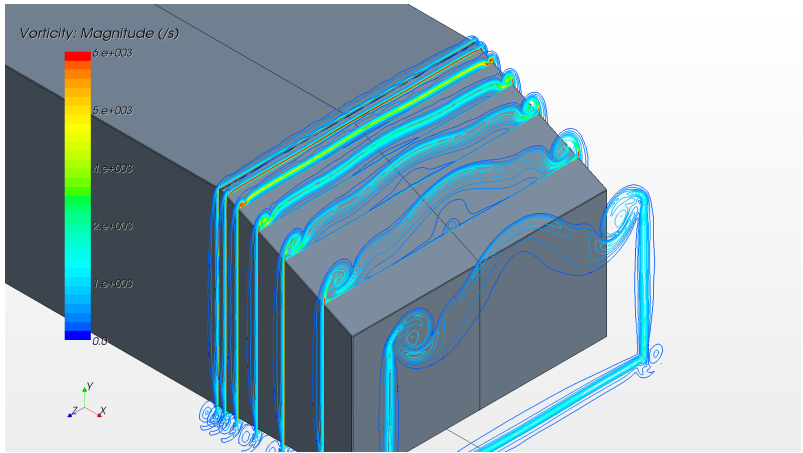
The considerations extracted from these numerical simulations, as anticipated in § 2, have been very useful for the production of unsteady device tested into the wind tunnel facility.



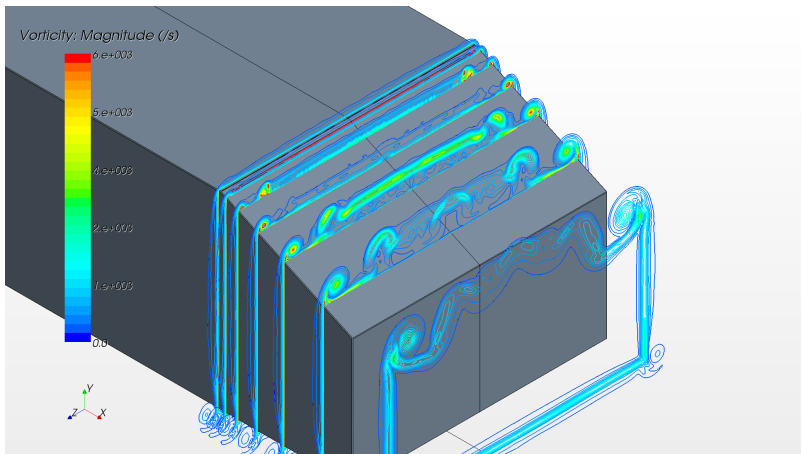
(a) w/o unsteady control device

(b) Synthetic jet, with  $f = 250$  Hz and  $V_{max} = 40$  m/s(c) Unsteady blowing, with  $f = 200$  Hz and  $\alpha = 20^\circ$ 

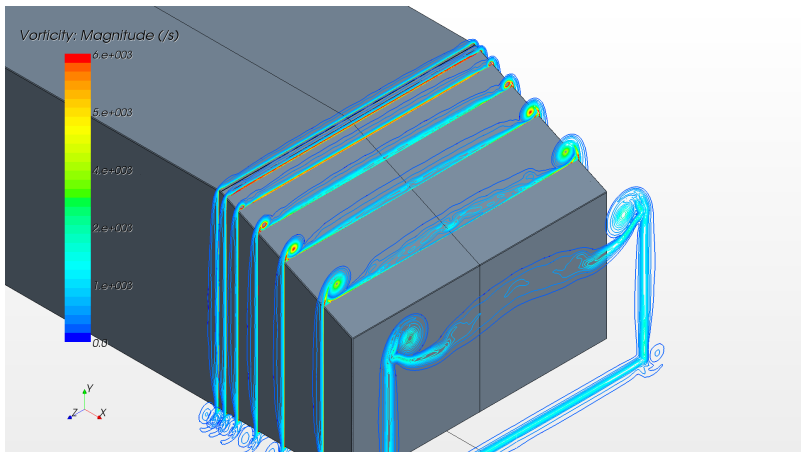
**Figure 3.11:** Velocity streamlines on several planes, during optimal operating conditions



(a) w/o unsteady control device

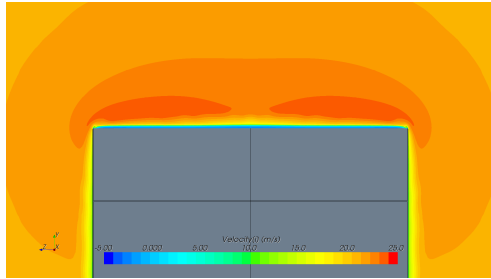


(b) Synthetic jet, with  $f = 250$  Hz and  $V_{max} = 40$  m/s

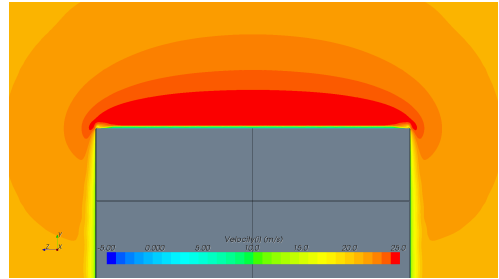
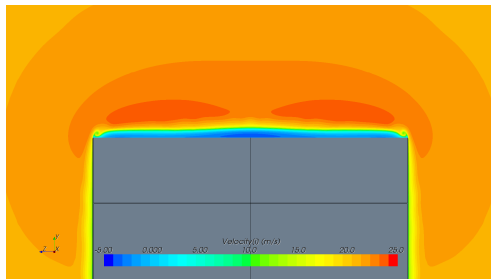


(c) Unsteady blowing, with  $f = 200$  Hz and  $\alpha = 20^\circ$

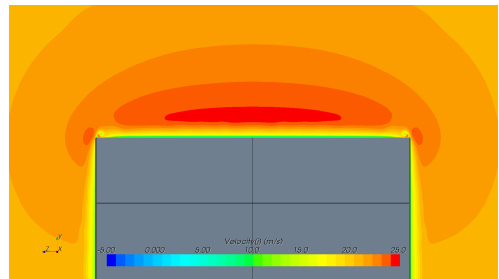
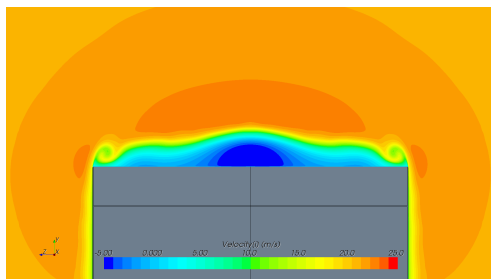
**Figure 3.12:** Vorticity streamlines on several planes, during optimal operating conditions



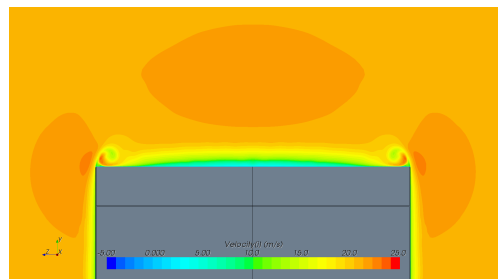
(a) Plane 1 - w/o unsteady control device

(b)  $f = 200 \text{ Hz}$ ,  $\alpha = 20^\circ$ 

(c) Plane 2 - w/o unsteady control device

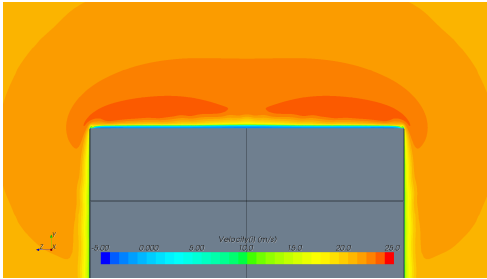
(d)  $f = 200 \text{ Hz}$ ,  $\alpha = 20^\circ$ 

(e) Plane 3 - w/o unsteady control device

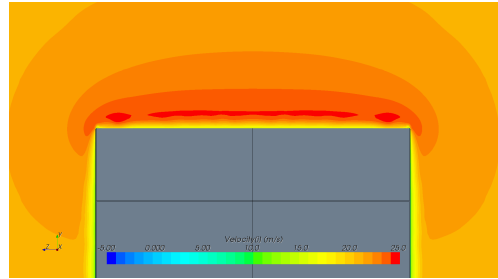
(f)  $f = 200 \text{ Hz}$ ,  $\alpha = 20^\circ$ 

**Figure 3.13:** Comparison of velocity contours on several planes - Unsteady blowing

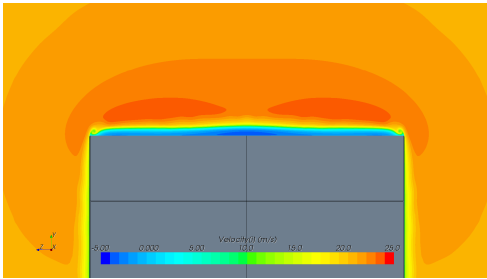




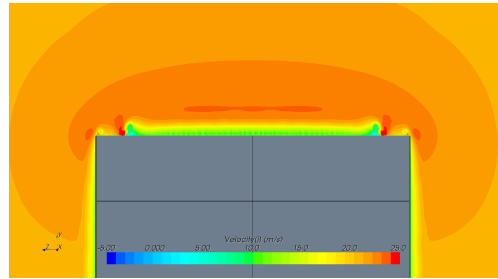
(a) Plane 1 - w/o unsteady control device



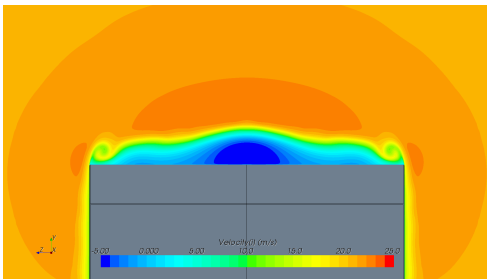
(b)  $f = 250$  Hz,  $V_{max} = 40$  m/s



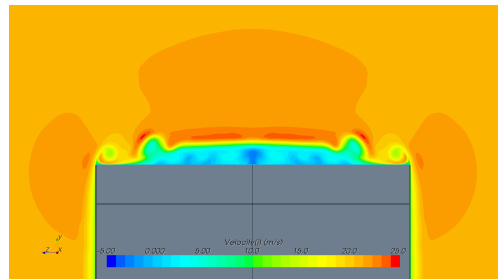
(c) Plane 2 - w/o unsteady control device



(d)  $f = 250$  Hz,  $V_{max} = 40$  m/s



(e) Plane 3 - w/o unsteady control device



(f)  $f = 250$  Hz,  $V_{max} = 40$  m/s

**Figure 3.14:** Comparison of velocity contours on several planes - Synthetic jet

## 3.4 Three-dimensional simulations on 35° rear end Ahmed body

This set of CFD simulations have been performed after the first experimental tests on the 35° Ahmed body model with the aim of better understand flow phenomena observed during wind tunnel tests. So, these simulations are not intended to give some numerical estimation of 35° rear end Ahmed body drag, but only a more exhaustive insight on flow field due to the activation of unsteady control device.

As it will be explained more extensively in § 4, during early experimental tests, it has been observed that, differently from 25° rear end Ahmed body, unsteady control device activation causes drag increase of 35° rear end Ahmed body. By means of tufts installed over the slanted surface, a curious effect has been observed: before the jet activation, the flow is completely detached from the rear end of the Ahmed body and no tip vortices are present; when the jet is activated, the flow reattaches and vortices start from Ahmed body tips. Also, at the same time, when tip vortices appear, 35° rear end Ahmed body drag increases widely. So, remembering that Ahmed body behaves like a very low aspect-ratio wing, it is not wrong to assume that tip vortices are strictly connected to generation of lift force and, also, the related lift induced drag. Hence, the drag increase is most likely due to the lift induced drag presence.

In Figure 3.15, it is shown an unsteady simulation solution on 35° rear end Ahmed body. This picture shows some streamlines around the body rear: the red ones are relative to the case without unsteady control device, while the blue ones are for the case with unsteady control device. Comparing these, the tip vortices development is evident between the two cases; also, the drag ( $C_D$ ) and lift ( $C_L$ ) coefficients trend, reported above, highlights as the tip vortices cause a both increase of lift and drag, justifying the hypothesis of an increase in induced drag. In fact, induced drag increase is strictly related to the square of the absolute value of lift, which is almost null in the case without unsteady jet configuration. The simulated unsteady control device is an unsteady blowing jet type (eq. (3.1)), with  $V_m = V = 20$  m/s

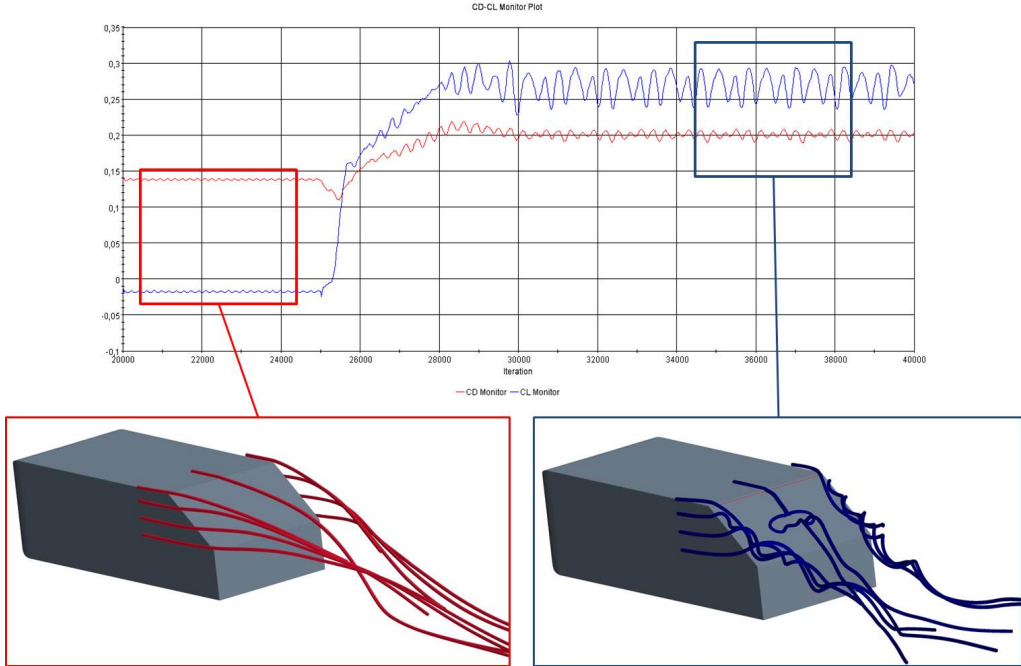


**Figure 3.15:** Time history of a simulation on 35° rear end Ahmed body

and  $f = 50/s$ , with  $\phi = 10^\circ$ . Activating the control jet, the value of lift increases and, similarly, the induced drag;  $C_D$  of the solution with active control device is about 40% larger than the  $C_D$  without active control device, while the  $C_L$  increase is much larger. It has to be noticed that  $C_D$  and  $C_L$  values in Figure 3.15 must be doubled, because, in the simulations, it has been used the whole Ahmed body frontal area as reference for force coefficients, while simulations have been performed only on one half of it. In Figure 3.16, the velocity distributions in the wake are compared for the cases without and with unsteady control device. These pictures show the positive effect of the unsteady jet device of reducing separation zone in the symmetry plane of the Ahmed body, but, also, the detrimental effect due to vortices.

$$C_{Di} = \frac{C_L^2}{\pi AR e} \tag{3.4}$$

To estimate the induced drag contribution is possible to use the well known equation in (3.4), which relates induced drag coefficient  $C_{Di}$  to lift

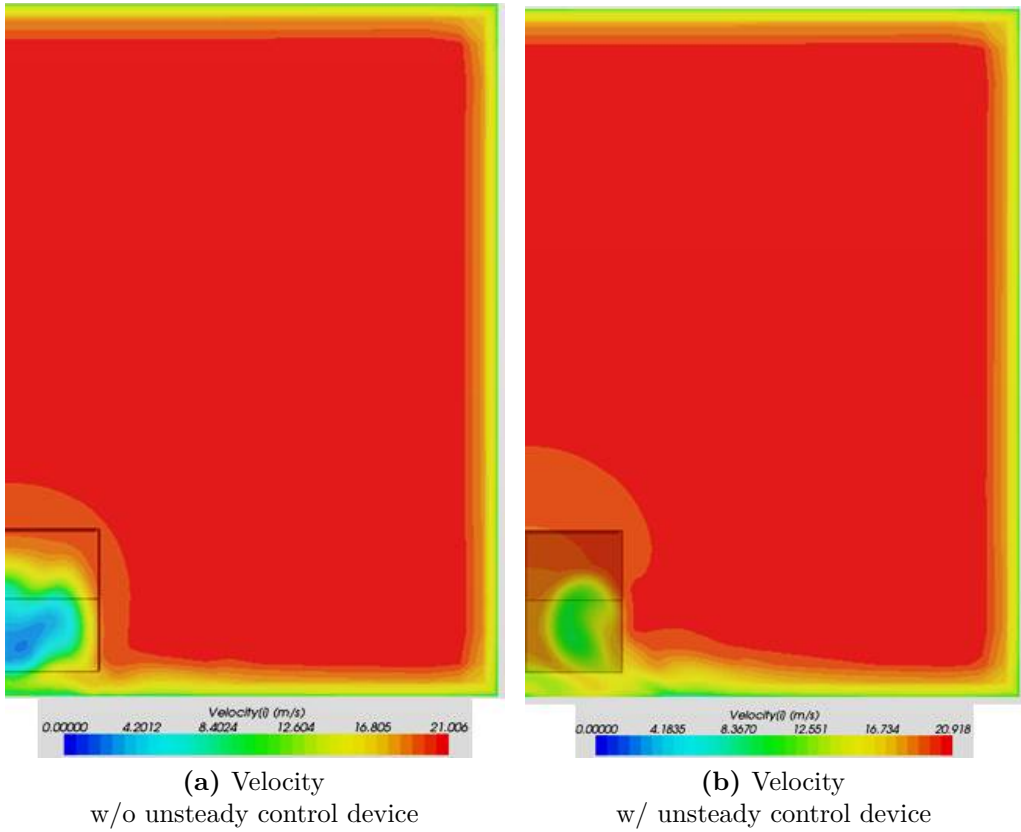


**Figure 3.16:** Wake distributions of a 35° rear end Ahmed body

coefficient  $C_L$ , body aspect ratio  $AR$  and Oswald factor  $e$ : so, to use this formula, it is necessary to suppose a value for the so-called Oswald factor  $e$ . A method to estimate the Oswald factor is provided in [35] and depicted in Figure 3.17: this picture suggests that, when  $AR$  is particularly low, the Oswald factor  $e$  reaches a limit value of about 0.96. Hence, considering that Ahmed body  $AR$  is 0.373 and  $C_L$  is about 0.275, it results  $C_{Di} = 0.068$  using a value of  $e = 0.95$ . This value of  $C_{Di}$  is acceptable supposing that, as for the 25° rear end Ahmed body, a 10% of drag reduction occurs due to flow reattachment in the Ahmed body symmetry. The calculus of the  $C_{Dw/j}$ , in the case of active control deployed, is reported in equation (3.5), along with the estimated value of induced drag coefficient  $C_{Di}$ .

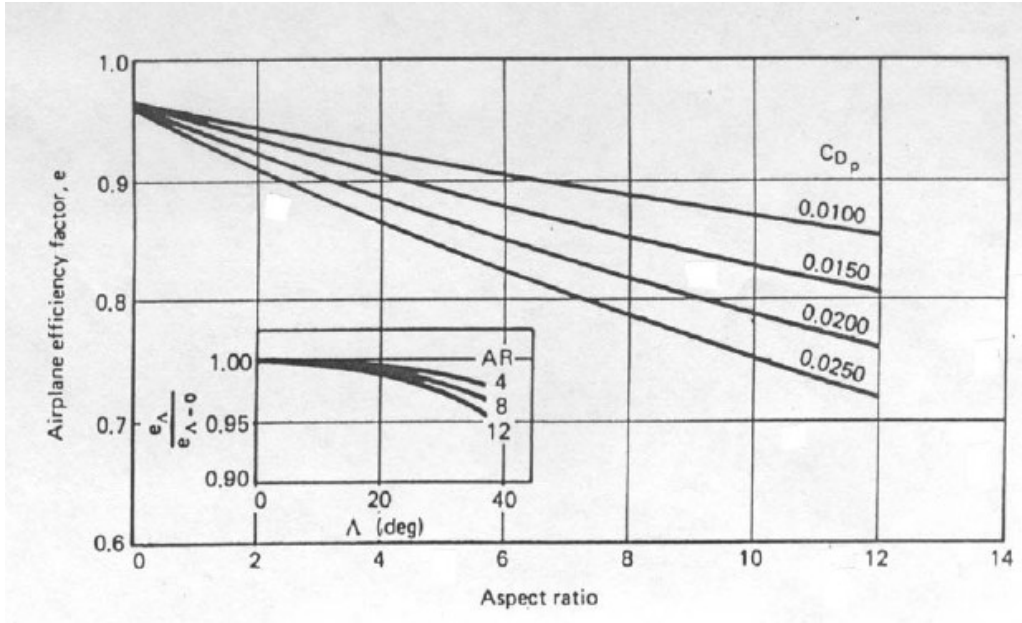


Figure 3.17: Oswald factor vs. Aspect ratio

$$C_{Dw/j} = C_{Di} + C_{Df} + C_{Dp} = C_{Di} + 0.90 C_{Dw/oj} = 0.068 + 0.126 = 0.194 \quad (3.5)$$

where  $C_{Di}$  is the induced drag coefficient,  $C_{Df}$  and  $C_{Dp}$  are skin friction and pressure drag coefficients,  $C_{Dw/oj}$  and  $C_{Dw/j}$  are, respectively, overall drag coefficients, without and with active control device deployed. Finally, it has to be remembered that these values are referred to only an half of Ahmed body and, thus, they have to be doubled.

### 3.5 Three-dimensional simulations on a FIAT Punto Classic

As anticipated in § 2.2, unsteady control devices were also tested on a simplified car model in order to investigate their effectiveness on a shape more similar to a common car. In fact, while the Ahmed body allows to

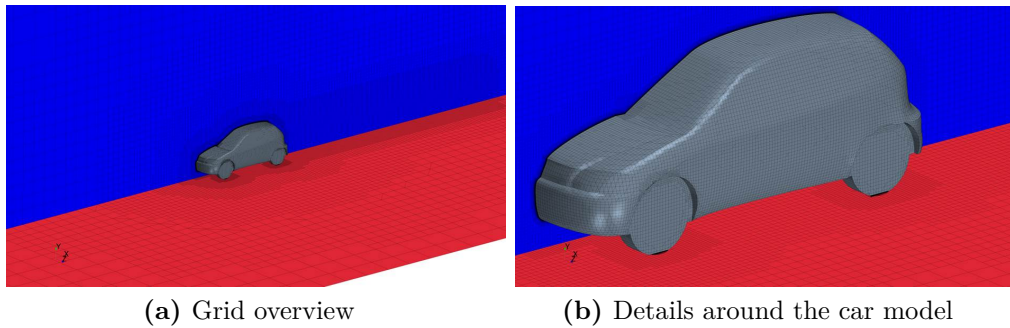


**Figure 3.18:** FIAT Punto model computational grid

well understand flow in the rear of a different car model, it does not account effects of the front shape to the flow over the rear. The influence of the front could not be forgotten, as that of the diffuser, the rolling tyres and other car components.

The FIAT Punto Classic in Figure 2.6b has been used for some CFD simulations. The mesh used for the simulations on the FIAT Punto model is shown in Figure 3.18. As for simulations on  $35^\circ$  rear end Ahmed body, a less heavy computational grid has been used than that used for  $25^\circ$  rear end Ahmed body. Recognizing similarities between the FIAT Punto model and the  $35^\circ$  rear end Ahmed body, simulations have been used only to verify this similitude; so, summarizing, they have confirmed such similarities between the flow field of the FIAT Punto Classic and the one of the  $35^\circ$  rear end Ahmed body; so,

In Figure 3.19 are presented some flow field visualizations obtained from CFD simulations. These point out stagnations points and expansions as expected, along with a large separation behind the car model. The separation zone behind the car it's more evident in Figure 3.21: with the help of velocity contours and streamlines, it is evident how the flow behind the FIAT Punto Classic, in clean configuration, is widely separated; also, effect of the car front is evident: in fact, comparing streamlines of FIAT Punto Classic with those of the  $35^\circ$  rear end Ahmed body, it is evident that some rotational effects are present. Using the control device, of synthetic jet type with  $V = 40$  m/s,  $f = 100$ /s and  $\phi = 20^\circ$ , to the rear end surface,

the separation behind the car reduces, even if the flow seems to be more rotational than before (Figure 3.22).

In terms of non-dimensional coefficients, increase of average values of both  $C_L$  and  $C_D$  (respectively,  $C_y$  and  $C_x$  in Figure 3.22 and in Figure 3.22) have been noticed: as can be seen from Figure 3.20, coefficients behaviour is very similar to that found on  $35^\circ$  rear end Ahmed body; numerically, drag coefficient  $C_D$  ( $C_x$ ) increase, due to control device using, is about 11%, while lift coefficient  $C_L$  ( $C_y$ ) is almost doubled. Hence, as for the  $35^\circ$  rear end Ahmed body, a possible reason of this could be the induced drag increment. Using equation (3.16b), with the same value of  $e$ , since  $AR = \frac{0.965\text{ m}}{0.400\text{ m}} = 0.386$ , induced drag coefficient value results  $C_{Di} = 0.018$  and  $C_{Di} = 0.069$ , respectively before and after active control device deployment.

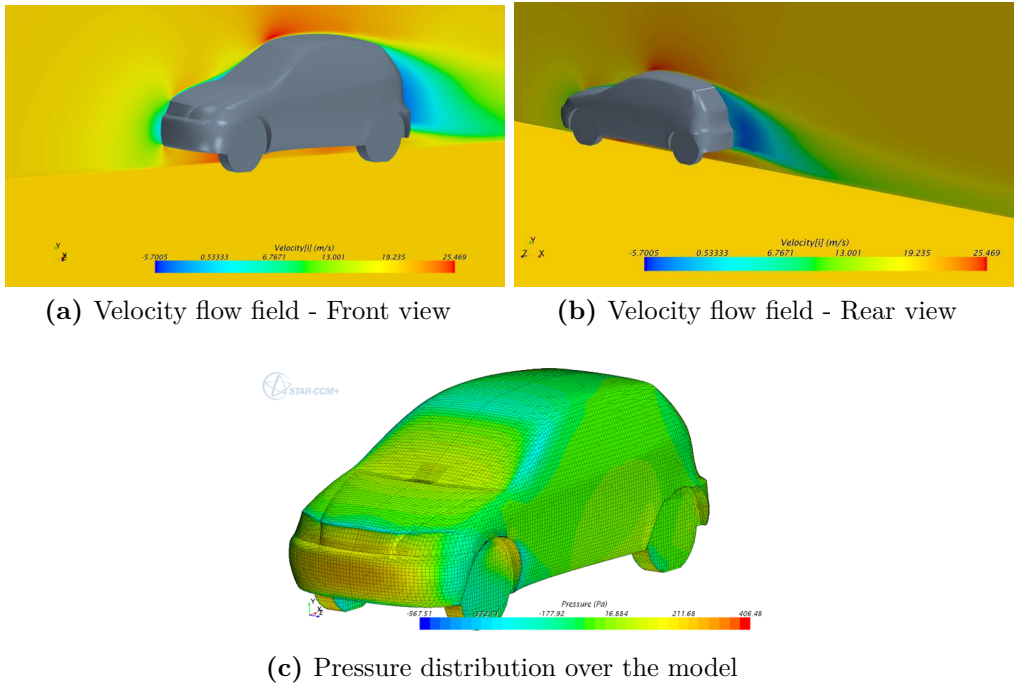


**Figure 3.19:** Some flow visualizations around the FIAT Punto model in clean configuration

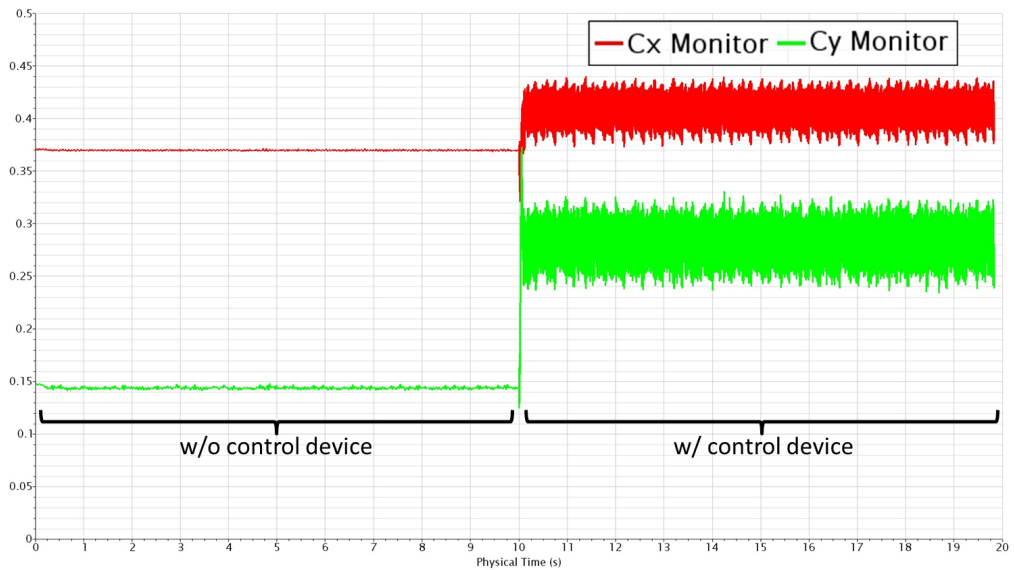
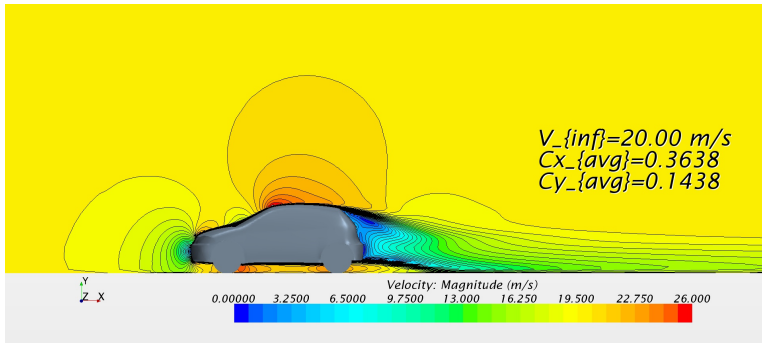
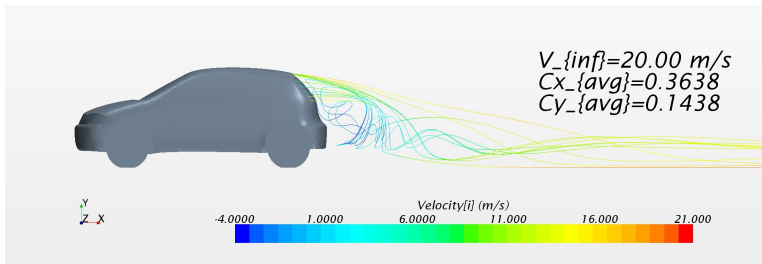


**Figure 3.20:** FIAT Punto Classic - Force coefficients history

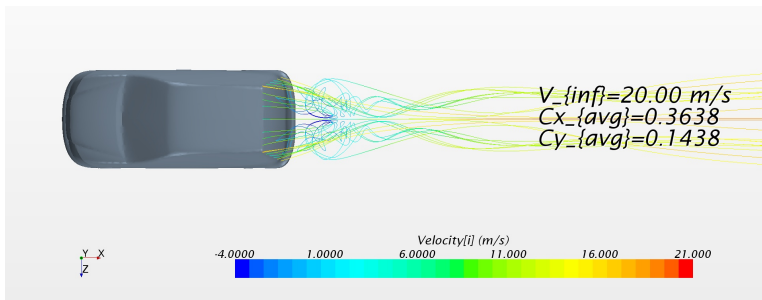




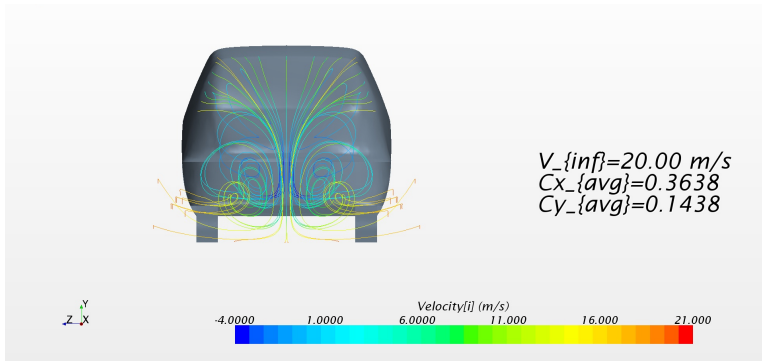
(a)



(b)

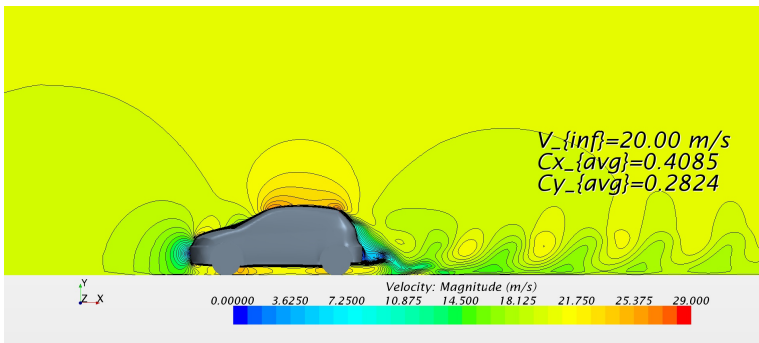


(c)

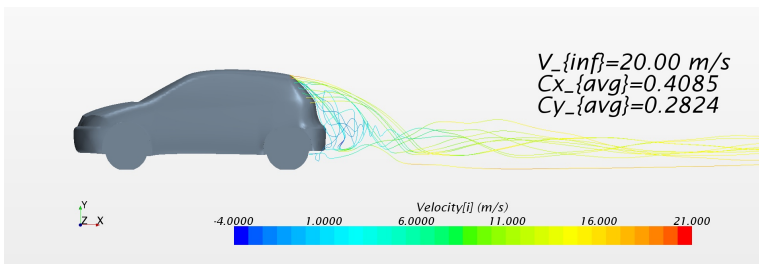


(d)

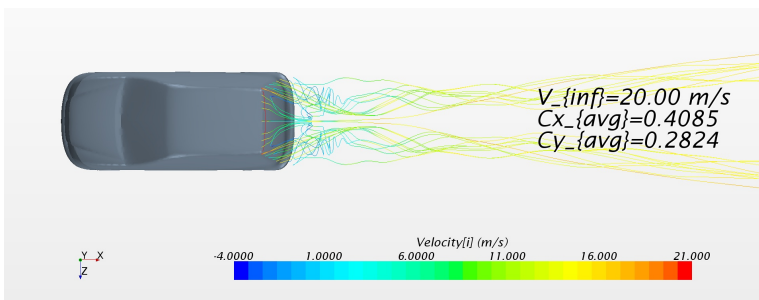
Figure 3.21: Streamlines visualizations - FIAT Punto model w/o control device



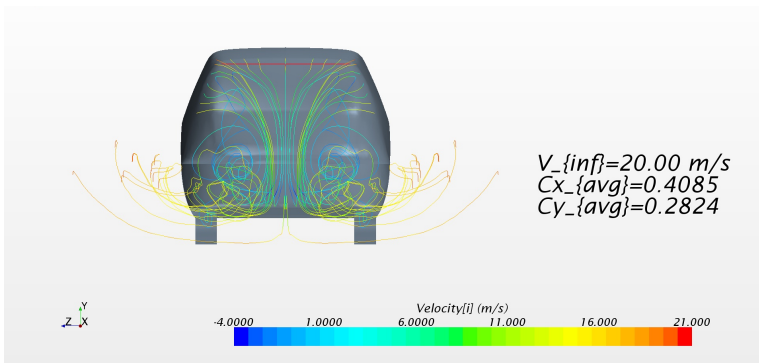
(a)



(b)



(c)



(d)

**Figure 3.22:** Streamlines visualizations - FIAT Punto model w/ control device



---

## Wind tunnel experimental tests

---

Experimental test campaign has been performed using the wind tunnel facility of the University of Naples Federico II. The facility is located at the Industrial Department, Aerospace section, in Naples. It is a closed loop wind tunnel with a closed test chamber (see Figure 4.1). Test chamber dimensions are: 1.4 m of height and 2 m of wide. Actually, the wind tunnel is capable of producing flow velocity, in test chamber, up to 45 m/s. During the years, turbulence level has been monitored and its values is about 0.1%.

### 4.1 Experimental tests measurement equipments

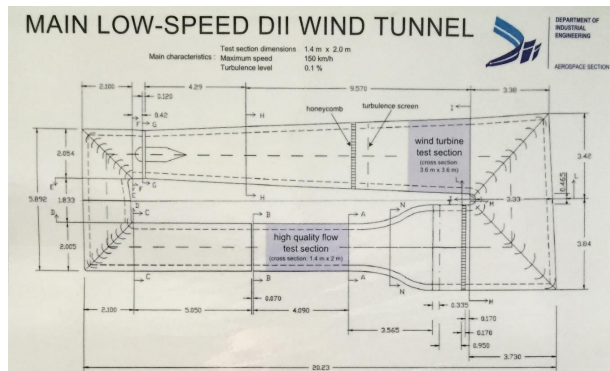
For testing, wind tunnel and model are equipped with some measurements instruments, briefly listed and described below. Among these, some are useful mainly for qualitative flow understanding, while some others are quantitative.

#### Wool tufts

The technique of using tufts is a very consolidate practice, mainly in the aerospace field, to understand qualitatively flow development around and on a body. It consists in placing a large number of short pieces of wool on the body surface: these taped wool pieces (tufts) could be of different



(a)



(b)

Figure 4.1: Wind tunnel facility of the University of Naples

lengths and, due to their low weight, are able to align with the local velocity vector. In this way, the experimenter can observe how is the local velocity distribution around a body, distinguishing between attached flow areas to separated ones. So, tufts are disposed in the considered most relevant areas of the model. Wool tufts have been used for all the experimental tests reported here as a first way of investigation about flow field behaviour.

### Oil Film

Oil film consists on painting some parts of the model with a very viscous fluid, e.g. oil, in order to visualize velocity distribution on painted surface. This technique uses flow wall shear stress to redistribute oil on the surface, visualizing areas in which shear stress is lower: in fact, low shear stress

value suggests flow of imminent separation or flow reattachment, in the case of a laminar separation bubble; also, it allows to identify presence of vortices. Hence, as the previous, oil film is a qualitative method for investigating flow behaviour. For the scope of this thesis, oil film has been used only for the Ahmed body: while, for the  $25^\circ$  rear end Ahmed body, there is no appreciable evidences on oil film distributions between without and with active control device cases, for the  $35^\circ$  rear end Ahmed body, it results a good method to compare oil film distribution between the two configurations.

### Particle Image Velocimetry (PIV)

To investigate flow fields around and behind a body, Particle Image Velocimetry (PIV) can be used. PIV is a quite complex technique which uses a series of flow field images to determine the more plausible particle tracks. To perform PIV measurements it is necessary to seed the flow around the body with high reflective particles; laser beam lights up these particles and their reflections are captured with high speed cameras. As a minimum, two images with a known time interval are necessary to perform PIV: in fact, comparing these two images and using the cross-correlation method, particle track can be reconstructed. Thus, difficulties of PIV technique are strictly connected to the needs of having high quality flow images, with high level of signal-to-noise ratio, for the purpose of discerning particle reflections to other spurious light sources. Some PIV analyses have been performed during experimental test campaign, both for evaluate flow in the symmetry plane and also for wake survey purpose.

### Load cells

The more simple way to quantitatively estimate forces on a test model is to use load cells. Load cells are strain-gauges equipped devices which can sense relative motions between a fixed frame, e.g. wind tunnel frame, and the tested model. Tested model motions are due to flow passing over the model and, usually, are very very small. Thus, the link between model under

test and fixed frame is made up only by load cells; to increase sensitivity, as well as to measure several force components, load cells can be arranged in a package known as force balance. So, before using such devices, it is necessary to calibrate the force balance, for each force component, and to reset the force balance signal before each measurement: in this way, measurement reliability and accuracy can be guaranteed. In this work, data from load cells have been used as the main reference for active device performance evaluation.

### **Hotwire**

Hotwire measurements are usually used to evaluate flow velocity. Hotwire principle is based on Joule effect: temperature variations on a wire, due to the flow in which it is disposed, cause a voltage changes across the wire and, then, these changes are correlated to a value of flow velocity, by means of a calibration curve. So, a control unit tries to keep wire temperature as constant as possible and, meanwhile, measures voltage changes. Hotwire measurements are necessary in all phenomena where flow velocity changes rapidly and you want to measure these fluctuations. The real weak point of these instrumentations is their fragility: the wire is extremely thin in order to reduce thermal inertia and, thus, to be more sensitive to flow velocity changes. Therefore, wire breaks are very frequent issues for such devices. Hotwire measurements have been used during experimental tests to characterize active control devices in terms of velocity and frequency.

### **Pressure probes**

A more classical way to know flow velocity is to measure the related dynamic pressure: using Bernoulli equation, it is possible to relate pressure to velocity and vice versa. Usually, pressure based flow velocity measurements are made with the so-called Pitot tube: a Pitot tube is a pressure probe of particular shape, with some holes, able to measure simultaneously static and total pressure. Static pressure holes are arranged to have their axis perpendicular to the flow field, while total pressure holes have their axis

aligned with flow field main velocity. The pressure difference between static and total pressure is equivalent to the so-called dynamic pressure and, hence, to flow velocity. So, difference pressure measurement is, nowadays, done by means of a pressure transducer, which converts pressures into voltages and, then, by means of calibration curve, into velocities. A Pitot tube allow to measure, with a high level of accuracy, flow velocity almost aligned with the centre of the total pressure hole; so, if you want to measure other flow velocity components, you need to use a different probe, such as a 5-hole probe or a 7-hole probe. For experimental test purposes, total pressure probes have been arranged into a rake configuration for wake survey purpose; also, a 7-hole probe has been used for the same scope.

## 4.2 Experimental tests on 25° rear end Ahmed body

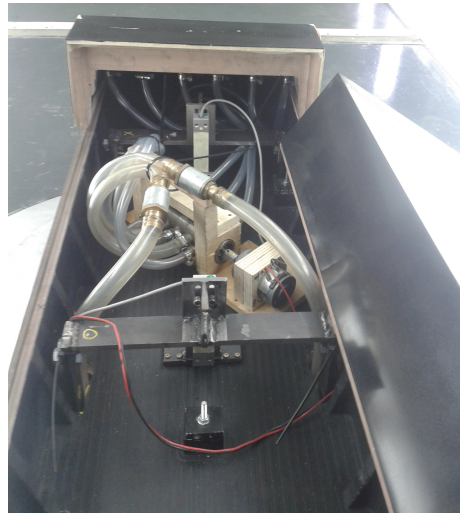
Early experimental activities were aimed to understand flow structure around over the 25° rear end Ahmed body and to estimate performance of both disposed unsteady blowing device and synthetic jet. Before performing tests under different wind tunnel velocity conditions, the unsteady active control device has been analysed by means of hotwire measurements: these measurements are performed to both determine output velocity from the slot and jet frequency as well.

### Tests with unsteady blowing device

Firstly, the unsteady blowing device, in a configuration quite similar to that of Figure 2.9, has been tested. In Figure 4.2a are shown the 25° rear end Ahmed body installed into the wind tunnel test section, equipped with the UB device; also, in Figure 4.2c, hotwire positioning for measurement purposes is shown. To relate output velocity from the slot to the UB supply pressure, which is the pressure at the main compressor tank exit section, the hotwire probe has been located very near to the middle of the slot section, almost aligned with the expected velocity direction, while supply pressure



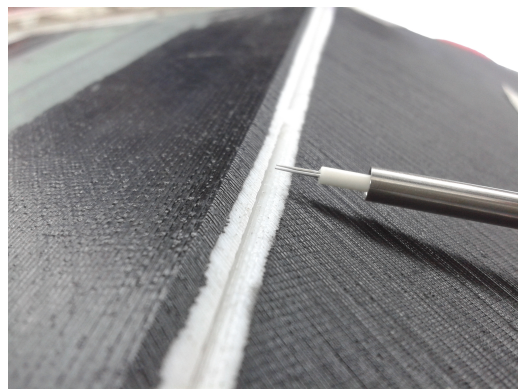
has been controlled with a pressure gauge before the section valve. In fact, using a main compressor tank, it is necessary to activate and deactivate pressure flow through the UB device and it could be performed with the section valve. Also, a pressure regulator maintains the pressure at the desired value for the test (Figure 4.2b). It is worth to notify that such supply pressure is the pressure increment referred to the ambient and not the absolute value of pressure.



(a) Unsteady blowing installation inside Ahmed body



(b) Main tank pressure control unit



(c) Hotwire positioning

**Figure 4.2:** Unsteady Blowing device - Preliminary measurements

As example, in Figure 4.3 are presented data acquired from hotwire measurements, relative to the unsteady blowing device. To identify jet

frequency, time history of velocity in Figure 4.3a has been processed with a Fast Fourier transform (FFT) and jet frequency identification, for a pressure  $P = 0.8 \text{ atm}$  and voltage  $V = 6 \text{ V}$ , is shown in Figure 4.3b. Similarly, data have been acquired for all the range of suitable voltages of the rotating valve electrical motor and also for three values of supply pressure, such as  $P = 0.5 \text{ atm}$ ,  $P = 0.8 \text{ atm}$  and  $P = 1.0 \text{ atm}$ . In this way, a complete characterization of the UB device, in terms of frequency and velocity, has been carried out. Finally, it has been deduced the curve in Figure 4.3c, which allows to relate rotating valve voltage supply to the frequency of the generated jet.

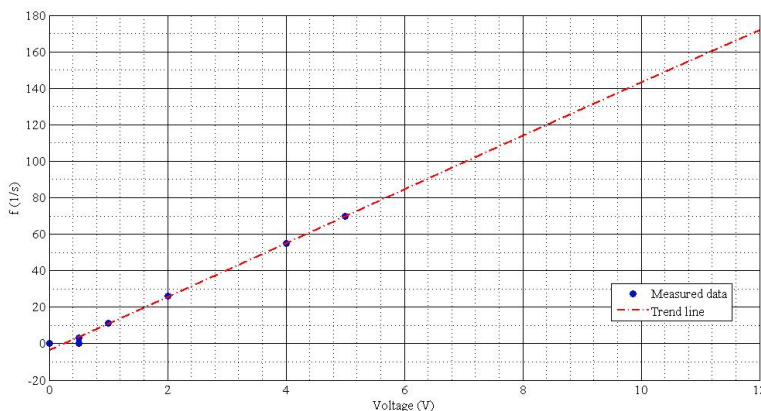
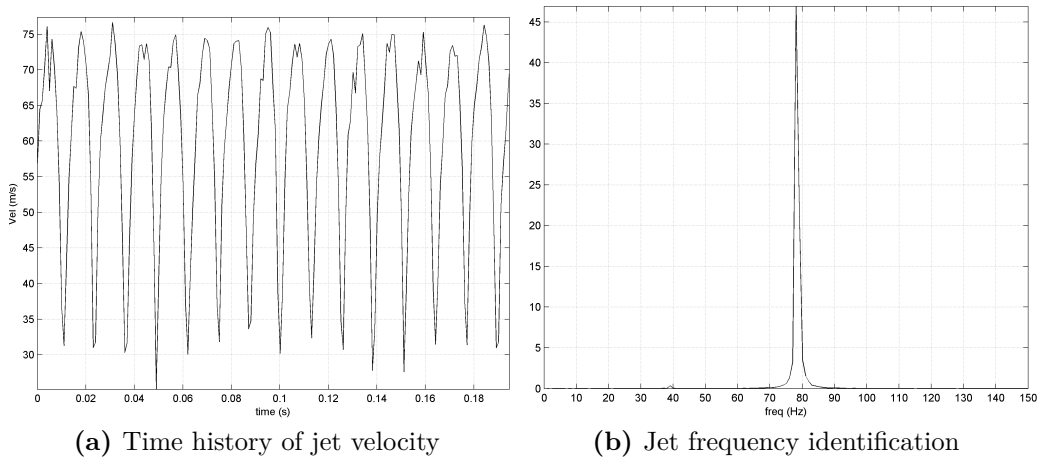
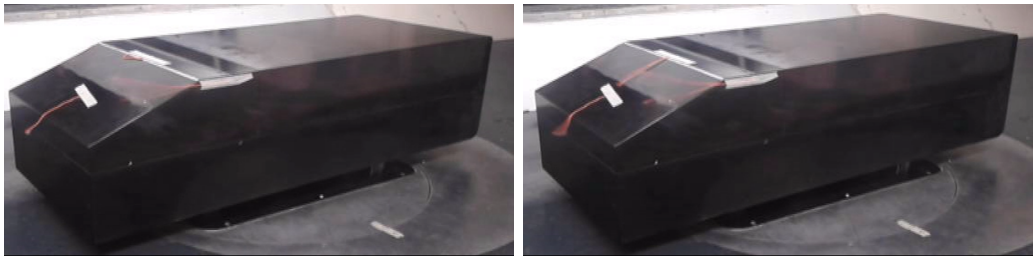


**Figure 4.3:** UB hotwire measurements on 25° rear end Ahmed body

In Figure 4.4 are shown the comparison of tufts behaviour, with and without the unsteady blowing device in operation. From these, it results evident that tufts on tips are almost insensitive to jet deployment, while tufts in the symmetry plane are the most influenced: in particular, looking to the tuft near the slot, in Figure 4.4a it denotes a separation, because it is reversed as compared with the lower one; conversely, in Figure 4.4b, such separation disappears due to the UB jet. The described tufts behaviour has been observed in all the tested configurations of frequency and pressure of the UB and, also, with the use of the SJ device.



(a) Tufts w/o UB control jet

(b) Tufts w/ UB control jet

**Figure 4.4:** Tufts images for the 25° rear end Ahmed body

Informations extracted from tufts have been confirmed by oil film images too. The Figure 4.5 compares oil film pictures, without and with UB control jet: in both figures, there are tip vortices signs, signified by the oil lines starting from the corner of the slanted surface. Also, the Figure 4.5b underlines how the UB flow drags oil, defining more clear transversal lines than before. The absence of transversal lines in Figure 4.5a it is an evidence of separation over this part of the Ahmed body.

As anticipated in Figure 2.4, two different load cells configurations have been used. Three-cells configurations measurements, due to weak load cell fixing, have shown a low level of reliability and, very frequently, zero-drifting. Hence, a more rigid two-cells configurations has been realized for overcoming such issues. The most relevant data acquired during the tests on 25° rear end Ahmed body, equipped with unsteady blowing jet, are listed in Table 4.1 and, graphically, presented in Figure 4.6. The Figure 4.6a, Figure 4.6b, Figure 4.6c, contain time histories of the unsteady blowing jet: their first part

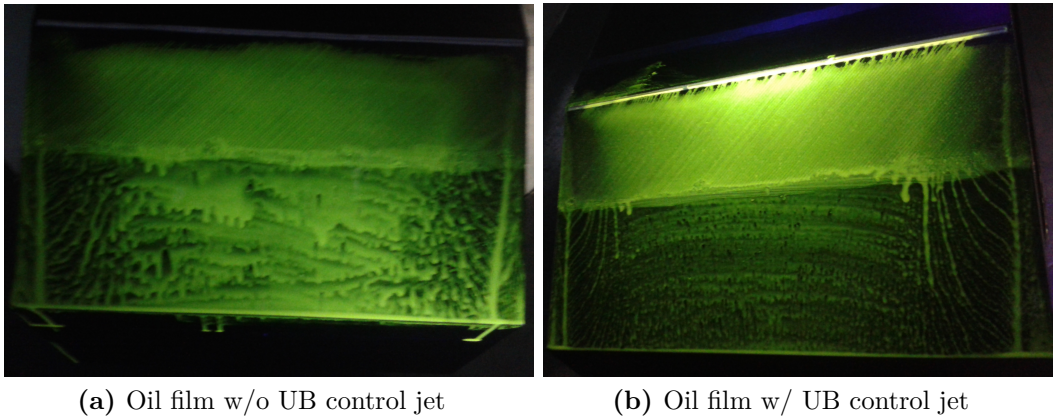
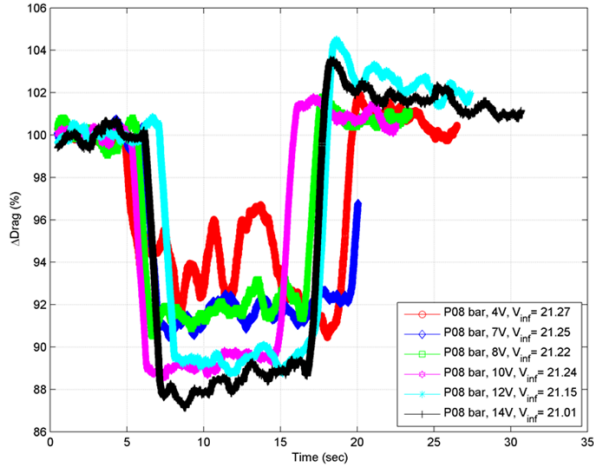


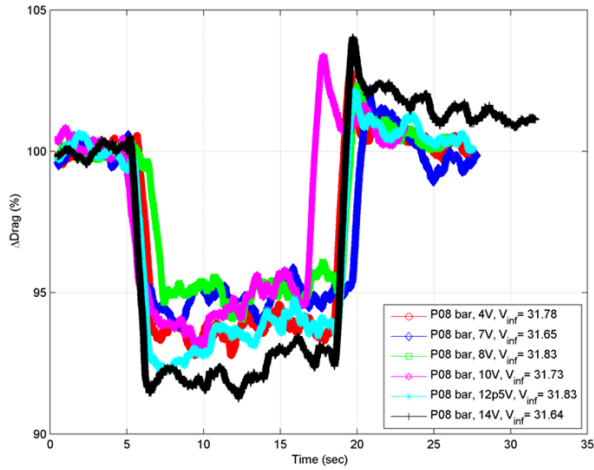
**Figure 4.5:** Oil film images for the 25° rear end Ahmed body

represent the Ahmed body drag without any unsteady control device; then, when time is about 5 s, the UB jet is activated for about 15 s and, so, it influences drag; lastly, the UB device is stopped and Ahmed body drag come back almost at its initial value. In this way, it is immediate to recognize the effect of UB device on the 25° rear end Ahmed body drag. So, drag reduction ( $\Delta\text{Drag}$ ) has been evaluated by the ratio of drag values relative to without and with jet deployment. From these resulted that, in almost all UB configurations tested, the operation of such active control device reduces Ahmed body drag and such reduction ranges between 5% to 12%, depending on supply pressure and frequency.

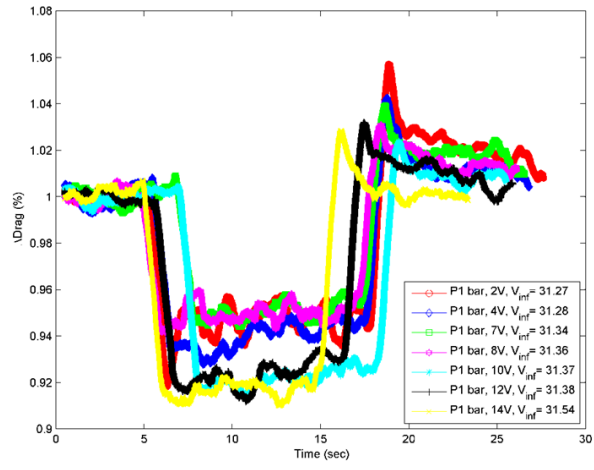
Considering oil films, PIV and tufts observations, it is not wrong to impute drag reduction to the control of separation over the Ahmed body slanted surface.



(a)  $V_{inf} = 20 \text{ m/s}$ ,  $P = 0.8 \text{ atm}$



(b)  $V_{inf} = 30 \text{ m/s}$ ,  $P = 0.8 \text{ atm}$



(c)  $V_{inf} = 30 \text{ m/s}$ ,  $P = 1.0 \text{ atm}$

Figure 4.6: UB load cells measurements -  $25^\circ$  rear end Ahmed body

$V_{\text{inf}}$ [m/s]	P [atm]	Voltage [V]	f [Hz]	Drag w/o jet [N]	Drag w/ jet [N]	$\Delta$ Drag
21.27	0.8	4	50	11.04	10.34	-6.32%
21.25	0.8	7	95	11	10.07	-8.44%
21.23	0.8	8	110	10.91	10.02	-8.14%
21.24	0.8	10	140	10.91	9.742	-10.73%
21.15	0.8	12	170	10.54	9.423	-10.61%
21.01	0.8	14	200	10.47	9.259	-11.54%
31.78	0.8	4	50	23.59	22.11	-6.27%
31.65	0.8	7	95	23.44	22.21	-5.25%
31.83	0.8	8	110	23.65	22.47	-5.02%
31.73	0.8	10	140	23.53	22.17	-5.77%
31.83	0.8	12.5	177.5	23.65	22.13	-6.44%
31.64	0.8	14	200	22.9	21.12	-7.78%
31.27	1.0	2	20	22.54	21.35	-5.26%
31.28	1.0	4	50	22.78	21.42	-5.97%
31.34	1.0	7	95	22.74	21.61	-4.97%
31.36	1.0	8	110	22.63	21.5	-5.00%
31.37	1.0	10	140	22.92	21.15	-7.76%
31.38	1.0	12	170	22.97	21.22	-7.61%

**Table 4.1:** UB load cells measurements - 25° rear end Ahmed body

Finally, using a rake of total pressure probes, the flow field of horizontal component of velocity ( $u$ ) has been reconstructed. The pressure probes rake has been located about 1.00 m behind the Ahmed body end. With the pressure probes rake, a gross area of 0.30 m of height and 0.45 m of width has been investigated, with a limitation on the allowable lower height (the area starts about 0.05 m from the floor). This issue causes the lack of data relative to the Ahmed under-body flow, because of its minimum clearance of just 0.05 m from the floor. Anyway, even if the data are not complete and, so, not sufficient to perform a correct estimation of drag from pressure measurements, using wake survey methods, it is even useful as further verification of what it has been observed with tufts and oil film. Furthermore, because of the flat under-body of Ahmed body and its horizontal installation (the so-called body pitch angle, referred to the

horizontal, is null), the under-body flow has little influence on the flow over the upper Ahmed body surface. In Figure 4.7, the  $u$  velocity fields are shown. As seen previously, the vortices are present in both situations; but, from these, it is noticed that velocity into the core of the vortices is higher for the case with the UB control jet (Figure 4.7b) than the case without UB control jet (Figure 4.7). So, if both tests have been made at the same value of  $V_{inf}$ , higher velocity behind the body results in less drag, because of the lower momentum loss, as observed with load cells measurements.

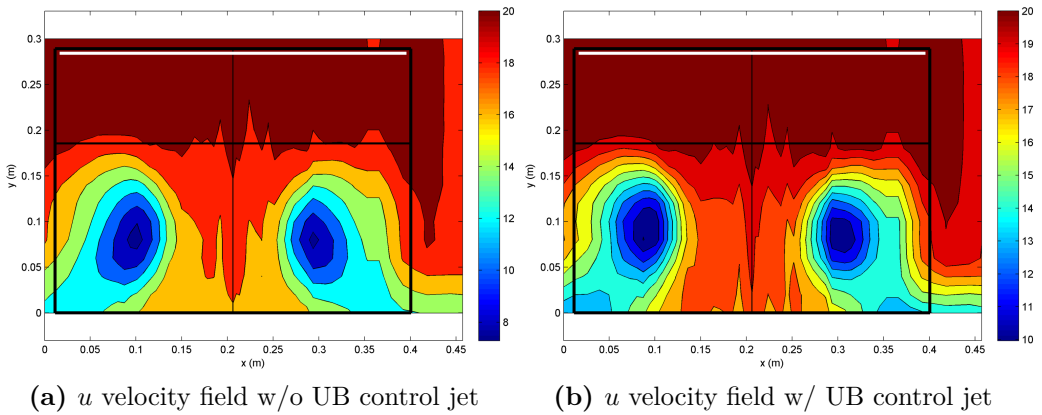


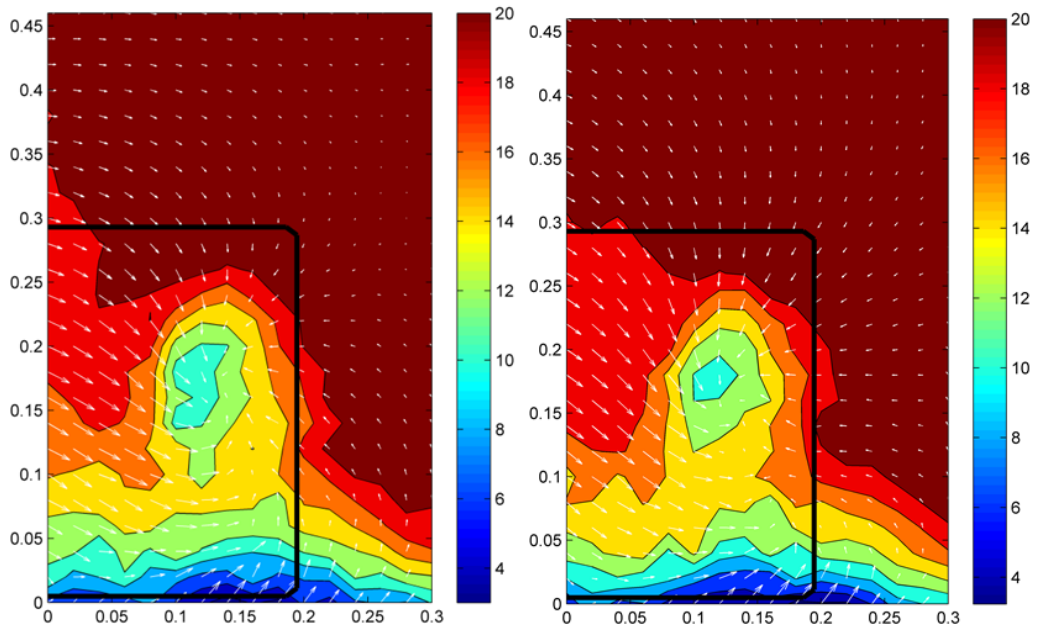
**Figure 4.7:**  $u$  velocity fields for the  $25^\circ$  rear end Ahmed body

### Tests with synthetic jet device

Secondly, the  $25^\circ$  rear end Ahmed body has been equipped with the synthetic jet device in Figure 2.12. As a first attempt, the SJ device has been put inside the volume of the Ahmed body; but, due to heating, it was necessary to locate the SJ elsewhere outside. Hence, a series of tubing, which dimensions are in Table 2.3, have been disposed to connect the output of the mechanical cylinder to the input of the blowing chamber. These tubes have been selected without any consideration about their possible influence on SJ resonant characteristics; but, how to optimize the system in order to work near the resonance has been left as the ultimate step, after the identification of an effective SJ operating condition for drag reduction purposes. All of the three blowing plates described in § 2.3.2 have been

evaluated under different SJ RPMs and wind tunnel velocities  $V_{\text{inf}}$ . For each blowing plate, hotwire measurements along with load cells ones have been performed, because of the different channel shapes of each blowing plate.

Phenomenologically, it has been noticed that no big changes occur using the SJ device or using the UB device. Thus, in Figure 4.8 are shown the velocity components measured with a 7-hole probe. Comparing these with the Figure 4.7, it results that no evident differences arose. Data in Figure 4.8b have been obtained with mechanical SJ device at 2500 RPM. The importance of such measurements is that, using a 7-hole, it is possible to gather other velocity components and not only the  $u$  one: knowing all the velocity components could be useful to set-up a wake survey method and, so, to measure induced drag amount and lift of Ahmed body. In fact, lift can be measured only by an indirect way because of load cells arrangement.



(a) Velocity components w/o SJ control jet (b) Velocity components w/ SJ control jet

**Figure 4.8:** Velocity components for the 25° rear end Ahmed body

The Figure 4.9 shows results of hotwire measurements on #1 blowing plate. The #1 blowing plate has a curved channel in order to generate a jet with about 20° from the slanted surface. So, hotwire probes has been located



nearly similar to that in Figure 4.2c. In Figure 4.9a is reported the velocity time history acquired by the hotwire anemometer: the absolute value of velocity, over the time, is representative of a SJ behaviour. It shows a principal peak, related to the blowing phase of the SJ, and a secondary peak, relative to the suction phase. As expected, the second peak is lower than the principal peak, probably for the higher flow resistance to be sucked inside the blowing chamber. Time history of velocity has been analysed by means of a Fast Fourier transform (FFT) to identify jet frequency and to relate this to mechanical SJ parameter, that is SJ RPM. The curve in Figure 4.9c shows the relationship between mechanical RPM and  $V_{jet}$  from the slot, highlighting also the impossibility of selecting jet frequency without changing jet velocity. From this curve, it can be seen that a resonance occurs at 2500 RPM, where there are the maximum of both  $V_{jet_{max}}$  and  $V_{jet_{mean}}$ .

Load cells measurements, for  $V_{inf} = 20$  m/s, in the SJ #1 configurations are in Figure 4.10; data of all conditions tested are listed in Table 4.2. The Figure 4.10 displays the effects of both frequency and velocity in reducing drag: the maximum value of drag reduction happens when SJ is at 2500 RPM, namely  $f = 88$  Hz,  $V_{jet_{max}} = 63.500$  m/s and  $V_{jet_{mean}} = 19.76$  m/s. In this condition, the drag reduction ( $\Delta Drag$ ) has been evaluated similarly to that of the UB device and it is about 11.35%. As expected, the value of 2500 RPM causes both SJ resonance and maximum drag reduction. When  $V_{inf}$  increases, the SJ #1 effectiveness reduces, as reported in Table 4.2. This effect is mainly due to the lowering of non-dimensional parameters, such as the  $C_\mu$ ; but, almost in all the  $V_{inf}$  tested, drag reduction, is more or less, between 10%.

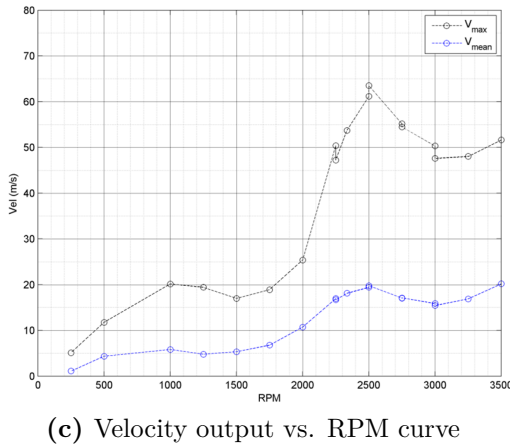
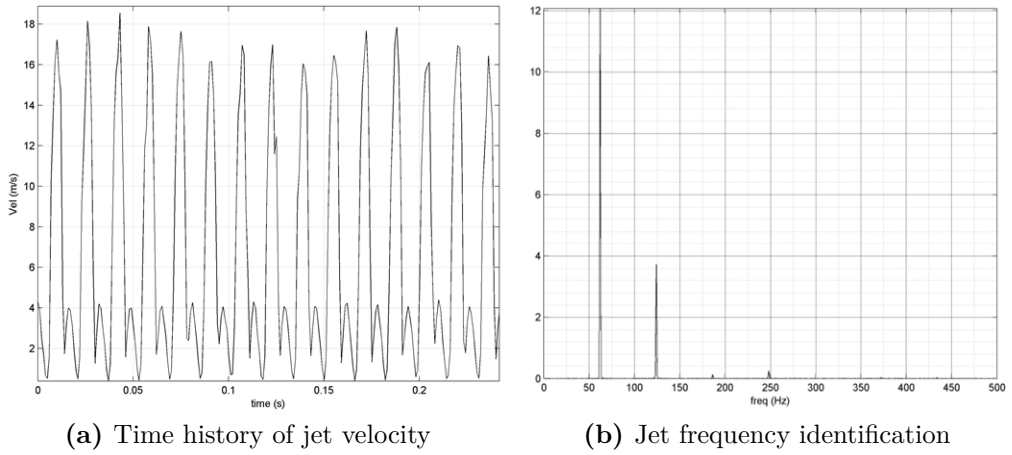


Figure 4.9: Hotwire measurements - SJ #1 configuration

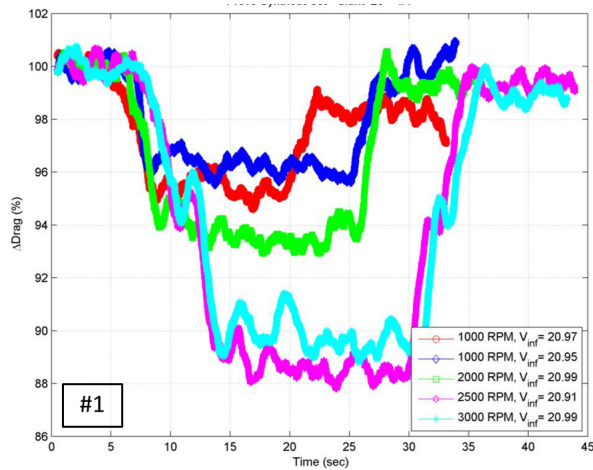


Figure 4.10: Load cells measurements - SJ #1 configuration

$V_{inf}$ [m/s]	$V_{jetmax}$ [m/s]	$V_{jetmean}$ [m/s]	RPM	f [Hz]	$\Delta Drag$
20	20.15	5.81	1000	36	-3.93%
20	-	-	1000	-	-4.55%
20	-	-	1000	-	-3.75%
20	-	-	1000	-	-1.74%
20	25.38	10.73	2000	66	-6.29%
20	-	-	2000	-	-6.24%
20	63.50	19.76	2500	88	-11.35%
20	50.31	15.88	3000	103	-8.54%
20	-	-	3000	-	-10.17%
25	20.15	5.81	1000	36	-1.74%
25	25.38	10.73	2000	66	-4.73%
25	63.50	19.76	2500	88	-10.65%
25	-	-	2500	-	-10.67%
25	50.31	15.88	3000	103	-9.08%
30	20.15	5.81	1000	36	2.46%
30	-	-	1000	-	1.60%
30	17	5.32	1500	53	-4.29%
30	-	-	1500	-	-3.84%
30	25.38	10.73	2000	66	-2.57%
30	-	-	2000	-	-3.84%
30	63.50	19.76	2500	88	-9.75%
30	50.31	15.88	3000	103	-6.44%
30	-	-	3000	-	-8.66%

**Table 4.2:** Load cells measurements - SJ #1 configuration

Changing the blowing plate from #1 configuration to #2 configuration, which has the blowing channel perpendicular to the slanted surface ( $\phi = 90^\circ$ ), test results show a lowering of drag reduction, even if jet velocities and frequency are almost unchanged. The Figure 4.11 displays that the SJ resonant condition still occurs at 2500 RPM, with velocity values slightly higher than those in Figure 4.11: in particular, the value of  $V_{jet_{mean}}$  is little larger, probably due to the less flow resistance of a straight channel compared with a curved one. All load cells measurements for the Ahmed body equipped with the #2 configuration of SJ blowing plate, at different  $V_{inf}$  velocities, are listed in Table 4.3. The Figure 4.12 represents data at which the higher value of drag reduction has been measured: it occurs when  $V_{inf} = 30$  m/s and SJ operating condition is at 2500 RPM ( $f = 88$  Hz,  $V_{jet_{max}} = 63.01$  m/s,  $V_{jet_{mean}} = 32.46$  m/s). In these conditions, drag reduction is not higher than 4%, more than halved compared to #1 configuration. Also, the Figure 4.12 underlines the detrimental effect of  $V_{inf}$  in reducing  $C_\mu$  value, when, at  $V_{inf} = 30$  m/s and 1000 RPM, drag increases instead of reducing.

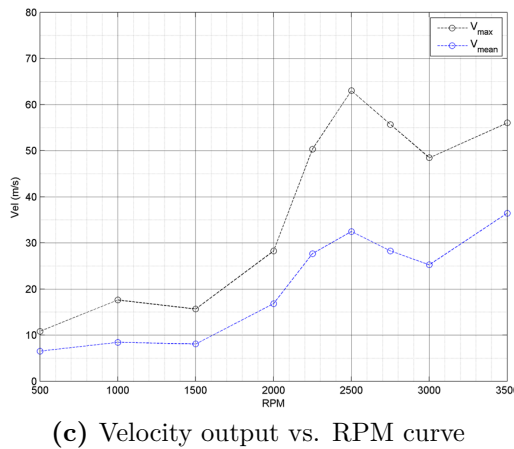
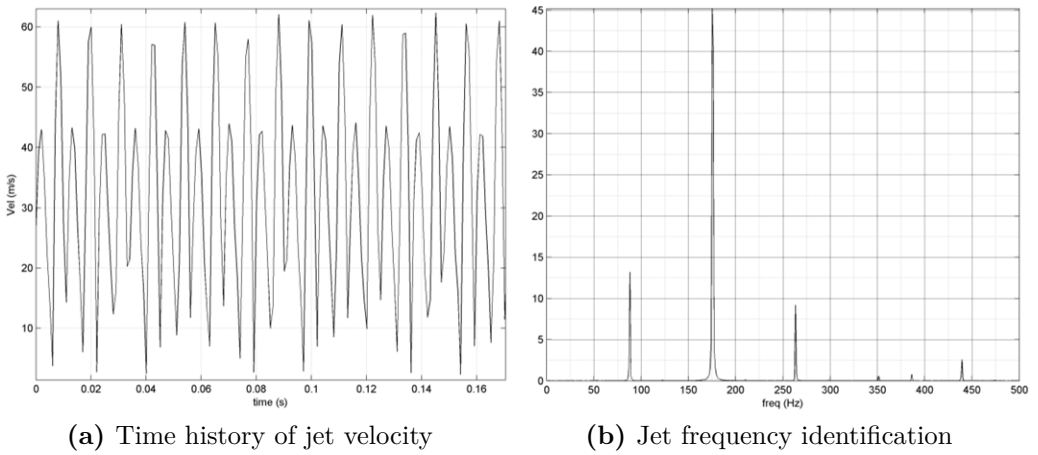


Figure 4.11: Hotwire measurements - SJ #2 configuration

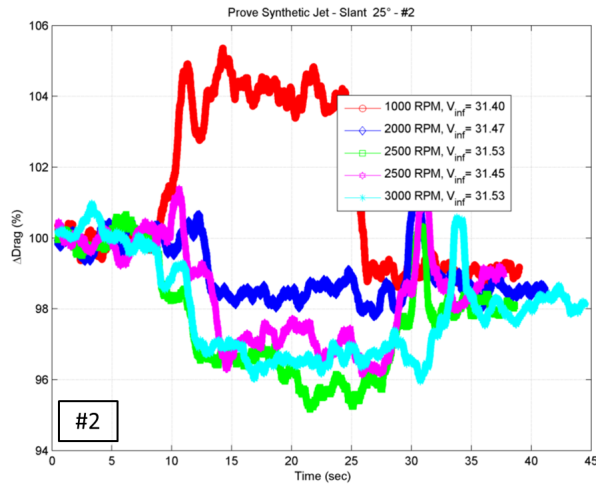
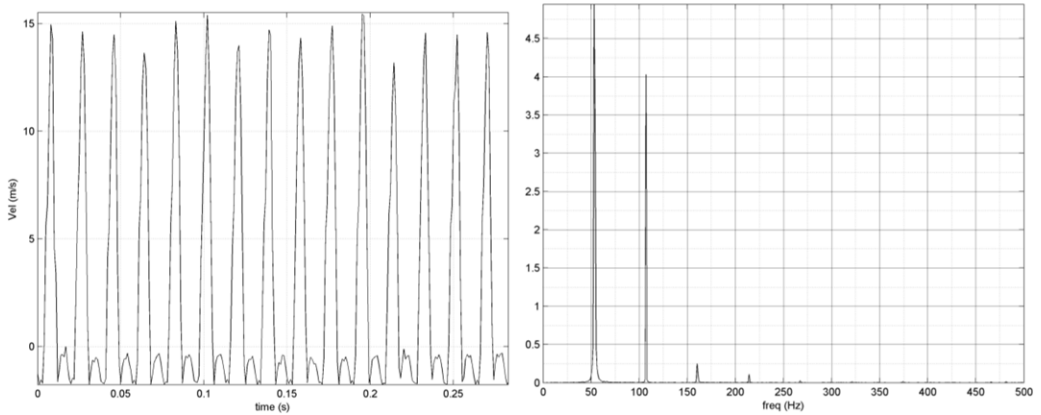


Figure 4.12: Load cells measurements - SJ #2 configuration

$V_{inf}$ [m/s]	$V_{jet_{max}}$ [m/s]	$V_{jet_{mean}}$ [m/s]	RPM	f [Hz]	$\Delta Drag$
15	17.63	8.43	1000	37	-2.48%
15	—	—	1000	—	-1.32%
15	28.24	16.81	2000	54	-2.62%
15	—	—	2000	—	-1.62%
15	63.01	32.46	2500	88	-1.56%
15	—	—	2500	—	-0.31%
15	48.46	25.25	3000	103	-1.82%
15	—	—	3000	—	-1.73%
20	17.63	8.43	1000	37	-1.96%
20	—	—	1000	—	-1.44%
20	28.24	16.81	2000	54	-1.74%
20	—	—	2000	—	-0.95%
20	63.01	32.46	2500	88	-2.04%
20	—	—	2500	—	-1.29%
20	48.46	25.25	3000	103	-2.37%
20	—	—	3000	—	-1.81%
25	17.63	8.43	1000	37	0.61%
25	—	—	1000	—	0.94%
25	28.24	16.81	2000	54	-1.13%
25	—	—	2000	—	-0.71%
25	63.01	32.46	2500	88	-2.75%
25	—	—	2500	—	-1.57%
25	48.46	25.25	3000	103	-2.80%
25	—	—	3000	—	-1.63%
30	17.63	8.43	1000	37	4.10%
30	—	—	1000	—	2.34%
30	28.24	16.81	2000	54	-1.60%
30	—	—	2000	—	-0.90%
30	63.01	32.46	2500	88	-3.83%
30	—	—	2500	—	-3.02%
30	—	—	2500	—	-2.81%
30	48.46	25.25	3000	103	-3.32%
30	—	—	3000	—	-1.91%

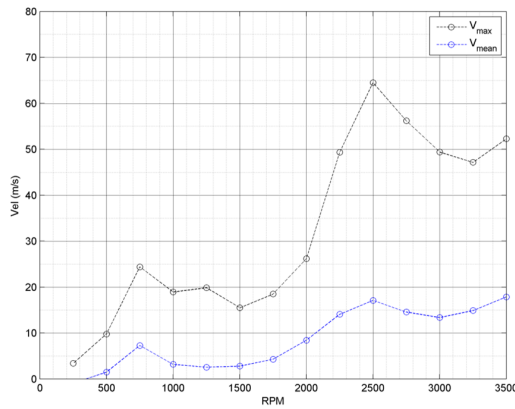
**Table 4.3:** Load cells measurements - SJ #2 configuration

Lastly, #3 blowing plate has been tested. The #3 plate is identical to the #2 configuration in terms of  $\phi$  angle, but it differs from the #2 ones for the absence of separation walls, between the blowing chamber and inside the slot. A similar investigation was made in [33], discovering the beneficial effects of such walls in increasing the exhaust velocity from the slot. Hotwire measurements in Figure 4.13 confirm this statement, with a more evident effect on  $V_{jet_{mean}}$  values, as compared with the #2 blowing plate. However,  $V_{jet_{mean}}$  values of the #3 plate are not so different from those of #1 configuration (Figure 4.9). Despite this, load cells data in Table 4.4 depict the complete ineffectiveness of such plate in reducing drag, for each value of velocity  $V_{inf}$  tested. As an example, in Figure 4.14, the results for  $V_{inf} = 25$  m/s are reported. Summarizing, the #3 blowing plate is ineffective and causes drag increase of about 3%, in all the tested conditions.



(a) Time history of jet velocity

(b) Jet frequency identification



(c) Velocity output vs. RPM curve

Figure 4.13: Hotwire measurements - SJ #3 configuration

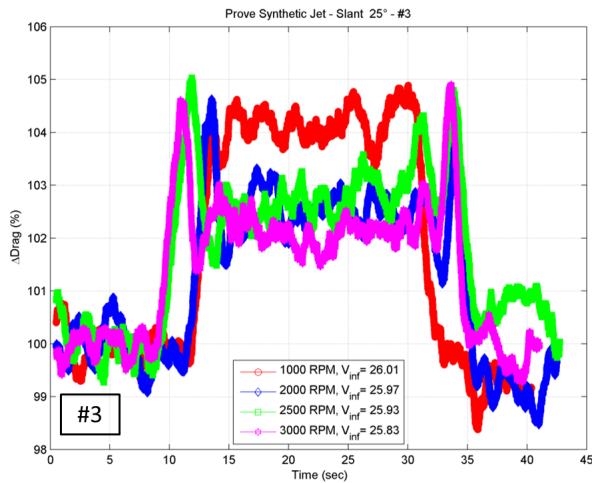


Figure 4.14: Load cells measurements - SJ #3 configuration



$V_{inf}$ [m/s]	$V_{jet_{max}}$ [m/s]	$V_{jet_{mean}}$ [m/s]	RPM	f [Hz]	$\Delta Drag$
15	18.93	3.17	1000	36	3.53%
15	—	—	1000	—	3.03%
15	26.18	8.45	2000	71	3.17%
15	—	—	2000	—	2.47%
15	64.51	17.09	2500	88	4.85%
15	—	—	2500	—	4.12%
15	49.39	13.36	3000	103	3.46%
15	—	—	3000	—	2.65%
20	18.93	3.17	1000	36	2.17%
20	—	—	1000	—	2.19%
20	26.18	8.45	2000	71	2.80%
20	—	—	2000	—	2.77%
20	64.51	17.09	2500	88	3.36%
20	—	—	2500	—	2.60%
20	49.39	13.36	3000	103	1.68%
20	—	—	3000	—	1.44%
25	18.93	3.17	1000	36	4.15%
25	—	—	1000	—	3.48%
25	26.18	8.45	2000	71	2.53%
25	—	—	2000	—	2.68%
25	64.51	17.09	2500	88	2.83%
25	—	—	2500	—	2.65%
25	49.39	13.36	3000	103	2.26%
25	—	—	3000	—	2.16%
30	18.93	3.17	1000	36	4.63%
30	—	—	1000	—	4.88%
30	26.18	8.45	2000	71	2.64%
30	—	—	2000	—	2.87%
30	64.51	17.09	2500	88	1.87%
30	—	—	2500	—	2.43%
30	49.39	13.36	3000	103	2.45%
30	—	—	3000	—	1.63%

Table 4.4: Load cells measurements - SJ #3 configuration

## 4.3 Experimental tests on 35° rear end Ahmed body

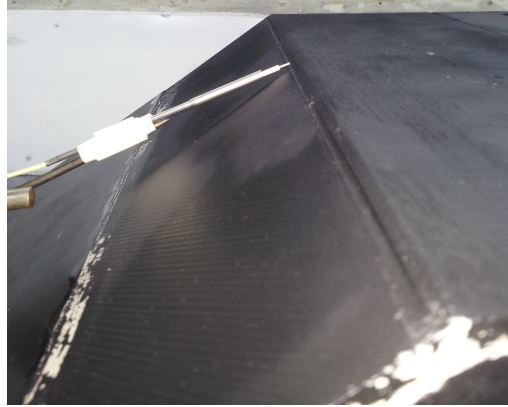
Similarly, experimental analyses have been performed on the 35° rear end Ahmed body, in Figure 2.5. These were aimed to investigate flow structure over such model and to verify if active control devices, of any type, can be used to reduce drag. Due to different characteristics of #4 and #5 blowing chambers compared with the #1, #2 and #3 ones, frequencies and velocities of active control devices have been measured by means of pressure and hotwire measurements.

### Tests with unsteady blowing device

First experimental tests on 35° rear end Ahmed body have regarded the model equipped with the unsteady blowing device. The unique differences between this configuration and that tested for the 25° rear end Ahmed body are the volume of the blowing chamber and the blowing plates (more details are in § 2.3.1). The unsteady blowing system arrangement for the 35° rear end Ahmed body is the same of that in Figure 4.2a and hotwire probe set-up is shown in Figure 4.15a: the hotwire probe has been located very near to the middle of the slot section, almost aligned with the expected velocity direction. As previous tests, pressure flow through the UB device has been controlled by a section valve, required to activate and deactivate the device, and a pressure regulator maintains the pressure at the desired value.

Data relative to the unsteady blowing device, measured with the hotwire probe, are presented in Figure 4.15. Jet frequency identification, from time history of velocity in Figure 4.15b, has been performed using Fast Fourier transform (FFT): in Figure 4.15c is shown the case with  $P = 0.5$  atm and voltage  $V = 5$  V. Since rotating valve has been not changed, the relationship between jet frequency and rotating valve voltage supply is the same of that in Figure 4.3c.

Looking to the tufts in Figure 4.16, it is evident the different behaviour of such wool pieces as compared with those of Figure 4.16. A first consideration



(a) Hotwire positioning

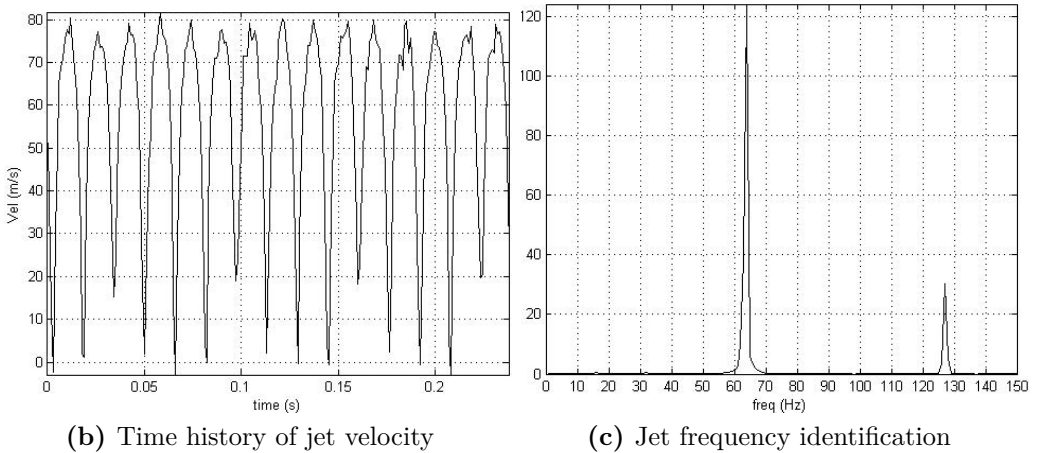


**Figure 4.15:** UB hotwire measurements on 35° rear end Ahmed body

can be deduced from Figure 4.16a: differently from the case of 25° rear end Ahmed body, when active control jet is inactive, there are no tip vortices; also, the flow is largely separated over the slanted surface; when active control device is active, tip vortices appears and flow reattaches over the slanted surface, as well. This behaviour has been observed in all the tested active control device configurations, without any effects related to frequency or pressure of the UB or to the use of the SJ device. This particular behaviour has been confirmed by other investigations made with oil film, rake of pressure probes, PIV and 7-hole probe, measurements.

Oil film images in Figure 4.17 show the different flow field over the slanted surface, without and with the use of UB control jet: the Figure 4.17a

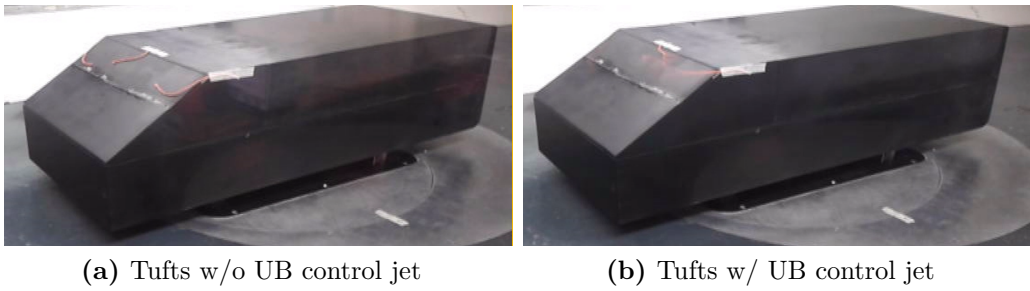
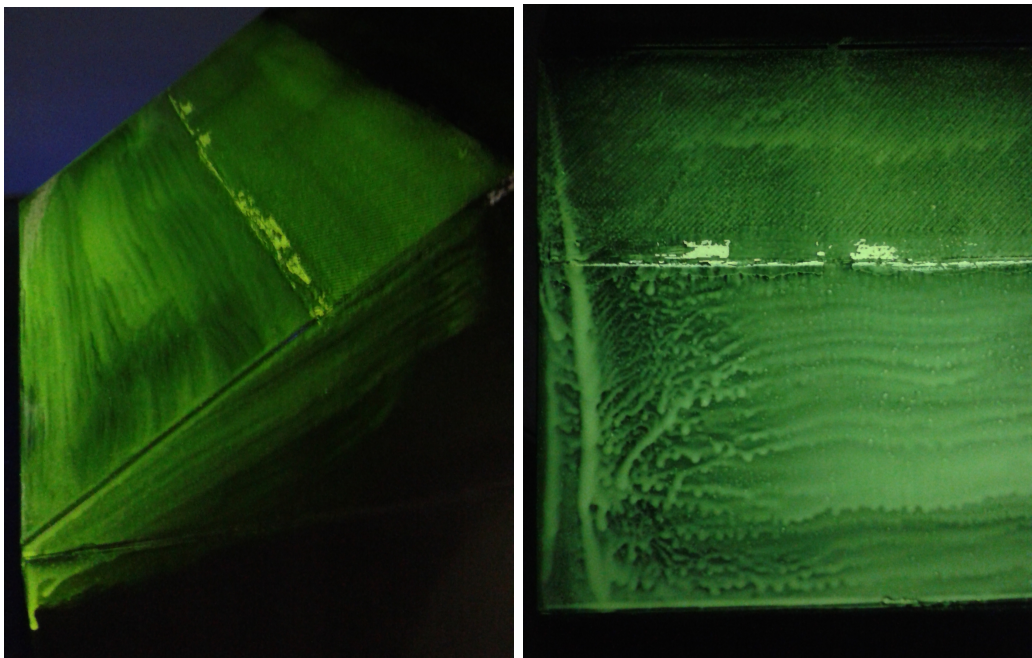


**Figure 4.16:** Tufts images for the 35° rear end Ahmed body

underlines the extent of separation over the slanted surface, where no transversal lines, due to the dragging of fluid near the surface, are present; conversely, in Figure 4.17b, it can be seen clearly the presence of vortex lines, similar to those seen in Figure 4.5b, and transversal lines too. The transversal lines in Figure 4.17b signify that, after the UB activation, the flow attaches on that surface.



(a) Oil film w/o UB control jet

(b) Oil film w/ UB control jet

**Figure 4.17:** Oil film images for the 25° rear end Ahmed body

The ability of UB to cause flow reattachment in the symmetry plane of the  $35^\circ$  rear end Ahmed body has been also observed performing PIV investigations on its symmetry plane. The processed images are presented in Figure 4.18, showing the capability of such active control device to reduce separated zone behind the  $35^\circ$  rear end Ahmed body.

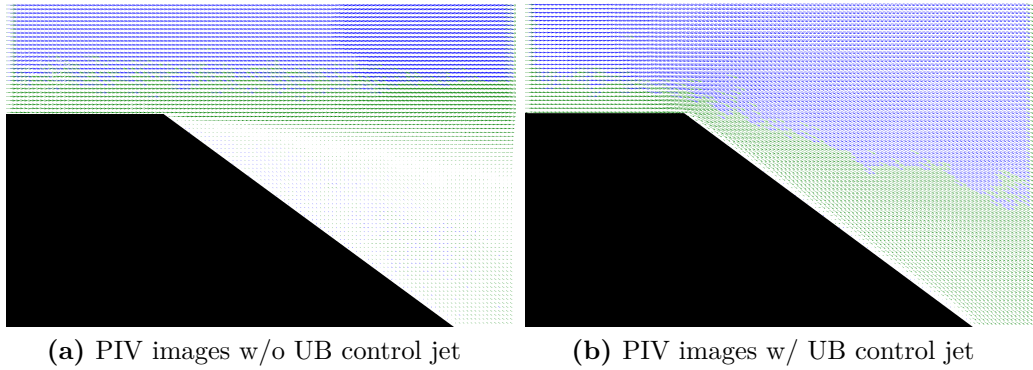


**Figure 4.18:** PIV images for the  $35^\circ$  rear end Ahmed body on symmetry plane

As a further confirm of the different flow field between the cases of with and without UB control jet, by means of a rake of pressure probes, the flow field in the wake of the  $35^\circ$  rear end Ahmed body has been measured. The comparison of the two acquired flow fields is displayed in Figure 4.19. As before, with a rake of total pressure probes has been acquired the flow field of horizontal component of velocity ( $u$ ); the measurement plane is located about 1.00 m behind the Ahmed body end and the measured gross area is of 0.30 m of height and 0.45 m of width. A limitation on the minimum allowable height from the floor (the area starts about 0.05 m from the floor) it's still present, causing the lack of data relative to the Ahmed under-body flow. From the pictures in Figure 4.19 is evident, as discussed before, the presence and growth of tip vortices when UB device is in operation.

Load cells measurements in Figure 4.20 show the time history of drag force, during UB jet deployment. These pictures underline that, even if reattachment occurs over the slanted surface, drag increases due to the UB activation. Drag increment is almost independent of frequency and

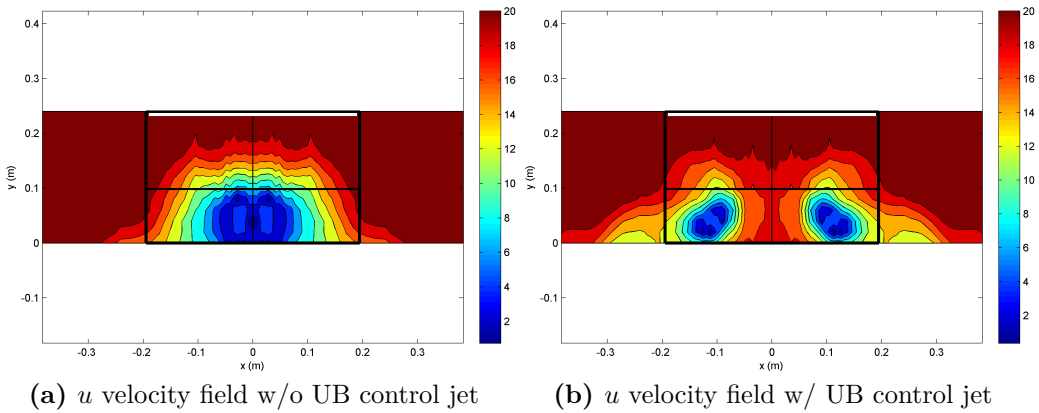
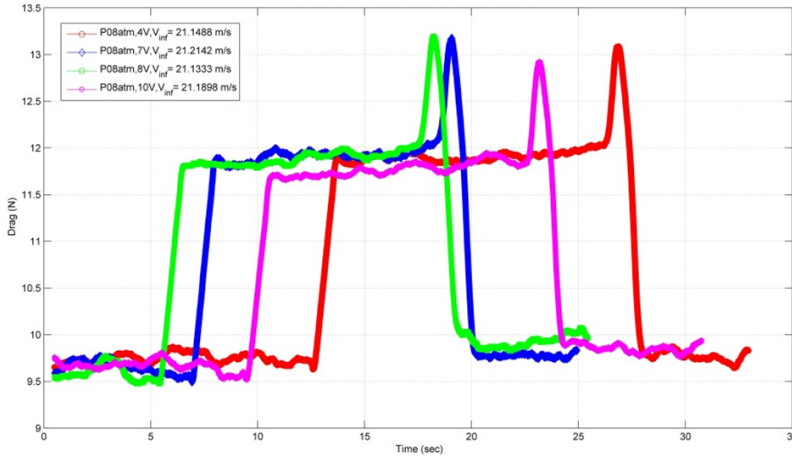


**Figure 4.19:**  $u$  velocity fields for the 35° rear end Ahmed body

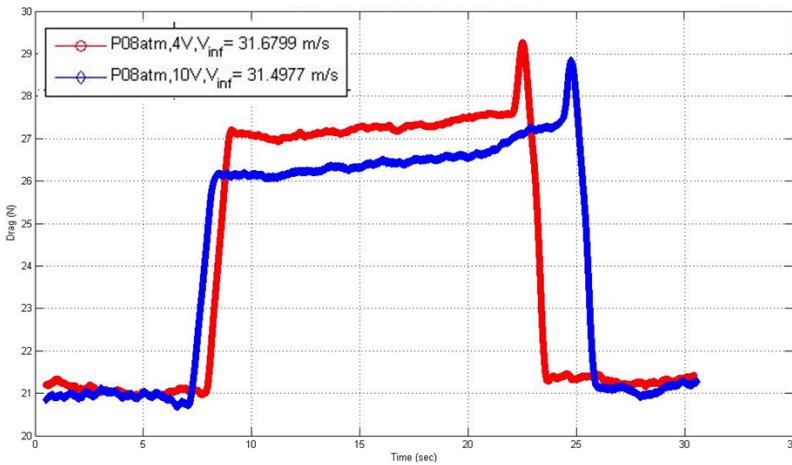
$V_{inf}$ , as can be seen in Figure 4.20a and in Figure 4.20b. Thus, considering the flow reattachment over the slanted surface, a possible explanation of this behaviour could be the corresponding increment of the induced drag component. As can be seen in Table 4.5, the UB device causes an average drag increment of about 25% in all tested configurations and no evidence of any drag reduction has been observed. These data have been measured using the two-load cells configuration and are very similar to those acquired with the three-load cells configuration.

$V_{inf}$ [m/s]	P [atm]	Voltage [V]	f [Hz]	Drag w/o jet [N]	Drag w/ jet [N]	$\Delta$ Drag
21.15	0.8	4	50	9.7	11.85	22.20%
21.21	0.8	7	95	9.6	11.9	23.90%
21.13	0.8	8	110	9.5	11.8	24.20%
21.19	0.8	10	140	9.6	11.8	22.90%
31.68	0.8	4	50	21	27.5	30.90%
31.50	0.8	10	140	21	26.8	27.60%

**Table 4.5:** UB load cells measurements - 35° rear end Ahmed body



(a)  $V_{inf} = 20$  m/s,  $P = 0.8$  atm



(b)  $V_{inf} = 30$  m/s,  $P = 0.8$  atm

**Figure 4.20:** UB load cells measurements -  $35^\circ$  rear end Ahmed body

### Tests with synthetic jet device

After the tests on  $35^\circ$  rear end Ahmed body equipped with the UB device, through which it resulted that the use of an UB active control device increases its drag, some experiments have been made using the mechanical SJ device used for the  $25^\circ$  rear end Ahmed body. The connection tubes, used to connect the output of the mechanical cylinder to the input of the blowing chamber, are the same listed in Table 2.3. Both of the blowing plates described in § 2.3.2 have been evaluated under different SJ RPM and wind tunnel velocity  $V_{inf}$ . Remembering that the only difference between

the #4 blowing plate and the #5 one is the different value of  $\phi$  angle, there is no reason to perform hotwire measurements on both these blowing plates. Hence, it has been assumed that the value of output velocity from the slot, along with jet frequency, are not influenced by the change of  $\phi$  angle and data measured for the #4 blowing plate have been used as reference for the #5 blowing plate too.

To investigate if different phenomena occur in the wake, due to the use of a SJ active control device, the velocity components have been measured by means of a 7-hole probe: it has been located just ahead of the wake plane acquired with the pressure probes rake, about 0.50 m behind the Ahmed body rear end. From velocity maps in Figure 4.21, it can be observed that no big changes occur, on such body, using the SJ device as compared with using the UB device. As observed previously, comparing the Figure 4.21a with the Figure 4.21a, the development of tip vortices is evident. Also, the jet generated by the SJ device causes the flow to be more rotational than before, as signified by in-plane velocity vectors. The observation of this flow behaviour is in accordance to the hypothesis of the increase of induced drag due to the use active control device; but, the lack of load cells able to measure lift of such body and, thus, induced drag, allows to estimate such drag contribute only indirectly from data acquired by the 7-hole probe.

The #4 and #5 blowing plates have a bit larger volume than the blowing plates used for the 25° rear end Ahmed body. So, hotwire measurements have been performed to characterize SJ output in such different configuration. The Figure 4.22 shows results of hotwire measurements on #4 blowing plate; these results have been used as a reference for the #5 blowing plate as well. The #4 blowing plate has a curved channel in order to generate a jet with about 20° from the slanted surface, while the #5 has also a curved channel but with a  $\phi$  angle of 30° from the slanted surface, to produce a jet with the same inclination used for the 25° rear end Ahmed body. Hotwire probe positioning has been almost the same shown in Figure 4.15a. In Figure 4.22a is reported the velocity time history acquired by the hotwire anemometer: the absolute value of velocity, over the time, is representative of a SJ behaviour. A principal peak, related to the blowing phase of the SJ,



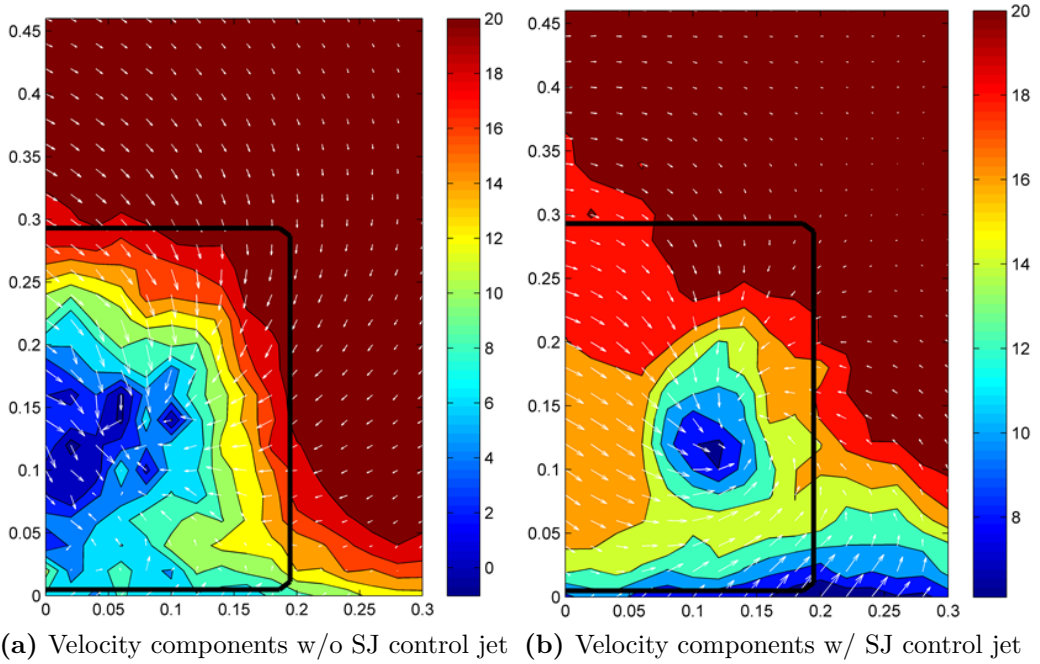


**Figure 4.21:** Velocity components for the 35° rear end Ahmed body

and a secondary peak, relative to the suction phase, can be still observed; the second peak is lower than the principal peak, probably for the higher flow resistance to be sucked inside the blowing chamber. Time history of velocity has been analysed by means of a Fast Fourier transform (FFT) to identify jet frequency and to relate this to the RPM of the SJ device. The curve in Figure 4.22c shows the relationship between mechanical RPM and  $V_{jet}$  from the slot, highlighting also the impossibility of selecting jet frequency without changing jet velocity. From this curve, it can be seen that the maximum value of the maximum velocity ( $V_{jet_{max}}$ ), that is the resonance, occurs between the 2500 RPM and 2750 RPM.

Load cells measurements have been executed at different  $V_{inf}$  velocities, from  $V_{inf} = 15$  m/s to  $V_{inf} = 30$  m/s, and RPMs of the mechanical SJ device. Results relative to the #4 configuration are in Figure 4.23 and, numerically, listed in Table 4.6. From the Figure 4.23 it's evident that the use of SJ device causes a drag increase instead of a reduction: the drag value increase abruptly when the SJ starts to work; then, its value stabilizes around a lower

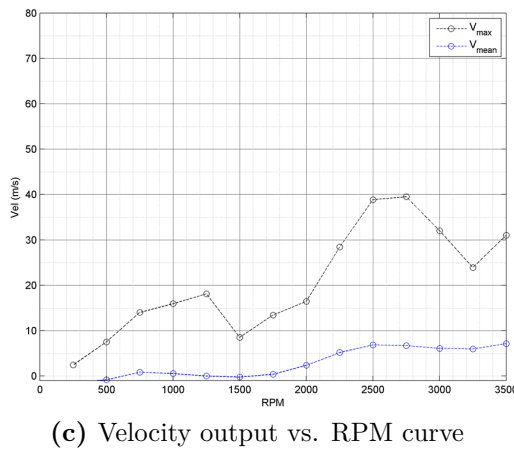
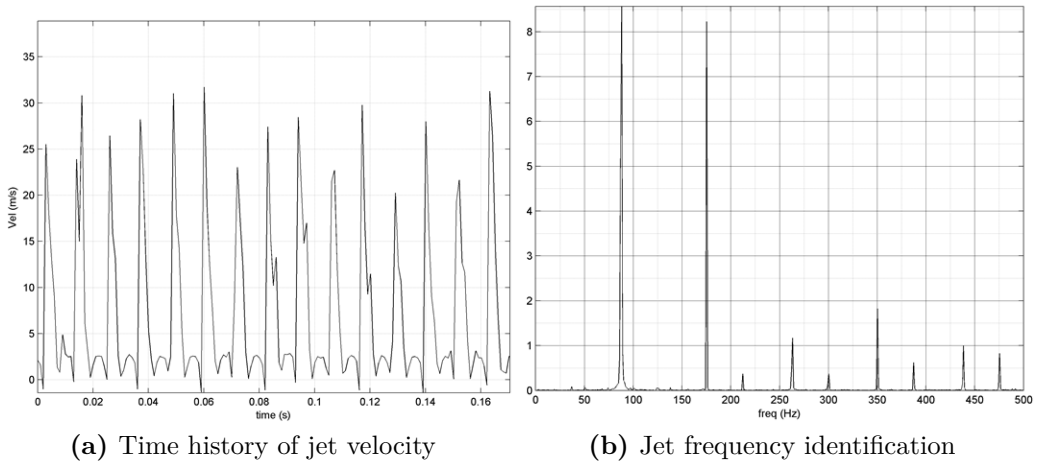


**Figure 4.22:** Hotwire measurements - SJ #4 configuration

value, which depends on the setted RPM of the mechanical SJ device; finally, it returns at the initial drag value, when the SJ is turned off. Disregarding the peaks related to jet turning on and off, the value of drag which the body experiences, when SJ is in operation, is between 15% and 30% higher than its initial value; lower drag increase happens always at 2500 RPM, that is the SJ resonant point (namely  $f = 88$  Hz,  $V_{jet_{max}} = 38.87$  m/s and  $V_{jet_{mean}} = 6.88$  m/s). As in the case of the 25° rear end Ahmed body, it is also experienced a change of SJ effectiveness in correspondence of  $V_{inf}$  increments, due to the lowering of non-dimensional parameters ( $C_{\mu}$  and  $F^{+}$ ).

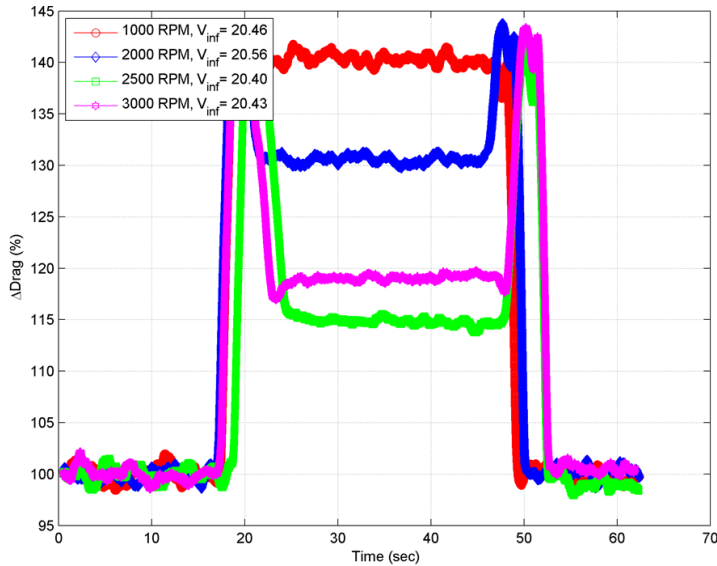


**Figure 4.23:** Load cells measurements - SJ #4 configuration

Then, tests have been done using the #5 blowing plate, without changing other components of the mechanical SJ. The #5 blowing plate has the same jet angle, referred to the horizontal plane, of the  $25^\circ$  rear end Ahmed body. Thus, the idea is to test, on the  $35^\circ$  rear end Ahmed body, if an increase of the  $\phi$  angle, from the slanted surface, could be effective in reducing body drag. Furthermore, increasing the value of the  $\phi$  angle should reduce the amount of induced drag, due to less curved apparent body determined by the jet. In fact, as for the wing, a lower body curvature determines lower lift and, in turn, lower drag due to the lift.

The Figure 4.24 resumes the tests data obtained using the #5 blowing plate at  $V_{inf} = 20$  m/s, while the Table 4.7 contains all tests in this configurations. These show that no substantial changes on load cells measurements happen substituting the #4 blowing plate with the #5 one: the drag increases at each  $V_{inf}$  value and for all RPM. ranging from 20% to 50%.

Summarizing, the  $35^\circ$  rear end Ahmed body does not experienced drag reduction as seen for the  $25^\circ$  rear end Ahmed body; but, conversely, even if active control device is capable of reducing separation over its slanted surface, the consequent induced drag increment is too high to overcome the

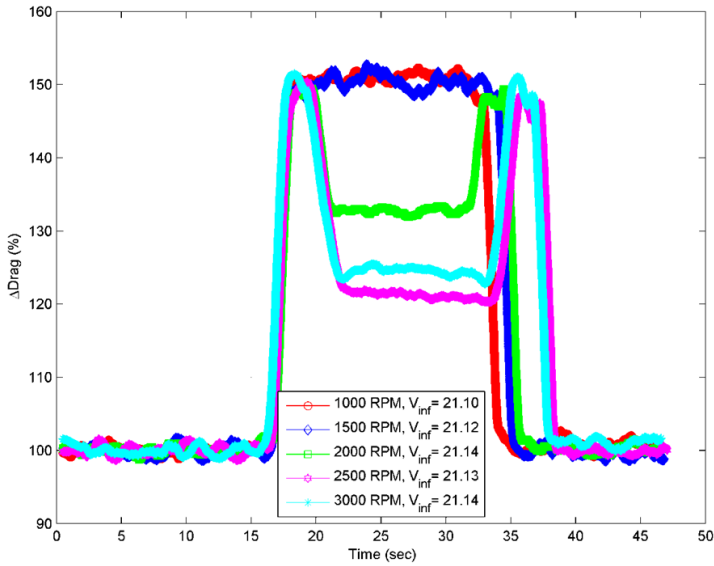


**Figure 4.24:** Load cells measurements - SJ #5 configuration

beneficial effects do to the flow reattachment. In other words, the overall drag of such body is higher with the use of an active control device than its value in clean configuration and this behaviour is mainly due to the negative effects of the induced drag.

$V_{inf}$ [m/s]	$V_{jet_{max}}$ [m/s]	$V_{jet_{mean}}$ [m/s]	RPM	f [Hz]	$\Delta Drag$
15	15.95	0.56	1000	36	15.52%
15	—	—	1000	—	25.42%
15	16.47	2.39	2000	71	12.87%
15	—	—	2000	—	21.18%
15	38.87	6.88	2500	88	11.97%
15	—	—	2500	—	11.63%
15	32.04	6.09	3000	103	10.30%
15	—	—	3000	—	13.45%
20	15.95	0.56	1000	36	14.01%
20	—	—	1000	—	14.08%
20	—	—	1000	—	40.26%
20	16.47	2.39	2000	71	21.32%
20	—	—	2000	—	30.93%
20	38.87	6.88	2500	88	20.42%
20	—	—	2500	—	14.89%
20	32.04	6.09	3000	103	14.10%
20	—	—	3000	—	19.05%
25	15.95	0.56	1000	36	9.60%
25	—	—	1000	—	9.98%
25	—	—	1000	—	46.48%
25	16.47	2.39	2000	71	28.38%
25	—	—	2000	—	33.24%
25	38.87	6.88	2500	88	25.51%
25	—	—	2500	—	16.60%
25	32.04	6.09	3000	103	19.73%
25	—	—	3000	—	20.92%
30	15.95	0.56	1000	36	5.49%
30	—	—	1000	—	43.29%
30	16.47	2.39	2000	71	34.50%
30	—	—	2000	—	39.55%
30	38.87	6.88	2500	88	29.70%
30	—	—	2500	—	20.69%
30	32.04	6.09	3000	103	24.66%
30	—	—	3000	—	22.52%

**Table 4.6:** Load cells measurements - SJ #4 configuration

$V_{\text{inf}}$ [m/s]	$V_{\text{jetmax}}$ [m/s]	$V_{\text{jetmean}}$ [m/s]	RPM	f [Hz]	$\Delta\text{Drag}$
15	—	—	1000	—	43.70%
15	—	—	1500	—	41.04%
15	—	—	2000	—	25.36%
15	—	—	2500	—	20.20%
15	—	—	3000	—	21.63%
20	—	—	1000	—	51.00%
20	—	—	1500	—	50.40%
20	—	—	2000	—	32.73%
20	—	—	2500	—	21.10%
20	—	—	3000	—	24.47%
25	—	—	1000	—	22.41%
25	—	—	1500	—	19.03%
25	—	—	2000	—	38.00%
25	—	—	2500	—	23.89%
25	—	—	3000	—	26.75%
30	—	—	1000	—	19.11%
30	—	—	1500	—	18.40%
30	—	—	2000	—	42.11%
30	—	—	2500	—	28.94%
30	—	—	3000	—	31.38%

**Table 4.7:** Load cells measurements - SJ #5 configuration

## 4.4 Experimental tests on FIAT Punto Classic

Lastly, several tests have been performed on a simplified car, the FIAT Punto Classic. Its external shape, as shown in Figure 2.8, was simplified conveniently for test purposes: so, rolling tyres, mirrors, windscreen wipers, door handles and other small parts, have been eliminated and neglected. Also, to fuse completely the blowing plate and chamber into the FIAT Punto shape, an approach similar to that used for the Ahmed body has been followed, as seen in Figure 2.7. Differently from the Ahmed body, this model has been realized with FDM method, in order to achieve a lighter model: thus, the model was split into several parts (see Figure 4.25a) and, then, each part has been glued together to form the complete model shape. The bottom part of this model is fixed to load cells measurements, using the same two load cells configurations of the Ahmed body (see Figure 4.25b).

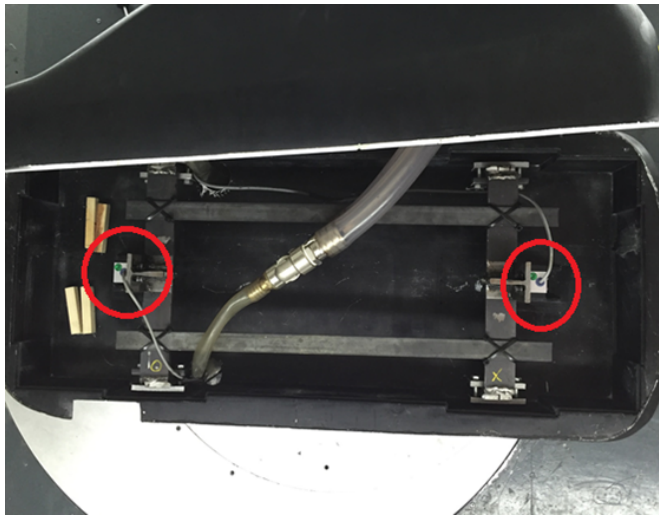
The rear end of the FIAT Punto Classic is almost truncated; thus, the expected behaviour could be more likely the  $35^\circ$  rear end Ahmed body. In the light of this, the FIAT Punto model has been tested only using the SJ active control device. The configuration tested is made by the same mechanical SJ device as previously described and by an indivisible terminal part, composed by the blowing chamber and the blowing plate. Blowing chamber has only one separation wall in the symmetry plane and its shape is elliptical, for being simply installed into the available space inside the model. Its overall volume of  $0.000\ 190\ \text{m}^3$  is slightly larger than those of the Ahmed body. The blowing plate has been designed to have  $\phi$  angle of  $20^\circ$ , referred to the rear end surface.

### Tests with synthetic jet device

First investigations on the FIAT Punto model have been performed to verify if any analogy exists between flow phenomena over such model and those observed over the  $35^\circ$  rear end Ahmed body. Thus, some wool tufts have been disposed on the surface, mainly on the rear end surface: by means



(a) Some model parts

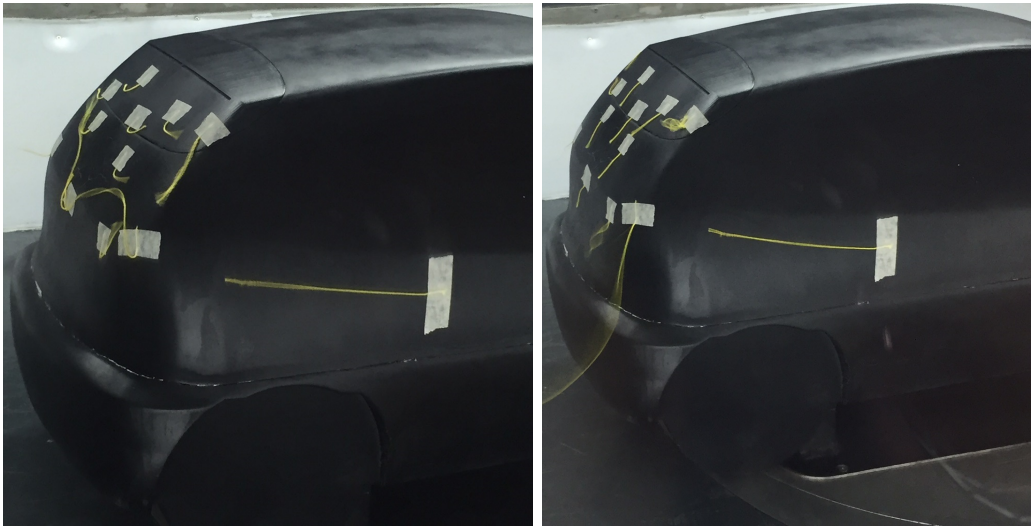


(b) Load cells configuration

**Figure 4.25:** FIAT Punto model overview

of these, the idea is to confirm visually that separation occurs in clean configuration and, then, it disappears when the SJ active control device is in operation. The comparison between such two situations is presented in Figure 4.26: in Figure 4.26a, it can be seen how tufts are reversed on the rear end surface, signifying the occurrence of large separation over the model rear end; conversely, from Figure 4.26b it can be observed the reattachment of the flow on the rear end surface and, thus, the extinction of separation. Moreover, using a rake of total pressure probes, located in the same position used for analyses behind the Ahmed body, the fields of  $u$  velocity has been acquired, in both situations. The  $u$  velocity maps are shown in Figure 4.27,





(a) Tufts w/o SJ control jet

(b) Tufts w/ SJ control jet

**Figure 4.26:** Tufts images for the FIAT Punto Classic

for the case w/o and w/ SJ: the Figure 4.27a shows the large extent of separation behind the FIAT Punto model, very similar to that seen behind the  $35^\circ$  rear end Ahmed body; using the SJ device, the  $u$  field changes and, as seen for the  $35^\circ$  rear end Ahmed body, tip vortices appear. Even if the measured area was not large enough to capture all the field behind the body, it is sufficient to observe such phenomena which confirm analogies between the FIAT Punto model and the  $35^\circ$  rear end Ahmed body.

Before load cells measurements, due to the different blowing chamber and plate, it was necessary to make hotwire measurement to characterize such SJ configuration. Hotwire probe has been disposed similarly to previous acquisitions made on the Ahmed body (Figure 4.28c). Time histories at different values of RPM of the mechanical SJ have been post-processed using the FFT method, in order to relate RPM to jet frequency. The curve in Figure 4.28d displays the relationship between RPM and jet velocity: as previously observed, the main resonance occurs nearly at 2500 RPM, but a first resonance is also present, at 750 RPM, even if it causes smaller velocity values. The reasons of the presence of two resonant point could be the slightly larger volume of the blowing chamber, as compared to those of the

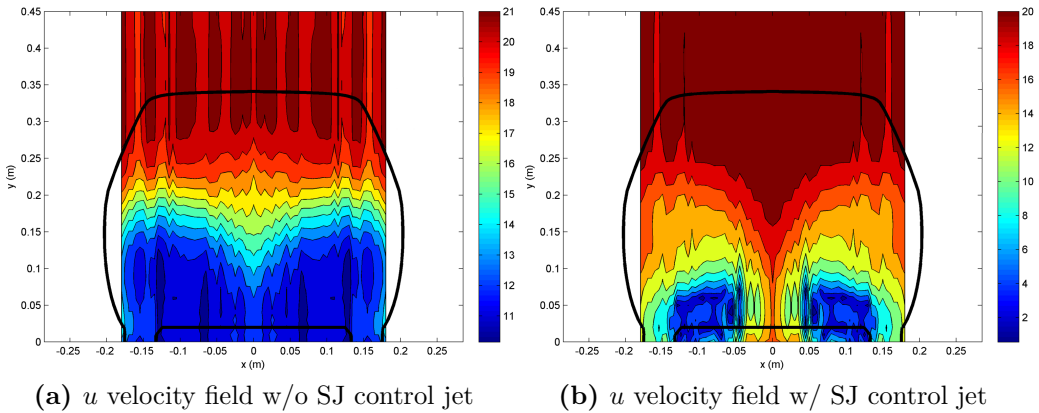


**Figure 4.27:**  $u$  velocity fields for the FIAT Punto Classic model

Ahmed body.

Recognizing the analogies between the behaviour of the FIAT Punto model and the  $35^\circ$  rear end Ahmed body, the expected results of load cells measurements is the proof of ineffectiveness of such active control devices in reducing drag of bluff bodies like these. The data measured with load cells are summarized in Table 4.8, for different values of both  $V_{\text{inf}}$  velocities and RPMs of the mechanical SJ device. In Figure 4.29 is shown the case at  $V_{\text{inf}} = 20 \text{ m/s}$ : this picture underlines that using the SJ on the FIAT Punto model results always in a drag increase of about 20%, independently from the RPM value of the mechanical SJ. The Table 4.8 highlights also that this situation is not isolated, but it happens almost at all the tested  $V_{\text{inf}}$  velocities.

$V_{inf}$ [m/s]	$V_{jetmax}$ [m/s]	$V_{jetmean}$ [m/s]	RPM	f [Hz]	$\Delta$ Drag
15	36.97	18.68	750	27	19.79%
15	23.53	11.1	1000	36	19.67%
15	—	—	1000	—	19.12%
15	28.63	16.33	2000	71	16.29%
15	—	—	2000	—	17.78%
15	61.27	29.51	2500	88	17.96%
15	—	—	2500	—	22.97%
15	64.52	27.31	2750	95	14.93%
15	52.91	23.63	3000	103	18.60%
15	—	—	3000	—	21.10%
20	36.97	18.68	750	27	20.65%
20	23.53	11.1	1000	36	20.02%
20	—	—	1000	—	19.41%
20	28.63	16.33	2000	71	18.97%
20	—	—	2000	—	18.62%
20	61.27	29.51	2500	88	17.97%
20	—	—	2500	—	20.37%
20	64.52	27.31	2750	95	18.21%
20	52.91	23.63	3000	103	19.34%
20	—	—	3000	—	19.02%
25	36.97	18.68	750	27	18.39%
25	23.53	11.1	1000	36	19.38%
25	—	—	1000	—	18.26%
25	28.63	16.33	2000	71	19.95%
25	—	—	2000	—	19.17%
25	61.27	29.51	2500	88	18.40%
25	—	—	2500	—	19.10%
25	64.52	27.31	2750	95	17.92%
25	52.91	23.63	3000	103	18.52%
25	—	—	3000	—	18.94%
30	36.97	18.68	750	27	17.40%
30	23.53	11.1	1000	36	43.29%
30	—	—	1000	—	17.71%
30	28.63	16.33	2000	71	39.55%
30	—	—	2000	—	20.22%
30	61.27	29.51	2500	88	20.69%
30	—	—	2500	—	18.96%
30	64.52	27.31	2750	95	18.69%
30	52.91	23.63	3000	103	22.52%
30	—	—	3000	—	19.23%

Table 4.8: Load cells measurements - FIAT Punto model w/ SJ

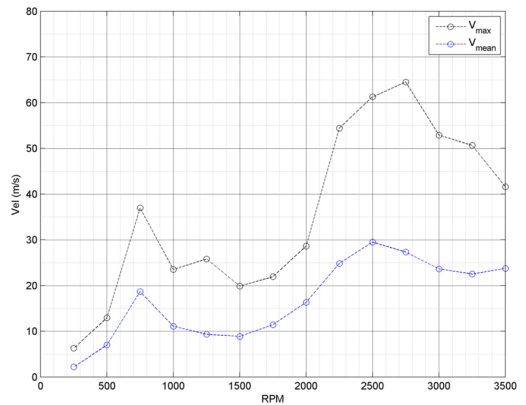
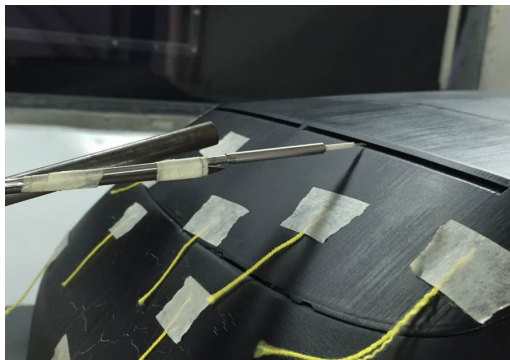
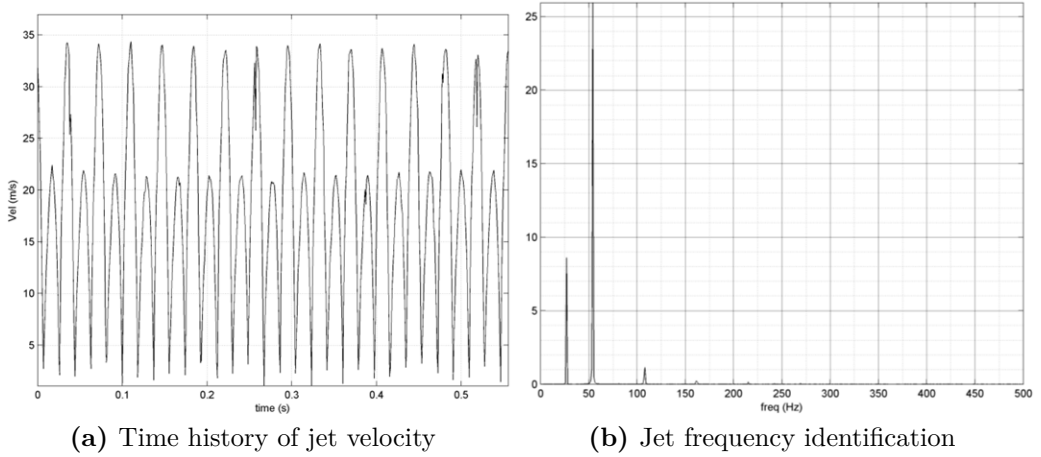


Figure 4.28: Hotwire measurements - FIAT Punto model w/ SJ

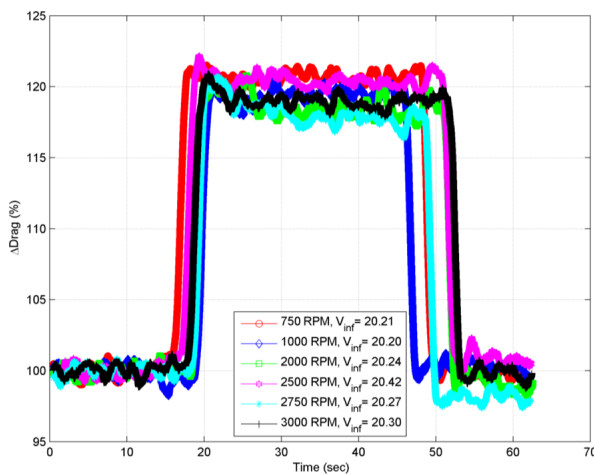


Figure 4.29: Load cells measurements - FIAT Punto model w/ SJ



## A simplified model for designing unsteady control devices using the electroacoustic analogy

---

After experimental tests, it has been noticed that, using an unsteady active control device on the  $25^\circ$  rear end Ahmed body, it's possible to reduce drag of about 10% from its the initial value. In order to accomplish this target, the SJ device must work at 88 Hz, producing at least 63.01 m/s of maximum outlet velocity. To produce such jet using the mechanical SJ device, the power needed to obtain the 10% drag reduction of the Ahmed body is surely higher than the related power drop due to lower drag. Also, considering that the SJ device principle, like other unsteady blowing device, is to work in resonance with cavity, a way to decrease the device needs of power is to design it in order to have resonant conditions at the desired jet frequency.

Hence, this chapter describes the development of a quite simplified model, based on the electroacoustic analogy, to determine the configuration of the mechanical SJ device, used during the tests, which allows it to work in resonant condition at  $f = 88$  Hz. The new features of such model, as compared with the existing ones, are that it can be modified to be compliant with both active devices used, as the UB and the SJ systems, and, moreover, that it takes into account all the phisical elements of the active control

device, from the generation system to the blowing chamber, whatever it is.

## 5.1 The idea and foundation elements

The fundamentals of the electroacoustic analogy are the similitude of the velocity and pressure equations, for flow into tubes, with the same of current and voltage, of an electrical circuit. In other words, the equations of an acoustics system, in which air flows with a certain velocity and pressure, are similar to those of an electrical circuit, in which voltage and currents pass. The theory behind this analogy is well described in several books, such as [36], [37], [38]: the authors underline the analogies between mechanical, electrical and acoustics elements, demonstrating how the analogies could be inferred from the equations describing such different systems. The main result of this analogy is that (acoustic) pressure and electrical voltage have the same role into the differential equations describing the related phenomena as well as (acoustic) mass flow rate and electrical current. Thus, it is possible to replicate an acoustical system by means of electrical circuit in order to determine its flow parameters and vice versa. In the light of this, it is possible to replicate the overall mechanical SJ device using an electrical circuit and, so, find out lengths, diameters and chamber volumes, which allow it to resonate at the wanted frequency.

To accomplish this task, it is necessary to use other results of such analogy. The analogy allows to relate coefficients of electrical differential equations with acoustic and mechanical ones; and, also, to compute their values starting from physical dimensions. As an example, in Figure 5.1 it is presented a picture which summarizes this relationship. The picture show an electrical circuit which corresponds to a physical acoustic one: the voltage generator in Figure 5.1 is the corresponding circuitual elements of a pressure supply, such as a compressor or the rotating valve (it changes the steady pressure supply to unsteady one); the first group of inductance and resistance takes into account the connection tube between the pressure supply and the blowing terminal; the orange circled part describes what happens inside the blowing chamber and through the blowing plate, by

means of resistance, inductance and capacitance.

More deeply, the behaviour of the blowing terminal can be described by the so-called Lumped Element Model (LEM), while that of connection lines must be described with the so-called Distributed Model. The difference among the two model is that behaviour of connection tubes depends on the frequency at which pressure supply oscillates, while that of the chamber is almost unaffected. Regarding the LEM model, from [36], circuital elements can be evaluated by means of (5.1): the expression in (5.1) are universal and, depending on the shape of the blowing plate (circular/slot), must be modified. Mainly affected by the shape of the blowing plate are  $R_{act}$  and  $L_{act}$ , while  $C_{act}$  depends only by the chamber volume  $V_0$ . In (5.1),  $\rho$  is the flow density,  $c$  is the sound velocity,  $P_{abs}$  is the absolute pressure,  $A_s$  is the blowing plate exit area,  $l$  is the blowing plate thickness,  $\Delta P$  is the pressure difference inside the blowing chamber and  $Q = \frac{V_{out}}{A_s}$  is the mass flow rate from the blowing plate. Considering that the blowing plate used during the tests has a rectangular exit, the expressions to calculate  $R_{act}$  and  $L_{act}$  are reported in [36] and here in (5.2), where  $Z_{act}$  is the blowing plate impedance,  $w$  is the blowing plate thickness,  $l$  is the slot exit length and  $d$  is the slot exit width.

$$\begin{aligned} R_{act} &= \frac{\Delta P}{Q} \\ L_{act} &= \frac{\rho l}{A_s} \\ C_{act} &= \frac{V_0}{\gamma P_{abs}} = \frac{V_0}{\rho c^2} \end{aligned} \quad (5.1)$$

$$Z_{act} = R_{act} + j \omega L_{act}, \quad R_{act} = \frac{12 \mu w}{d^3 l}, \quad L_{act} = \frac{6 \rho w}{5 l d} \quad (5.2)$$

$$\omega_v = \frac{R_t}{L_t} = \frac{8 \pi \nu}{A} \quad (5.3)$$

The works [39] and [40] give an useful understanding of the behaviour



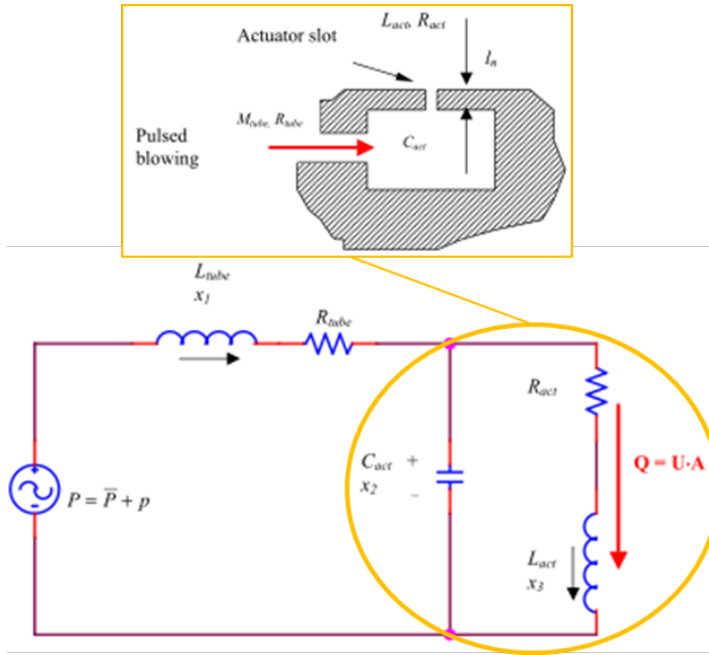


**Figure 5.1:** Lumped Element model for blowing chamber and plate

and modelling of distributed lines. Summarizing, connection tubes can be modelled with the distributed lines in Figure 5.2; the equation of pressure and mass flow rate (see (5.4)), having the same form of that of voltage and current, can be written substituting physical components to electrical ones, such as  $R_t$ ,  $L_t$ ,  $G_t$ ,  $C_t$ . In this way, physical system dimensions are considered during the evaluation of  $R_t$ ,  $L_t$ ,  $G_t$ ,  $C_t$ , by means of expressions in (5.5). These expressions are function of oscillation frequency  $\omega$  and characteristic frequency  $\omega_v$ , air parameters ( $\mu$ ,  $\gamma$ ,  $\sigma$ ,  $\rho$ ,  $P_{abs}$ ) and section tube  $A$ . In the case of distributed lines the circuitual elements  $R_t$ ,  $L_t$ ,  $G_t$ ,  $C_t$ , are per unit of length and, thus, they have to be integrated over the tubing length.

$$\begin{aligned} \frac{dp}{dx} &= Z_t q = (R_t + i \omega L_t) q \\ \frac{dq}{dx} &= Y_t p = (G_t + i \omega C_t) p \end{aligned} \tag{5.4}$$

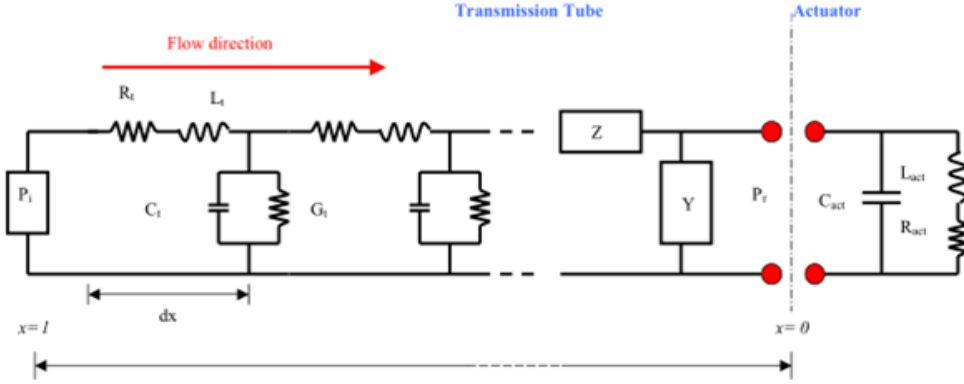


Figure 5.2: Distributed model for connection tubes

$$\begin{aligned}
 R_t &= \frac{1}{2} L \sqrt{\omega \omega_v} + \frac{8 \pi \mu}{A^2} \\
 L_t &= \frac{\rho}{A} \\
 C_t &= \frac{A}{\gamma P_{abs}} \\
 G_t &= \frac{(\gamma - 1)}{2 \sigma} C \sqrt{\omega \omega_v}
 \end{aligned} \tag{5.5}$$

## 5.2 Electrical circuit for device optimization

The SJ device used for tests is more complex than a simple connection tube with a blowing terminal; hence, the evaluation of corresponding electrical circuit is hard to perform by hand. So, it is necessary to use a software tool to resolve the related circuit. Implementing these equations into a MATLAB script and using the SimRF Simulink toolbox, it is possible to design a whatever complex electrical circuit, made up of resistors, inductors and capacitors. Also, the SimRF Simulink toolbox includes a block (Figure 5.3) which allows to simulate distributed line, using the same parameters in (5.5).

The Figure 5.5 presents the electrical circuit created into the Simulink environment, which replicates the real active control device. As listed

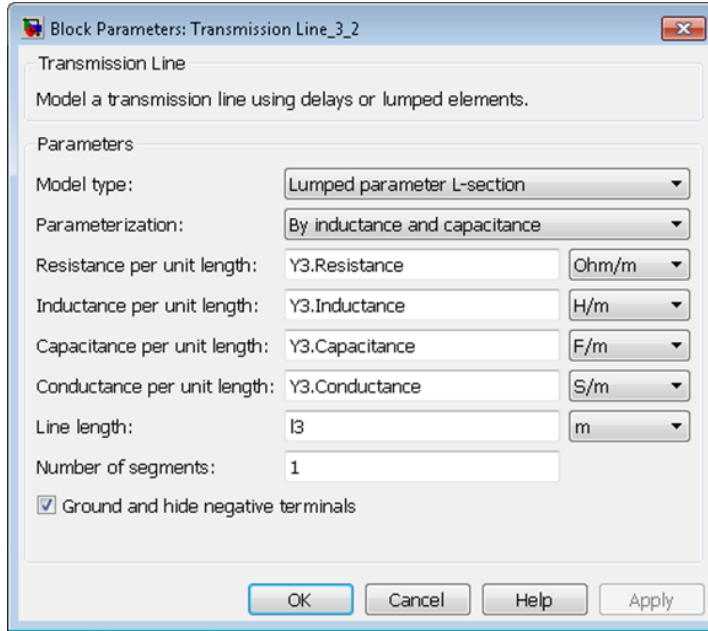


**Figure 5.3:** Overview of the distributed line block of SimRF Simulink toolbox

in Table 2.2 and in Table 2.3, the arrangement of the both active control devices is quite similar: both devices have three distribution lines and slightly different blowing terminal. So, the overall arrangement of the circuit is the same.

Considering that the blowing terminal cannot be changed without creating a new one, it has been considered fixed; so, to determine the resonant condition of such active devices, the investigation has been more focused on determine which lengths and diameters of connection tubes cause higher output from the blowing terminal. Lengths  $L_1$ ,  $L_2$  and  $L_3$  as well as diameters  $d_1$ ,  $d_2$  and  $d_3$ , can assume values within a prescribed range, while the frequency  $\omega$  has been fixed at the corresponding value of frequency  $f = 88$  Hz.

The schematic view of the optimization cycle is in Figure 5.4. Optimization starts from an initial set of values for lengths and diameters, which are those in Table 2.3, with which circuitual elements are evaluated, using the equations in (5.5) and in (5.2); then, with these circuitual elements, circuit response in the time domain has been estimated, measuring electrical current

(that is the mass flow rate  $Q$ ) and, hence,  $V_{out}$  from the slot. To estimate time response, a white noise input has been used, in order to be independent of the voltage generator, that could be the pressure supply or the mechanical device. Knowing time response of the circuit, it is possible to determine at which frequency  $f$  resonance occurs, calculating the system transfer function: the transfer function is the ratio between the system response and the input forcing, in the frequency domain. Hence, it is necessary to transform, using the FFT algorithm, both the input forcing and system response into the frequency domain, so as transfer function  $F(s)$  can be evaluated. This cycle continues until the termination criteria is satisfied: the optimization cycle ends when the function  $\frac{1}{F(s)}$  reaches the minimum. In fact, when the the function  $\frac{1}{F(s)}$  has its minimum value, the transfer function  $F(s)$  has its maximum value and, so, the current and velocity  $V_{out}$  from the slot: in this condition, the set of lengths and the diameters makes the system to work in resonant condition.

The optimization has been carried out to identify the lengths and diameters for active control device resonance and results are graphically summarized in Figure 5.6. In Table 5.1, there are lengths and diameters at which resonance occurs. The Figure 5.6a shows that after about 220 iterations, the maximum of  $F(s)$  is reached; in these condition, pressure into the chamber and outlet velocity from the slot diverge over the time, as shown in Figure 5.6c and in Figure 5.6d. The resonance is evident in Figure 5.6b, where the ratio between the velocity output fluctuation  $|u_e'|$  and the fluctuations of input pressure  $|p_i'|$ , over the frequency  $f$ , is displayed: it shows that the main resonant peak occur at 88 Hz, as expected, with  $\frac{|u_e'|}{|p_i'|} = 0.058$ . The set of lengths and diameters that allows the active control device to work in resonant condition is listed in Table 5.1: these have to be validated by means of experimental tests, that have not yet performed.

Even if the results have not validated, the method exposed provides an investigation technique for finding resonance conditions of complex blowing system, searching the best set of connection tubes dimensions.

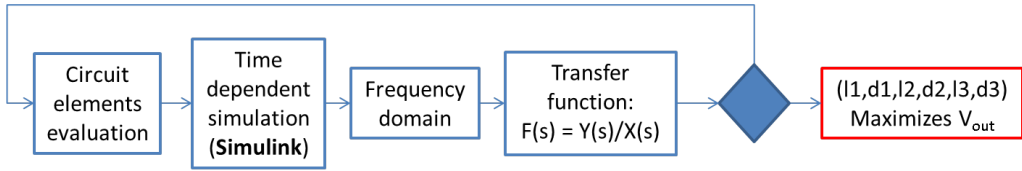


Figure 5.4: Schematic view of the optimization cycle

Optimization starting point					
$L_1$	$d_1$	$L_2$	$d_2$	$L_3$	$d_3$
0.70 m	0.031 75 m	1.8 m	0.0254 m	0.50 m	0.0254 m
The optimization cycle stops when $1/F(s)$ reaches a minimum when $F(s)$ is maximum					
$L_1$	$d_1$	$L_2$	$d_2$	$L_3$	$d_3$
0.56 m	0.0254 m	3.16 m	0.0254 m	0.23 m	0.0254 m

Table 5.1: Optimization cycle results - System geometry

### 5.3 Ideal power consumption and power saving estimation

As seen before and in [41] and in [42], electroacoustic analogy is mainly used as preliminary design tool for SJ actuators. In this section, another use of such electroacoustic analogy is proposed.

The purpose of this final section is to use this approach to estimate the ideal power consumption of an active control device, of synthetic jet type, capable to reduce drag of bluff bodies, as the 25° rear end Ahmed body. In fact, among the different configurations of bluff body tested, only for this one resulted beneficial to use active control device for reducing drag, with an average gross drag reduction of about 10%.

To do this estimation, power consumption has been evaluated calculating the active power of the electrical circuit equivalent to the real active device. In fact, remembering the definition of reactive and active powers for unsteady-state electrical circuits, the active power is the only amount of power which can be lost due to Joule effect and, so, it can be assumed as the power

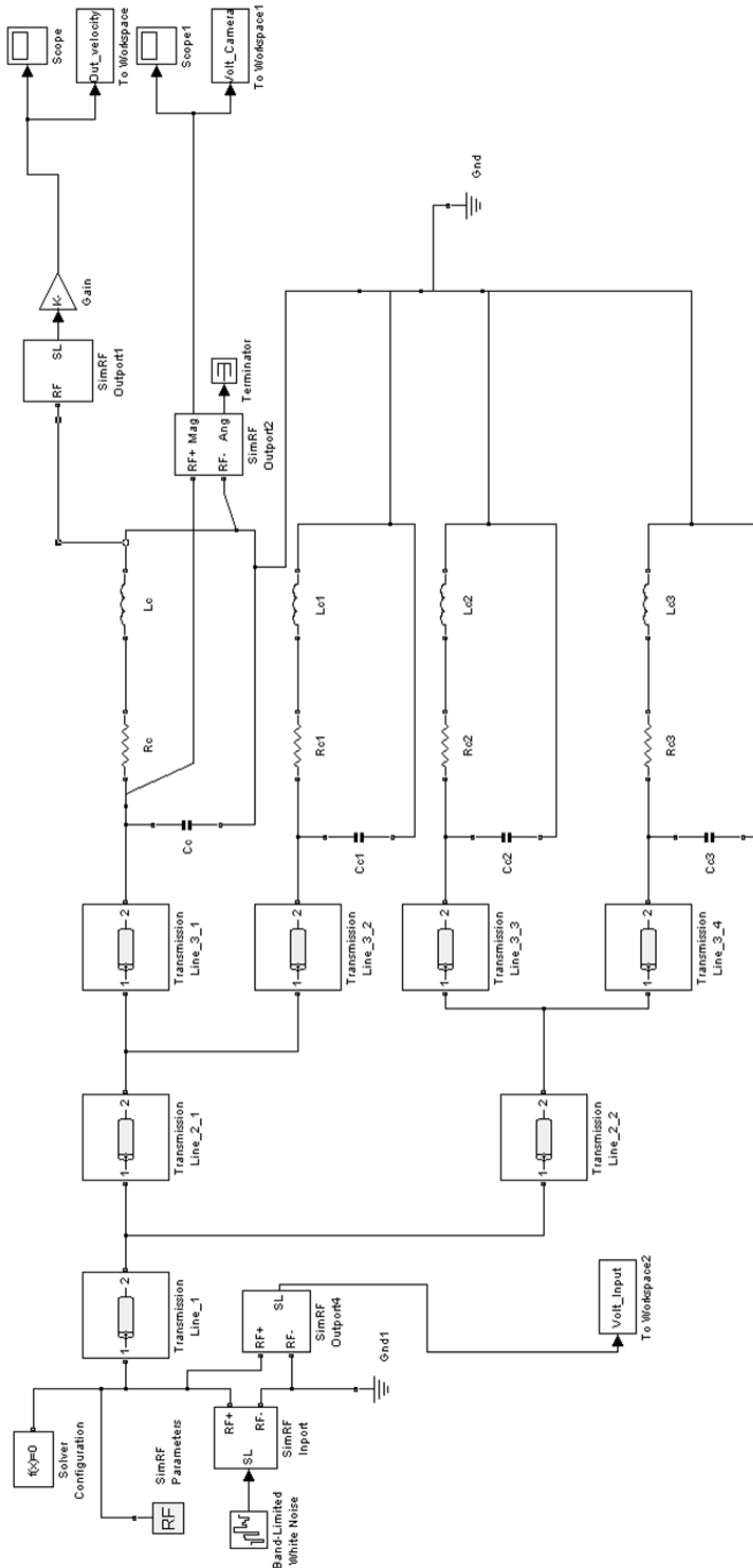
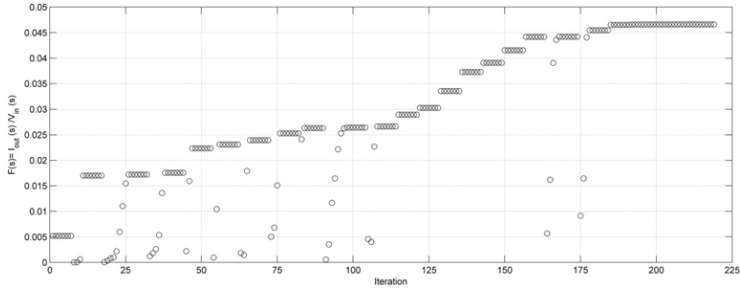
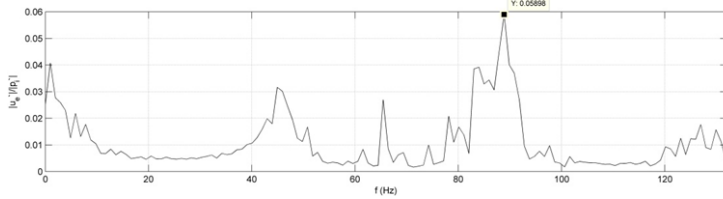
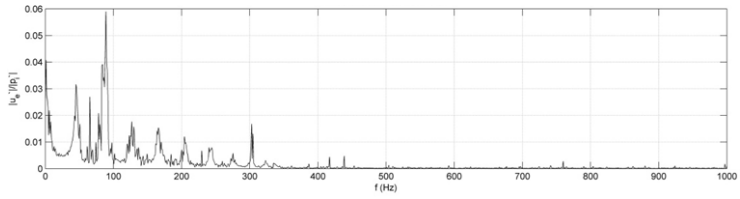


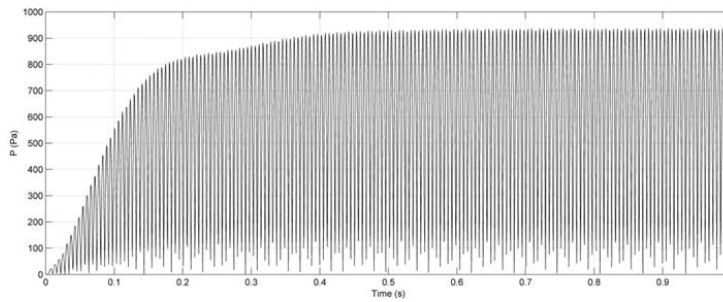
Figure 5.5: Simulink toolbox - Equivalent circuit of the tested SJ device



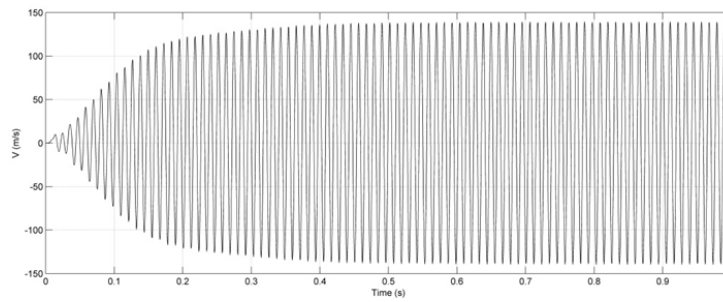
(a) Iteration



(b) Transfer function  $F(s)$



(c) Pressure vs. Time



(d) Velocity vs. Time

Figure 5.6: Optimization cycle results

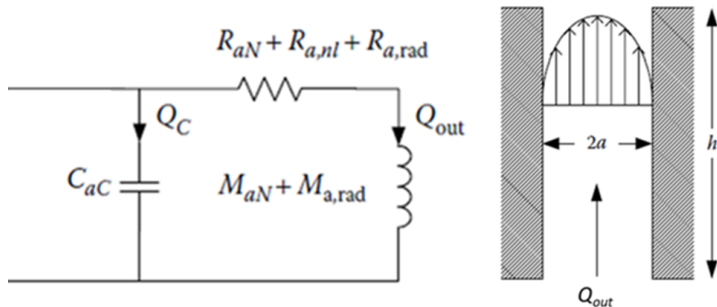


**Figure 5.7:** Circuit used for power consumption estimation

needed to drive the active control device; conversely, the reactive power may be assumed to be related to the amount of power that remains stored inside the circuit, due to the presence of capacitance and inductance. To estimate such active power, only the blowing terminal has been considered and a slightly modified LEM model has been used.

From [38], a schematic representation on the analogy is presented in Figure 5.7. Differently from the previous, the electrical resistance is made up of different contributions,  $R_{aN}$ ,  $R_{a,nl}$  and  $R_{a,rad}$ , which take into account secondary non-linear effects ( $R_{a,nl}$ ) and radiation effects ( $R_{a,rad}$ ), while the  $R_{aN}$  is analogous to  $R_{act}$  in (5.2), for a  $2D$  rectangular slot.

The equations of such resistance components are in (5.6). Into these equations,  $h$  is the blowing plate thickness,  $a$  is the half of the slot exit width,  $w$  is the slot length,  $S_n$  is the slot cross-sectional area ( $S_n = 2aw$ ),  $\rho$  is the air density,  $\mu$  is the air dynamic viscosity,  $c$  is the isentropic speed of sound,  $Q_{out}$  is the volume flow rate from the slot and  $K_d$  is a dimensional dump loss coefficient, which takes into account the velocity profile through the blowing plate thickness. The value of  $K_d$  has been selected as that of a  $2D$  slot ( $K_d = 2/5$ ).

Calculating these resistance components and adding together, the ideal power consumption of such active control device can be evaluated by means of equation (5.7), substituting  $I_{rms}$  with  $Q_{out}$ . In Table 5.2 is reported the estimation of power consumption for both data available from tests and numerics (CFD). In fact, this comparison is intended to underline that, during the tests, the characteristics of the control jet have been different to



those wanted from CFD calculations, resulting in much higher ideal power consumption. In other words, if during the tests it would have been possible to generate the jet used for CFD simulations and it would have resulted to be effective, the ideal power saving obtained with such device should be much higher. From the Table 5.2, it results that, ideally, the needs of power to produce a jet with the effective frequency  $f$  and  $V_{out}$  is about 5 W, while the tested jet needs about 18 W.

$$\begin{aligned}
 R_{aN} &= \frac{3 \mu h}{2 w a^3} \\
 R_{a,nl} &= \frac{0.5 \rho K_d |Q_{out}|}{S_n^2} \\
 R_{a,rad} &= \frac{\rho \omega^2}{2 \pi c} \left( 1 - \frac{\omega^2 w^2}{36 c^2} \right)
 \end{aligned} \tag{5.6}$$

$$\begin{aligned}
 \Pi_{sj} &= R_{tot} I_{rms}^2 \\
 &= (R_{aN} + R_{a,nl} + R_{a,rad}) \frac{Q_{out}^2}{2}
 \end{aligned} \tag{5.7}$$

Using the last result and considering a drag reduction of about 10%, due to the active control device (the 25° rear end Ahmed body drag decreases from about 10.9 N, measured in clean configuration, to about 9.81 N, using the active control device) the power saving resulting from drag reduction, at  $V_{inf} = 20$  m/s, is about 22 W (see (5.8)). In the light of this, the overall ideal power saving, obtained with an active control device operating at design conditions, can be evaluated using the formula (5.9): substituting the calculated drag power saving and power needed by the active control

	$f$ [Hz]	$V_{out}$ [m/s]	$R_{aN}$	$R_{a,nl}$	$R_{a,rad}$	$R_{tot}$	$Q$ [m <sup>3</sup> /s]	$\Pi_{sj}$ [W]
Tests	88	63.5	1757.96	32256.84	4.53	34019.33	0.0321	17.53
CFD	100	40	1757.96	20319.27	5.85	22083.09	0.0202	4.51

**Table 5.2:** Ideal power consumption

device, it results that the overall ideal power saving is about 20%. It has to be noticed that this estimation does not take into account any device efficiency loss, which depends highly on the way of generation of controlling jet; hence, in this sense, the power saving calculated is ideal.

$$\begin{aligned}\Pi_{drag} &= D V_{inf} \Rightarrow \\ \Delta\Pi_{drag} &= \Delta D V_{inf} = (10.9 \text{ N} - 9.81 \text{ N}) 20 \text{ m/s} \approx 22 \text{ W}\end{aligned}\tag{5.8}$$

$$\begin{aligned}\Delta\Pi &= \frac{\Pi_{sj} - \Delta\Pi_{drag}}{\Delta\Pi_{drag}} = \frac{17.53 - 22}{22} = -0.20 \Rightarrow \\ \Delta\Pi[\%] &= -20\%\end{aligned}\tag{5.9}$$



---

## Conclusions and future works

---

The work presented in these pages is a summary of numerical and experimental activities on bluff bodies drag reduction using active control devices. Mainly, the work focused on car shaped bluff bodies, as the well-known Ahmed body and a simplified FIAT Punto Classic model. Knowing the capabilities of Ahmed body in reproducing flow field of different kinds of car, two configurations of it has been investigated, which have slant angles of  $25^\circ$  and  $35^\circ$ , respectively.

Both numerical (CFD) and experimental investigations confirmed the possibility of reducing drag of bodies whose flow field is similar to the  $25^\circ$  rear end Ahmed body; but, among the set of parameters investigated, it has not been recognized any effective condition of reducing drag of  $35^\circ$  rear end Ahmed body. Moreover, considering that this Ahmed body configuration is representative of the class of cars in which the FIAT Punto Classic can be classified, the use of active control device on such model results detrimental as well.

A possible explanation of this different effectiveness of the active control device respect to shape changing, could be found making the so-called drag breakdown: for these bodies, drag is mainly composed by the pressure drag, the lift-induced drag (or drag due to lift) and skin friction drag. With the experimental tests, it has been verified the reduction of flow separation behind the body, that causes a reduction of pressure drag. Also, a strange behaviour has been observed on the  $35^\circ$  rear end Ahmed body: when active control device is operating, tip vortices appear behind the body; these vortices signify the increment of vertical force and its related lift-induced

drag. Hence, the different effectiveness of active control device can be explained considering this: while active control device causes the flow to reattach over the slanted surface and, so, reduces the amount of pressure drag, it redistributes pressure over the body determining an increment of lift-induced drag. So, if the reduction of pressure drag is larger than the increment of lift-induced drag, as in the case of the 25° rear end Ahmed body, the use of an active control device is beneficial; otherwise, it is completely detrimental. All these thoughts are summarized in Table 6.1, along with jet parameters which are effective in reducing 25° rear end Ahmed body drag.

Model	Active control	$V_{inf}$ [m/s]	$P$ [atm]	$V_{out}$ [m/s]	$f$ [Hz]	Blowing plate	$\Delta drag$ [%]
Ahmed (25°)	Unsteady Blowing	21	0.8	–	200	–	–11.54
Ahmed (25°)	Unsteady Blowing	21	1	–	200	–	–7.78
Ahmed (25°)	Unsteady Blowing	31	1	–	140	–	–7.76
Ahmed (25°)	Synthetic Jet	21	–	63.5	88	#1	–11.35
Ahmed (25°)	Synthetic Jet	31	–	63.01	88	#2	–3.83
Ahmed (25°)	Synthetic Jet	–	–	–	–	#3	ineffective
Ahmed (35°)	UB + SJ						always ineffective
FIAT Punto	Synthetic Jet						always ineffective

**Table 6.1:** Main results summary

Once effective jet conditions have been identified, an electroacoustic model has been developed to make active control device to resonate at the wanted jet frequency. The idea is to exploit resonance to reduce device power needs and increase overall power saving. Starting from the available system arrangement, a electrical circuit has been created inside Simulink environment and an optimization study has been carried out to determine tubing lengths and diameters able to run the mechanical synthetic jet device in resonance. The optimization process has found a suitable set of lengths and diameters, but, unfortunately, they were not yet validated with tests.

Lastly, using electroacoustic analogy, an estimation of ideal power saving has been carried out. This estimation highlighted that, for the case of 25° rear end Ahmed body, it is ideally possible to save about 20% of power, considering the power saving due to drag and the power needed by the active

control device, operating with effective set of parameters.



---

# Bibliography

---

- [1] Hucho W. H., (1998), *Aerodynamics of Road Vehicles - Fourth Edition*, SAE International.
- [2] L. Dumas, (2008), *CFD-based optimization in Automotive Aerodynamics*, book chapter in *Optimization and Computational Fluid Dynamics*, Springer.
- [3] Ahmed S.R., Ramm G. and Faltin G., (1984), *Some salient features of the time-averaged ground vehicle wake*, SAE 840300.
- [4] Barnard R. H., (2001), *Road Vehicle Aerodynamic Design, An Introduction - Third Edition*, MechAero Publishing.
- [5] Katz J. and Plotkin A., (1991), *Low-Speed Aerodynamics - From Wing Theory to Panel Methods*, McGraw Hill.
- [6] Joseph P., Amandolèse X., Aider J. L., (2010), *Drag reduction on the 25° slant angle Ahmed reference body using pulsed jets*, Research Article, Springer.
- [7] Aronsson E., Blank G., Nilsson D., (2010), *Numerical simulation of the flow around simplified vehicle*, Bachelor's Thesis, Chalmers University of Göteborg.
- [8] Baxendale A. J., Graysmith J. L., Howell J., Hayness T., *Comparisons between CFD and experimental results for the Ahmed reference model*, Research Article, MIRA and Rover Group.



- [9] Franck G., Nigro N., Storti M., D'Elia J., (2008), *Numerical simulation of the flow around the Ahmed vehicle model*, Research Article, Latin American Applied Research.
- [10] Lienhart H., Stoots C., BeckerBruneau S., *Flow and turbulence structures in the wake of a simplified car model (Ahmed model)*, Research Article.
- [11] Stankiewicz W., Morzyński M., Noack B. R., Thiele F., (2005), *Stability properties of 2D flow around Ahmed body*, Conference Article.
- [12] Fourrié G., Keirsbulck L., Labraga L., Gilliéron P., (2011), *Bluff-body drag reduction using a deflector*.
- [13] Beaudoin J.F., Aider J.L., (2008), *Drag and lift reduction of 3D bluffbody using flaps*.
- [14] Aider J.L., Beaudoin J.F., Wesfreid J.E., (2009), *Drag and lift reduction of a 3D bluff-body using active vortex generators*.
- [15] Pujals G., Depardon S., Cossu C., (2010), *Drag reduction of a 3D bluffbody using coherent streamwise streaks*.
- [16] Rouméas M., Gilliéron P., Kourta A., (2008), *Drag reduction by flow control on a car after body*.
- [17] Rouméas M., (2006), *Contribution à l'analyse et au contrôle des sillages de corps épais par aspiration ou soufflage continu*, PhD's Thesis, Politecnico di Tolosa.
- [18] Leclerc C., (2008), *Reduction de la traînée d'un véhicule automobile simplifiée à l'aide du contrôle actif par jet synthétique*, PhD's Thesis, Istituto di meccanica dei fluidi di Tolosa.
- [19] Krentel D., Mumiovic R., Brunn A., Wolfgang N., King R., (2010), *Application of active flow control on generic 3D car models*, Springer.
- [20] Krajnović S., Osth J., Basara B., (2009), *LES of active flow control around an Ahmed body with active flow control*.

- [21] Lehugeur B., (2009), *Contrôle des structures tourbillonnaires longitudinales dans le sillage d'une géométrie simplifiée de véhicule automobile: approche expérimentale.*
- [22] Brunn A., Nitsche W., Henning L., King R., (2008), *Application of Slope-seeking to a Generic Car Model for Active Drag Control*, AIAA.
- [23] Beaudoin J.F., Cadot O., Wesfreid J.E., Aider J.L., (2008), *Feedback control using extremum seeking method for drag reduction of a 3D bluff body.*
- [24] Pastoor M., Henning L., Noack B.R., King R., Tadmor G., (2008), *Feedback shear layer control for bluff body drag reduction.*
- [25] Bellobuono E. F., (2006), *Aircraft endurance improvement through turbulent separation control*, PhD's Thesis, Università degli Studi di Napoli Federico II.
- [26] Seifert A. and Wygnanski I., (1996), *On delay of airfoil stall by periodic excitation*, Journal of aircraft, 33, No.4, 691.
- [27] Seifert, A., Bachar, T., Koss, D., Shepshelovich, M., and Wygnanski, I., (1993), *Oscillatory Blowing: A Tool to Delay Boundary-Layer Separation*, AIAA Journal, 31, No. 11, pp. 2052-2060.
- [28] Tinapp F., Nitsche W., (2000), *Separation control on high lift configuration by periodic excitation*, 12DGLR-Fach-Symposium der AG STAB.
- [29] Miranda S., (2000), *Active Control of Separated Flow over a Circular-Arc Airfoil*, Virginia Polytechnic Institute.
- [30] Gutmark, E., Wygnanski, I., *The planar Turbulent Jet*, Journal of Fluid mechanics, Vol. 73, pp. 465-495, 1976.
- [31] Bremhorst K., Hollis P. G., *Velocity Field of an Axisymmetric Pulsed, Subsonic Air Jet*, AIAA Journal, Vol. 28, pp 2043-2049, 1990.

- [32] Gilarranz J. L., Traub L. W., Rediniotis O. K., *A New Class of Synthetic Jet Actuators — Part I: Design, Fabrication and Bench Top Characterization*, Journal of Fluids Engineering, Vol. 127, pp 367-376, 2005.
- [33] Gilarranz J. L., Traub L. W., Rediniotis O. K., *A New Class of Synthetic Jet Actuators — Part II: Application to Flow Separation Control*, Journal of Fluids Engineering, Vol. 127, pp 377-387, 2005.
- [34] Calise G., (2012), *Tecniche avanzate per la riduzione della resistenza all'avanzamento degli autoveicoli. Design di sistemi di controllo attivo*, Master's Thesis, Università degli Studi di Napoli Federico II.
- [35] Shevell R. S., (1988), *Fundamentals of Flight*, Prentice Hall, 2nd ed., p. 187.
- [36] Olson H. F., (1957), *Acoustical Engineering - Second Edition*, D. Van Nostrand Company, Inc., pp. 71-91.
- [37] Blauert J., Xiang N., (2009), *Acoustics for Engineers - Second Edition*, Springer, pp. 27-35.
- [38] Mohseni K., Mittal R., (2015), *SYNTHETIC JETS - Fundamentals and Applications*, CRC press.
- [39] Karam J.T. Jr., (1966), *A new model for Fluidics Transmission Lines*, Control Engineering, Vol. 13, pp. 59-63.
- [40] Karam J.T. Jr., Franke M. E., (1967), *The Frequency Response of Pneumatic Lines*, Journal of Basic Engineering, pp. 371-378.
- [41] Gallas Q., Holman R., Nishida T., Carroll B., Sheplak M., Cattafesta L., (2003) *Lumped Element Modeling of Piezoelectric - Driven Synthetic Jet Actuators*, AIAA Journal, Vol. 41, pp. 240-247.
- [42] Prasad S. A. N., Gallas Q., Horowitz S., Homeijer B., Sankar B. V., Cattafesta L. N., Sheplakx M., (2006), *Analytical Electroacoustic Model*

*of a Piezoelectric Composite Circular Plate*, AIAA Journal, Vol. 44, pp. 2311-2318.